AARHUS UNIVERSITET

# Chemical Dynamics in Liquid Helium

**Alberto Viñas Muñoz**

Aarhus University
Department of Chemistry

*Doctor of Philosophy in Chemistry*

2022

# Acknowledgements

I would like to acknowledge the present and former members of the Femtolab group at Aarhus University. Thanks to Simon and Constant for their collaboration.
During these three years I have been lucky to teach the courses of "reaction dynamics" and "physical chemistry I", as well as two laboratory courses on physical chemistry. I would like to thank Thomas Breitenbach for his thorough approach to teaching lab exercises and for always being open to introducing new ideas into the course.
The complicated and often capricious laser systems in the lab would not be as tame as they are if it were not for the invaluable experience and always inspiring attitude of Jan Thøgersen. His mastery of lasers is only rivalled by his ever curious mind.
Good experimental work is best served with good theory on the side and for that reason I would like to thank prof. Manuel Barranco and prof. Martí Pi from Universitat de Barcelona for their simulations. Besides their unmatched skills in simulating helium nanodroplet dynamics, their attitude and kindness has made it a pleasure to collaborate with them. Gràcies!
Thanks to Frank Jensen for performing calculations on the pair potentials of iodine and iodine cation with helium.
I would like to thanks Constant for taking the time to read the text and provide, as usual, useful comments and corrections. I would also like to acknowledge Henrik Stapelfeldt for his supervision.

# Abstract

The experiments presented in this thesis concern the time-resolved study of chemical dynamics in liquid helium. Besides the conclusions drawn from each of the experiments, the results obtained here build towards the long-term goal of performing low-temperature bimolecular reactions in liquid helium with femtosecond and single-particle resolution.

In the first series of experiments, the interaction of rotationally excited dopants (OCS, $I_2$, $CS_2$) with helium has been studied by means of rotational coherence spectroscopy. The observations made in these experiments reveal that dopants preserve gas-phase-like rotation if their excitation is well below the lowest energy excitation of the fluid, but an increasingly larger coupling is observed as higher rotational states are populated. Modelling the data also reveals that the rotational energy structure of molecules embedded in liquid helium can be effectively described by the transfer of angular momentum from the molecule to the droplet. In addition to investigating the rotational dynamics of linear molecules in liquid helium by means of rotational coherence spectroscopy, laser-induced alignment has been applied to a large organic molecule (subphthalocyanine) and has been used as a means of gathering structural information about the dipole moment for the $S_2 \longleftarrow S_0$ transition.
The second set of experiments concerns the photodissociation dynamics of iodobenzene doped in helium nanodroplets. Photodissociation of iodobenzene at 266 nm has revealed dynamics at longer timescales than expected for a simple direct photodissociation mechanism, and suggest that the droplet can trap some of the escaping fragments and induce a reformation of the parent (iodobenzene) molecule in a vibrationally hot state. Furthermore, the results presented here indicate that different vibrational levels of the hot iodobenzene molecule can be accessed by tuning the wavelength of the probe pulse, opening possibilities in terms of studying vibrational relaxation in liquid helium in a time-resolved manner.
In the last set of experiments, results concerning the solvation dynamics of alkali metal cations ($Na^+$, $Li^+$) in liquid helium are presented. The solvation of the cation has been followed at the single-particle level and with time resolution by means of Coulomb explosion imaging induced by ionizing a "spectator" dopant located in the center of the droplet. The dynamics measured show that, for the first solvation layer of the cation, it takes around 700 fs for each helium atom to bind to the alkali metal ion. This results are, to our knowledge, the first experiments that address solvation dynamics in the natural timescale of the process, at a single-particle level and without the need of theoretical models that aid the interpretation of the results.

# Resumé

Eksperimenterne præsenteret i denne afhandling omhandler det tidsopløste studie af kemisk dynamik i flydende helium. Udover konklusionerne fra hvert af eksperimenterne, bygger de opnåede resultater her mod det langsigtede mål om at udføre lavtemperatur bimolekylære reaktioner i flydende helium med femtosekund og enkelt-partikel opløsning.

I den første række af eksperimenter er interaktionen mellem rotationelt exciterede dopanter (OCS, $I_2$, $CS_2$) med helium blevet undersøgt ved hjælp af rotationskohærent spektroskopi. Observationerne i disse eksperimenter afslører, at dopingstoffer bevarer gasfase-lignende rotation, hvis deres excitation er et godt stykke under den laveste energiexcitation af væsken, men en stadig større kobling observeres, efterhånden som højere rotationstilstande er befolket. Modellering af dataene afslører også, at rotationsenergistrukturen af molekyler indlejret i flydende helium effektivt kan beskrives ved overførsel af vinkelmomentum fra molekylet til dråben. Ud over at undersøge rotationsdynamikken af lineære molekyler i flydende helium ved hjælp af rotationskohærent spektroskopi, er laserinduceret justering blevet anvendt på et stort organisk molekyle (subphthalocyanin) og er blevet brugt som et middel til at måle orienteringen af dipolmomentet for $S_2 \longleftarrow S_0$ overgangen.
Det andet sæt eksperimenter vedrører fotodissociationsdynamikken af iodbenzen dopet i helium nanodråber. Fotodissociation af iodbenzen ved 266 nm har afsløret dynamik på længere tidsskalaer end forventet for en simpel direkte fotodissociationsmekanisme og antyder, at dråben kan fange nogle af de undslippende fragmenter og inducere en reformation af modermolekylet (iodbenzen) i en vibrationelt varm tilstand. Desuden indikerer de her præsenterede resultater, at forskellige vibrationsniveauer af det varme iodbenzenmolekyle kan tilgås ved at indstille bølgelængden af sondepulsen, hvilket åbner muligheder i forhold til at studere vibrationsrelaksation i flydende helium på en tidsopløst måde.
I det sidste sæt af eksperimenter præsenteres resultater vedrørende solvatiseringsdynamikken af alkalimetalkationer ($Na^+$, $Li^+$) i flydende helium. Opløsningen af kationen er blevet fulgt på enkeltpartikelniveau og med tidsopløsning ved hjælp af Coulomb-eksplosionsbilleddannelse induceret ved ionisering af et "tilskuer"-dopingmiddel placeret i midten af dråben. Den målte dynamik viser, at det for det første solvatiseringslag af kationen tager omkring 700 fs for hvert heliumatom at binde til alkalimetalionen. Disse resultater er, så vidt vi ved, de første eksperimenter, der adresserer solvatiseringsdynamikker i processens naturlige tidsskala, på enkeltpartikelniveau og uden behov for teoretiske modeller, der hjælper med fortolkningen af resultaterne.

# Contents

# List of Abbreviations

**Ak** . . . . . Alkali
**BBO** . . . . . Barium Borate
**CEI** . . . . . Coulomb Explosion Imaging
**DMSO** . . . . . Dimethyl sulfoxide
**ET** . . . . . Electron Transfer
**FFT** . . . . . Fast Fourier Transform
**FT** . . . . . Fourier Transform
**FWHM** . . . . . Full-width half-maximum
**HeND** . . . . . Helium Nanodroplet
**IR** . . . . . Infrared
**KDP** . . . . . Potassium Diphosphate
**Np** . . . . . Naphthalene
**OPA** . . . . . Optical Parametric Amplifier
**RCS** . . . . . Rotational Coherent Spectroscopy
**REMPI** . . . . . Resonantly Enhanced Multiphoton Ionization
**TDDFT** . . . . . Time-dependent Density Functional Theory
**TPX3** . . . . . TimePix3
**UV** . . . . . Ultraviolet
**VMI** . . . . . Velocity Map Imaging

*"And God said: "Let there be light", and there was light."*

— Genesis 1:3.

# 1 Introduction

One of the successes of 20th century chemistry was the development of new techniques for the structural characterization of molecules. Frequency-domain spectroscopy revolutionised chemistry by providing a way to infer molecular structure from light-matter interaction. Learning about how molecules are structured is key to understanding their reactivity, as well as the subtle interactions that take place in a liquid, solid or gas; needless to say, the development of molecular spectroscopy was paramount in the progress of chemistry as a science. Nonetheless, a "static" picture of molecules becomes insufficient as the phenomena under study become more and more subtle. A new revolution came towards the end of last century, driven in great part by technological innovation, when the study of molecular dynamics became technically accessible. The relative delay (compared to other branches of chemistry) in the development of molecular dynamics as a field can be attributed to the inherent difficulty of measuring such processes. One of the reasons why the study of dynamical processes at the molecular level is complex is that molecular changes occur in very short timescales, on the order of $10^{-12}$ to $10^{-15}$ s, and detection systems are limited by response times that are generally a thousand to a million times slower.

Overcoming the technological barrier that kept the timescales of molecular motion inaccessible has fostered a transition from a static to a dynamic picture; this has improved significantly our understanding of chemistry. The revolution that reaction dynamics brings about is not only a refinement of our previous theories, instead, it allows us to stop regarding ourselves as (highly informed) spectators that watch molecule A turn into B and promises us the ability to "steer" the process. This means that knowledge of reaction dynamics upgrades us from mere spectators to active parts that use light as an elegant and effective method to exert control over chemical reactions.

Reaction kinetics is a field that has been around for much longer than reaction dynamics. These two fields, despite the differences that lie in between them, are closely related in the sense that both measure the speed at which a chemical process takes place. It is tempting to differentiate them by pointing out that chemical kinetics follows the macroscopic consequences of what reaction dynamics studies at a microscopic level, but this picture is rather incomplete. In kinetics, molecule A turns into B at a rate $v$, but this model fails to account for the large number of species that may have been formed in the meantime. What we learn from kinetics is therefore sufficient to prepare a given product, but insufficient if we were to fully control the chemical process. In chemical kinetics, the speed at which a reaction takes place is usually characterised by a rate constant, $k$, which depends on the temperature at which the reaction is performed according to the well-known Arrhenius equation:

$$k = Ae^{-E_a/RT} \tag{1.1}$$

This equation, which dates back to 1878 [1], assigns an "activation energy" to the reaction. The activation energy should not be confused with the energy that a reaction absorbs or releases, but rather the amount of energy that a molecule in the ground state should gain in order to reach a reactive state that evolves into products. The excess energy that brings the reactants to the reactive state, named the transition state, is generally provided by increasing the thermal energy available in the environment, or at least this was the traditional way of carrying out a reaction in most laboratories.

Far away from laboratories, a different type of reactions is found to be at the core of life and a myriad of processes taking place on Earth – photochemical reactions. The advent of lasers in the second half of last century opened up an avenue in terms of controlling chemical reactivity efficiently through the use of light. Light packages (photons) with a well-defined energy can be produced routinely nowadays. Contrary to heating up a sample, where a broad distribution of molecular states is populated, light-induced excitation can access well-defined states or a small manifold of states selectively.
The high degree of selectivity of photoinduced reactions gives rise to some of the most sophisticated chemical processes to be observed in nature, such as photosynthesis [2]. In research, the degree of control that light offers can be exploited to study subtle photochemical or photophysical processes that are of interest in many fields of science, as well as a tool to investigate atomic and molecular properties.

Hopefully the virtues of using light to initiate/study reactions are conveyed by now, but there is still one factor that blurs the high selectivity offered by light: the distribution of quantum states imposed by temperature – is it feasible to strip molecules of the ubiquitous thermal fluctuations?

**Table 1.1:** Polarizabilities of some atoms (source: cccbdb.nist.gov)

| Species | Polarizability (in $A^3$) |
|---|---|
| Helium | 0.208 |
| Neon | 0.381 |
| Argon | 1.664 |
| Hydrogen | 0.667 |
| Bromine | 3.050 |

## 1.1 Liquid Helium

Perhaps the word most used in this thesis is "helium". Its properties enable the realization of the experimental conditions necessary to study chemical processes at (ultra-)low temperatures. Helium exists in the form of two isotopes, one with two protons and a neutron ($^3$He) and one with two protons and two neutrons ($^4$He). Helium-4 is the most abundant isotope (>99.999%) and is also the second most abundant element in the universe (hydrogen being the most abundant). Its abundance in outer space contrasts with its relative scarcity on Earth, where it is only found as a trace element. Because of this, helium is not extracted from the atmosphere, but rather distilled from natural gas, where it ends up trapped as a result of radioactive decay of heavier elements.
Helium remained elusive until it was isolated from an impure variety of uraninite (cleveite) in 1895, 27 years after its existence was hinted by a spectroscopic line found in sunlight. Like the other noble gases, it was particularly hard to isolate due to its low reactivity and its odorless and colorless nature.
Helium occurs naturally as a gas, and it was not until 1908 that it was prepared in its liquid form. Down to its liquefaction temperature (4.2 K) it behaves as a normal fluid. Nonetheless, at 2.17 K a second-order phase transition is observed, yielding helium in a superfluid phase. Interestingly, helium remains a liquid even at temperatures close to 0 K, only solidifying if high pressures are applied.
The atomic properties of helium account for its liquid form even at ultra-low temperatures – it has two electrons, which fully occupy its 1s orbital and make it a close-shell system. Its electronic configuration bestows it with a low polarizability of 0.21 $Å^3$ (see table 1.1 for comparison with other atoms), which is lower than any other atom in the periodic table. The low polarizability (and absence of a dipole) is thus key in understanding the very weak potential found for the He-He interaction, as well as that of helium with other molecules or atoms. The weak van der Waals potential and a nuclear spin of 1 for $^4$He can be invoked to account for the liquid nature of helium at temperatures close to zero. Due to its very low polarizability liquid helium interacts very gently with dopants, leaving them nearly unperturbed and hence showing spectroscopic characteristics very close to that of molecules in the gas phase.

## 1.2 Helium Nanodroplets

Some of the characteristics of helium in its superfluid phase are a negligibly low viscosity, high thermal conductivity, and that it remains a liquid even down to temperatures close to absolute zero unless high pressures are applied. This makes it an ideal matrix, but it does not come without drawbacks. As mentioned earlier, the interaction of dopants with the helium matrix is very weak, which causes aggregation of the impurities. As a result, impurities coagulate on the walls of the container and significantly hinder its use as a cryomatrix.
A solution to this problem consists of substituting bulk liquid helium by a flow of nano-sized helium droplets (HeNDs), which can be considered "wall-less nano-vessels". This approach had previously been employed for other noble gas clusters [3] and was first applied to helium clusters in 1990 [4]. Impurities generally have a bound state in the center of the droplet, although in a few cases, namely that of the alkali metals and (to a lesser extent) the alkaline earth metals, the dopants remain at the surface instead of entering the droplet due to their outstandingly weak interaction potential with helium. Regardless of whether the dopant binds to the surface or the interior, the use of droplets overcomes the aggregation problem observed in bulk helium and serves as a starting point for all the experiments presented in this thesis.

### 1.2.1 What is the Temperature of Helium Nanodroplets?

A striking property of liquid helium is that it can attain extremely low temperatures while still remaining liquid. Low temperatures are desirable in spectroscopy, as molecules are stripped off of thermal effects that would otherwise make the interpretation of molecular spectra more difficult.
However, since helium nanodroplets are finite systems, it cannot be assumed that helium nanodroplets share all properties with liquid helium, and their properties have been (and still are) subject of experiments and theoretical studies. The earliest measurement of the droplet temperature was achieved in an experiment concerning the rotational spectrum of $SF_6$ in nanodroplets [5].
Rotational spectroscopy is common for gas-phase molecules but generally inaccessible experimentally for molecules in solution. The frequent collisions experienced by molecules in solution bring about the decoherence of rotationally excited molecules. However, the superfluid nature of liquid helium, further discussed in the next section, allows the observation of fine structure in the rotational spectra, as is the case for bare $SF_6$ molecules. The rotational structure of the $\nu_3$ vibrational transition of $SF_6$ was fitted to a Boltzmann distribution and the authors assigned a temperature of $0.37 \pm 0.05$K, which fit well with previous theoretical predictions [6].

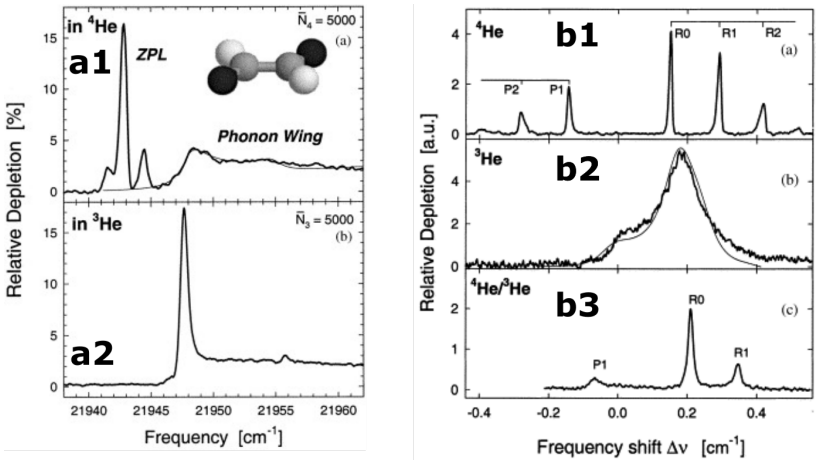


**Figure 1.1:** (a1-a2) Electronic spectrum of glyoxal molecules embedded in $^4$He (a1) and $^3$He (a2). The characteristic gap between the zero phonon line and the rise of the phonon wing, known as the phonon gap, is manifested only for the superfluid. (b1-b3) rotational spectrum of OCS in $^4$He (b1), $^3$He (b2) and in a mixture of $^4$He/$^3$He containing 60 atoms of $^4$He (b3). See text for details. Figure adapted from [7].

### 1.2.2 Do Helium Nanodroplets Preserve Superfluidity?

Superfluidity and superconductivity are two exciting properties, discovered during the last century, whose inner workings still fascinate the scientific community and are an active area of research in multiple fields. Part of this excitement stems from the fact that superfluids show at a macroscopic level a property that is (with the exception of superfluids themselves) normally only encountered in the microscopic world: quantization. Despite the well-established superfluidity of liquid helium, nanodroplets are finite systems and do not necessarily share the features of the bulk fluid. In a paper by Hartmann et al. from 1996, the first experimental evidence of superfluidity in helium-4 nanodroplets was shown as a manifestation of the elementary excitations of the fluid in the phonon wing observed in the electronic excitation of glyoxal molecules [8]. The excitation spectrum of liquid helium in its superfluid phase is one of the characteristics that differentiate it from normal fluids and the observation of this spectrum is generally accepted as indicative of superfluidity. Namely, phonon wings are a consequence of coupled transitions between the host molecule and the matrix [9]. The gap in the spectrum is therefore indicative of an absence of solvent excitations up to 6 cm$^{-1}$, which implies that the solvent does not couple effectively with particles bearing less energy than its lowest excitation; this is indicative of superfluidity, as it implies that there is an energy range for which no solvent excitations are available and as such a particle can move through it without dissipating energy i.e., in a frictionless manner.

Realizing that helium-4 nanodroplets are superfluid raises an interesting question – how large does a droplet need to be to become superfluid? In an experiment carried out by

Grebenev et al. [10] a gradual inclusion of $^4$He atoms was done by doping OCS molecules in a $^3$He nanodroplet and progressively adding $^4$He atoms to see when does superfluidity arise in the form of resolved rotational structure. The rotational structure for OCS molecules embedded in $^4$He is shown in fig.1.1b1, and the structureless spectrum for $^3$He droplets in fig.1.1b2. Finally, panel 1.1b3 corresponds to the smallest amount of $^4$He atoms for which fine structure is reestablished. This elegant experiment can be taken as a further confirmation of the superfluidity of helium nanodroplets and sets a boundary of 60 atoms for the appearance of superfluidity in helium-embedded OCS molecules. The number of $^4$He atoms required to encounter superfluidity is of 60 atoms which corresponds well with the 64 atoms predicted by different theoretical studies [11, 12] and matches the number of atoms expected to form two solvation shells around the OCS molecule.
Yet another consequence of superfluidity is the formation of quantized vortices. Quantum vortices appear upon an increase in angular momentum of the droplet and are known to exist only in superfluids. Despite the difficulty of measuring the presence of vortices in helium nanodroplets, this was achieved in 2014 by doping helium nanodroplets with xenon clusters that become trapped in the vortices [13]. The Bragg patterns arising from xenon clusters were used as an indirect way to image the vortices.

### 1.2.3 Helium Nanodroplets as Nanocryostats

The use of HeNDs as nanocryostats is one of their most attractive applications. Several experiments that chase this goal can be found in the literature, although none of them has approached chemical dynamics with time resolution. Arguably the most outstanding example of a chemical reaction in helium nanodroplets is the formation of barium oxide from reacting barium and dinitrogen oxide [14]:

$$\mathrm{Ba} + \mathrm{N_2O} \longrightarrow \mathrm{N_2} + \mathrm{BaO^*}$$

this reactions produces BaO in an electronically excited state. $\mathrm{BaO^*}$ can release its excitation by emitting a photon, in a process named chemiluminescence (a chemical reaction resulting in highly excited products that undergo radiative relaxation). The light originating from the product was used as a probe for the reaction, as it carries information about the vibrational state of the products formed.
One finding from this experiment was that the emission lines of BaO included hot lines [15], implying that the barium oxide formed was lacking either an efficient relaxation mechanism to dissipate its excess vibrational energy or the time for this to occur. The long time delay between the reaction and the detection of emitted light (generally on the order of microseconds) pointed towards the first option, which brought the authors to suggest that the reaction takes place on the surface of the droplet. The addition of xenon clusters in the bulk of the droplet prior to the reaction showed a suppression of the emission lines corresponding to vibrationally excited states. This was interpreted by the authors as the xenon effectively dragging the barium atom to the bulk of the droplet, where vibrational relaxation can take place.

The possibility of changing the solvation state of the dopants by including other dopants or by exciting with light will be useful when designing bimolecular reaction schemes to be performed in helium nanodroplets, since the possibility to trigger the reaction with light opens the door for time-resolved studies of chemical reactivity.

Electron transfer reactions are promising candidates to be studied in helium nanodroplets. The theoretical study of an electron transfer reaction between cesium and fullerene has been performed by Lara-Castells et al.[16], following experimental observations in mass spectrometric studies of doubly doped droplets [17]. The ab initio calculations indicate that the reaction can proceed through a harpoon-type mechanism i.e., initial submersion of the surface bound dopant (cesium) and eventual transfer of an electron once the right distance to fullerene is achieved. However, the simulation concludes that while this reaction is possible for the cesium dimer ($Cs_2$), the probability is "negligibly small" for atomic cesium, an assessment that corresponds well with the results from the experiments carried out by Renzler et al. [17].

### 1.2.4 Formation of Weakly Bound Complexes

The ability to control the interaction between molecules and assemble them to form supramolecular structures, or molecular complexes, is central to new developments within chemistry. The importance of studying molecular complexes is important to, for instance, understanding protein-host interactions or interaction of molecules with a metal surface that catalyses a reaction.
The aforementioned examples, especially those of relevance in the context of biochemistry, correspond to rather weak interactions, driven by van der Waals forces. This type of interactions have traditionally occupied a secondary place in chemistry textbooks; they are so weak that other, much stronger, interactions dominate our view of a chemical process. Nonetheless, weak interactions are essential in describing complex processes; their role is most important before the reaction itself i.e., in the formation of the pre-reactive complex (e.g. a protein-host complex). In the gas phase, complexes are formed by three-body collisions, which occurs in the hot regions of the molecular beam and as a consequence, the complexes are formed in conformers corresponding to global minima in the potential energy surface, or in a distribution of geometries, with the most abundant being those lowest in energy. The energetic collisions are also detrimental if weak complexes are to be formed, as the high rate of collisions can destroy the complex if its potential is too shallow.
The picture in helium nanodroplets is rather different: the molecules or atoms are sequentially picked by the droplet, and softly attracted towards its interior by long-range forces that enable the formation of the complex in the interior of the droplet. This picture is different in that the temperature available in the environment is very low, and the complexes are not formed through highly energetic collisions. In practice, this results in the possibility of forming complexes in shallow minima, which are quite exotic

if compared to the conformations that are accessible by any other means, including molecular beams. The resulting geometry of the complex is driven by kinetics (geometry of approach remains), versus the thermodynamic picture prevalent in other methods.

An illustrative example is the experiment carried out by Nauta and Miller, in which electric fields are used to form long linear chains of HCN molecules, instead of the ring-like shapes that are dominant in gas-phase methods [18]. In this regard, it is most likely the group of Roger E. Miller that has contributed with the most impactful experiments on complex formation in helium nanodroplets. Some of his most outstanding contributions include the formation of highly polar water clusters driven by the addition of neon atoms that "seed" the formation of water networks [19], or the formation of water hexamers [20]. In both cases, the structures formed are found to be either less stable than other conformers in the gas phase (water hexamers) or simply unstable (neon-seeded water networks).

Other examples where weakly bound complexes have been formed in droplets include experiments whose main interest lies within the physics of the complex, e.g. its rotational dynamics. Some work on this line has been done in our group [21], by forming extremely weakly bound species such as the sodium dimer in its triplet state, or the sodium trimer. These "molecules" have been studied by means of rotational coherence spectroscopy and the results have allowed, in combination with Coulomb explosion imaging, to retrieve the time evolution of rotational and vibrational wavepackets formed by Raman-type excitation with broad-band pulses.
Work on the dynamics of alkali oligomers on the surface of helium nanodroplets has also been carried out previously by the groups of Frank Stienkemeier and Marcel Mudrich. Some of the works include the study of the vibrational wave packet dynamics of potassium dimers [22] and rubidium dimers [23] on the surface of the droplet, and the dynamics of high-spin alkali trimers [24].

# 2 Methods

This chapter presents some of the technical aspects underlying the experimental setup and describes the methods used for data analysis. It also covers the principles behind the helium nanodroplet machine and the characteristics of the helium nanodroplets.

## 2.1 Helium Nanodroplet Machine

The helium nanodroplet machine used in the experiments presented in this thesis has been described before in other thesis and papers. For a more detailed account of the experimental setup than that presented here, the reader is referred to the literature [25].

## 2.2 Formation of Helium Nanodroplets

A beam of helium nanodroplets is formed by expanding high-pressure high-purity (99.9999%) helium gas into high-vacuum through a 5 $\mu$m orifice. The orifice is located on a 2 mm diameter Platinum/Iridium (95/5) disk, mounted into a hollow copper cylinder through compression against a gold washer. This assembly is referred to as "nozzle". The helium flowing through the nozzle is cooled by means of two cooling stages, which cool the nozzle down to a temperature of 3 K. The nozzle temperature is nonetheless adjusted by two resistors (Farnell, MHP35 470F), which provide heat in order to set up the desired conditions for the expansion. The working temperature is generally between 12-30 K, which is measured by a diode (LakeShore Cryogenics DT-670B-CU) and current-stabilized by a cryogenic temperature controller (LakeShore Cryogenics Model 335). The characteristics of the droplet beam can be tuned by adjusting the stagnation pressure of the helium and/or changing the temperature of the nozzle through

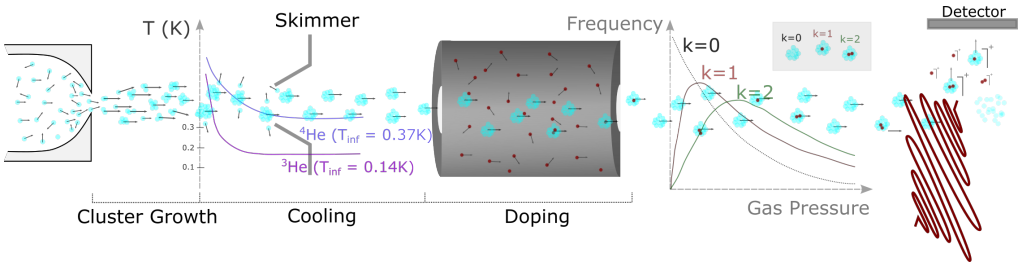


**Figure 2.1:** Pressurized helium is expanded into high vacuum leading to multiple collisions that produce increasingly large clusters as the expansion takes place (cluster growth). The droplets cool down to 0.37 K ($^4$He) before reaching the doping chamber (cooling), where they collide with the gas molecules that act as dopants (doping). Finally, the droplet beam is intercepted orthogonally by a laser beam, which fragments and/or ionizes the dopants.

which the gas is expanded.

Two distinct regimes can be defined following the physical mechanism by which the droplets are formed – supercritical or subcritical expansion. In the supercritical regime, helium is initially in its liquid form and breaks into small droplets made up of $10^5$-$10^7$ atoms (20-70 nm in diameter); this process takes place for nozzle temperatures between 5-10 K and stagnation pressures of 20-80 bar. Increasing the nozzle temperature (12-30 K) leads to a transition to the subcritical expansion regime, where smaller droplets (300-13000 atoms, 30-100 Å in diameter) are formed [26]; the droplets used in all the experiments reported in this text were produced in the subcritical expansion regime. The droplet beams produced in these conditions feature droplet speeds in the range of 200-400 m/s and have a well-defined velocity distribution ($\Delta v/v \approx$ 1-3%) [26].
Once the gas expands through the nozzle, high density regions are created where the cluster growth occurs. After the clusters are formed, they expel helium atoms that carry away 5 cm$^{-1}$/atom [26] and thereby cool the system. Dopants are introduced in the droplet through an oven/doping cell located ca. 60 cm away from the nozzle. At this distance, the temperature of the clusters has asymptotically converged to 0.37 K in the case of $^4$He clusters and to 0.14 K for $^3$He. All the helium droplet experiments carried out in this thesis are performed using $^4$He droplets.

The subcritical expansion of helium is a statistical process, meaning that the resulting droplets have a distribution of sizes [27]. It is important to take this into account in the interpretation of experimental results, as it will be shown later. The distribution can be described by:

$$f(N) = \frac{1}{N\delta\sqrt{2\pi}} \exp\left[ -\frac{(lnN - \mu)^2}{2\delta^2} \right] \tag{2.1}$$

where $N$ is the number of atoms per droplet and $\mu$ and $\delta$ are parameters characteristic of the log-normal distribution, with $\mu$ representing the mean and $\delta$ the standard deviation. The distribution can be expressed in terms of droplet radius, but expressing the droplet

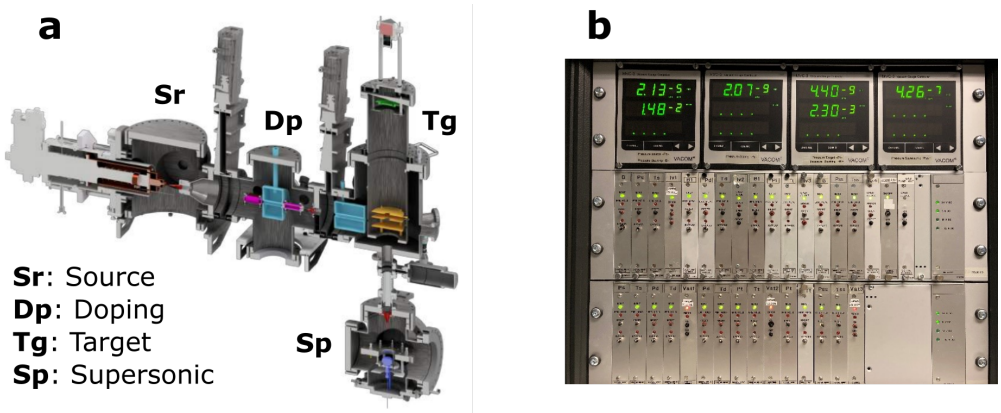


**Figure 2.2:** (a) schematic representation of the helium droplet machine and the different chambers that compose it and (b) picture of the integrated control panel showing typical pressures (in mbar) for the different chambers.

size distribution in terms of number of atoms is illustrative when considering the energetics of a process, given that the nanodroplet maintains a constant temperature by expelling helium atoms that carry away 5 $cm^{-1}$ each. It follows directly that any dissipative event in the droplet leads to the loss of a certain number of atoms, and taking this into account, it follows that choosing the right droplet size is not only constrained by the size of the dopant but also by the energetics of the process of interest. The choice of droplet sizes should take into account how many atoms are evaporated during a certain photophysical or photochemical process, as energy dissipation can lead to a total depletion of the droplet.

## 2.3 Vacuum Systems

A schematic of the vacuum chambers conforming the helium nanodroplet machine used in our laboratory is shown in fig.2.2. Each chamber has a specific function (growth of helium clusters, doping of the droplets, interaction with the laser) and can be isolated from the others by means of pneumatic valves (VAT Series 108 UHV). All the valves are controlled electronically through an integrated panel (fig.2.2). Closing the pertinent valves makes it possible to isolate a specific chamber, which allows to operate on a specific compartment while keeping vacuum on the rest of the system.
The formation of a helium nanodroplet beam requires expansion into ultra-high vacuum. The required vacuum conditions are achieved by a series of turbomolecular pumps backed by roughing pumps that initiate the evacuation of the chamber at atmospheric pressure. Details on the pumps can be found in table 2.1.

**Table 2.1:** Pumps used in the different chambers of the helium nanodroplet machine. *Shared with the source chamber. †Shared with the doping chamber ‡ Originally 1600 l/s: mounted on CF250/CF160 reducing flanges.

| Chamber | Turbomolecular Pump | Backing Pump |
|---|---|---|
| Source | Edwards STP-iXR2206 (2200 l/s) | Edwards iGX600L (620 $m^3$/h) |
| Supersonic | Edwards STP-iXR1606 (655 l/s)‡ | Edwards iGX600L (620 $m^3$/h)* |
| Doping | Edwards STP-iX455 (450 l/s) | Busch COBRA BA 0100 (85$m^3$/h) |
| Target | Edwards STP-iXR1606 (655 l/s)‡ | Busch COBRA BA 0100 (85$m^3$/h)† |

## 2.4 Pickup of Dopants

The molecules or atoms that are introduced in a helium nanodroplet are generally referred to as dopants or impurities. The process by which the dopant is introduced in the droplet is called doping.

Picking up dopants requires the collision of HeNDs with dopant molecules (or atoms) in the gas phase. The procedure to achieve this is dependent on the nature of the dopant, depending on whether it has a sufficiently high vapour pressure (at room temperature) or it requires heating up the sample to generate significant vapour pressure.

In the case of molecules with low vapour pressure, as it is the case for many solids, the dopant molecules are placed into the chamber inside of a cylindrical ceramic oven that has a tantallum wire wrapped around it and can be heated by connecting the wire to a power supply, which heats up upon circulation of a current through Joule heating. Adjustment of the voltage in the power supply allows for a modification of the vapour pressure of the dopant. The temperature of the ceramic oven, although not reliable in quantitative terms, is measured by a thermocouple placed in contact with the oven. This oven design was used in the experiments presented in chapter 3 (alignment of subphthalocyanine molecules), but was later improved and a new design was implemented.

The new design features a stainless steel short cylinder with two small holes that allow the passage of the droplet beam. One of the improvements of this new design is an easier alignment of the droplet beam through the oven and an easier loading of the solid samples, especially in cases where the dopant requires a special treatment, as is the case for alkali metals (chapter 5). Alkali metals are highly reactive upon contact with atmospheric water and their surface readily gets oxidized in the case of sodium, or ignites in the case of larger alkali metals (Cs, Rb). Due to this, the manipulation of alkali metals must be done in inert conditions and the design of the oven adapted to allow an easy transportation from the glove box where it is loaded to the doping chamber where it must be installed. The safe transportation from the glove box to the chamber is achieved by submerging the alkali metal sample in *n*-hexane, which prevents the metal from having contact with atmospheric water. Given that *n*-hexane is highly volatile, it can be readily removed once inside the chamber by pumping the system from 2-3 days.

Molecules with sufficiently high vapour pressures can be introduced into the chamber by means of an external reservoir. Gas phase molecules from the reservoir evaporate as the reservoir is connected to swagelok tubing that leads into a leak valve (Kurt J. Lesker

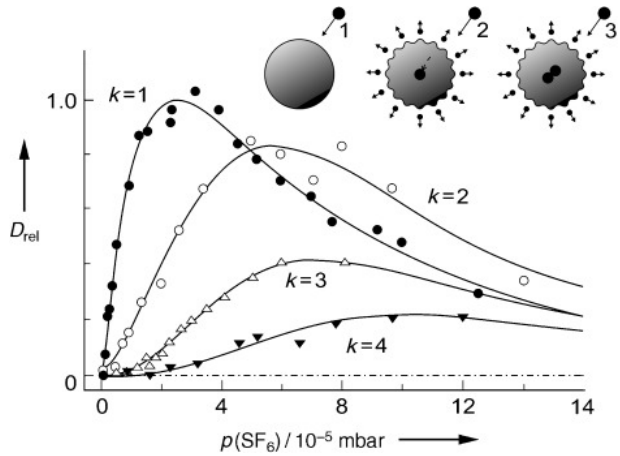


**Figure 2.3:** Probability of picking up $k$ dopants as a function of the dopant's partial pressure ($SF_6$ in this case). Image taken from [26].

LVM Series All-Metal Leak Valve), which has an adjustable opening that controls the flux of gas into the chamber. The leak valve feeds the gas into a "pick-up cell", which consists of a steel cylinder with its axis oriented parallel to the propagation direction of the droplet beam. This geometry maximizes the path of the beam through the doping region and minimizes number of gas molecules that can effuse into the target chamber.

Doping takes place in a statistical manner, meaning that the dopants that enter the droplet follow a distribution roughly imposed by geometrical impact cross-sections, and results in a distribution of the number of dopants in the droplet beam. Two parameters can be adjusted to control the number of dopants per droplet, or rather the probability of having a number of dopants per droplet – the droplet size and the dopant pressure. The doping probability has been found to be described well by Poisson statistics [26].

The Poisson distribution for different k-mers is shown in fig. 2.3, where the fraction of droplets containing k dopants as a function of the dopant's partial pressure is plotted. A good degree of control over the doping conditions can be achieved in the low-pressure limit, in what we call the monomer regime. For low pressures, the dimer contribution is low enough to assume most of the signal comes from monomers (undoped droplets dominate but do not contribute to the signal); however, this comes at the cost of losing signal due to a low amount of doped droplets. Good experimental conditions are found by reaching a compromise between signal and background and depend strongly on the experiment carried out.

A more complex scenario is found if the species of interest is a dimer or higher order complex. In this case, it is unavoidable to have a mixture of species due to the statistical nature of the pick-up process. Distinguishing between ions that stem from monomers, dimers or trimers can be done if the energy channels through which the ions are produced are significantly different in energy. In case that the energetics of the system are not

fully known, data analysis procedures can contribute to determining the order of the complex that gives rise to an ion channel. This analysis can be made, for instance, by covariance analysis. If the ions are formed from the same dissociative event, there will be a correlation (e.g. in angle) between them, but if the ions originate from separate events their distributions will be random.

One additional source of spurious ion counts is gas-phase molecules that reach the target chamber i.e., undoped molecules that effuse to the target chamber. This occurs due to the necessity of having two openings on the oven, which allows gas-phase molecules, with their velocities oriented along the propagation of the droplet beam, to pass through the skimmers and reach the target chamber. The molecules that reach the target chamber without being bound to a helium droplet are referred to as effusive molecules.
One possibility to reduce the effusive molecules reaching the target chamber lies on the design of the oven/doping cell, so that the trajectories that lead to molecules crossing to the target chamber out of a droplet is minimized. Another approach to reduce effusive molecules is installing a cold trap in the doping and target chambers; a metallic container filled with liquid nitrogen that reaches temperatures down to 77 K and condenses any molecule that approaches its surface. If all the measures available are taken and there is still a significant effusive contribution, a filtering procedure can be applied in the data analysis stage. This assumes that the effusive signal is distinguishable from the droplet signal. Fortunately, this is often the case when working with velocity map imaging, as it will be shown later.

### 2.4.1 Localisation of Dopants

So far, a dopant has been considered to be picked-up when it follows the droplet, regardless of its localisation. Nonetheless, in most experiments it is important to establish where within the droplet does the dopant reside. A first consideration is whether the most stable state for the dopant is in the center of the droplet or on its surface. Considering whether the dopant enters the droplet and becomes fully solvated, or stays on the surface, can be initially simplified to the energetic of the process. If a given dopant is found to reside in the center of the droplet, it does so because the energy gained by entering the droplet is larger than the energy needed to create a cavity within the liquid helium.
This ratio is reflected in a dimensionless parameter, $\lambda$, which is often named the "Ancilotto parameter", after Francesco Ancilotto, who introduced the concept [28].
This parameter establishes that for dopants with a value of $\lambda<1.9$ the dopant will remain on the surface of the droplets, while dopants with $\lambda>1.9$ are expected to have a minimum in the center of the droplet. A quick inspection of the values of $\lambda$ provided in the literature [28, 26] reveals that most dopants, whether molecular or atomic, show Ancilotto parameters larger than 1.9, meaning that they reside in the center of the droplet. An exception to this is found for alkali metals, all of which are found to reside on the surface of the droplet, in part due to the repulsion experienced between their

valence $s$ electron and liquid helium. Despite the success of the Ancilotto parameter at predicting the localisation of dopants within the droplet, the validity of the parameter is most appropriate for $\lambda$ values that do not lie close to 1.9. For dopants with values close to this boundary, a more careful analysis of the interaction potential is required to define where in the droplet they are located [29], as it is the case for alkaline earth metals, of which magnesium has been the most widely studied species [30, 31]. In the case of magnesium, the atom is found completely surrounded by helium but nearby the surface, opposed to most dopants which are localized in the center of the droplet.

## 2.5 Laser System

The different optical setups designed for the experiments in this thesis rely on 800 nm pulses delivered by a Spitfire Ace 35F regenerative amplifier. The 800 nm light from the amplifier can be modified in wavelength, time duration and/or polarization by adding optical elements to the beam path. The amplifier is seeded by a Spectra-Physics MaiTai SP oscillator at a repetition rate of 84 MHz and pumped by a Spectra-Physics Empower 45 Q-switched Nd:YLF laser. The output from the amplifier consists of 800 nm pulses with a pulse energy of 5 mJ and 25-35 nm bandwidth. The principle behind the amplifier is chirped pulse amplification, for which the pulses entering the amplifier are initially stretched in order to avoid damaging the gain medium. Once the laser pulses have been amplified, they are either compressed down to around 35 fs or sent out directly with a duration of 160 ps. The amplifier delivers pulses of around 5 mJ at a repetition rate of 1 kHz, with wavelength centered around 800 nm.

## 2.6 Optical Setup

The basic elements of the optical setup are outlined in fig.2.4. The beam is split by means of a thin-film polarizer at Brewster's angle and the power ratio is adjusted by changing the polarization of the incoming light. The transmitted beam is sent to a traslational stage (Schneeberger R-9800), which can be moved to compensate for differences in the distance travelled by each of the beams. Light is thereafter sent to a motorized delay stage (Newport M-UTM100PP), which enables the pump-probe time delay to be scanned during experiments.
Some experiments require the use of 800 nm pulses, but in some others the wavelength must be changed. This is achieved by frequency-doubling (400 nm) or frequency tripling (266 nm) the 800 nm fundamental. If 400 nm pulses are to be used, they are generated by frequency-doubling 800 nm light in a thin barium borate crystal (BBO). A wider range of wavelengths can be achieved by frequency mixing in an optical parametric amplifier (TOPAS), which generates a wavelengths ranging from UV to NIR with the 800 nm fundamental as input.

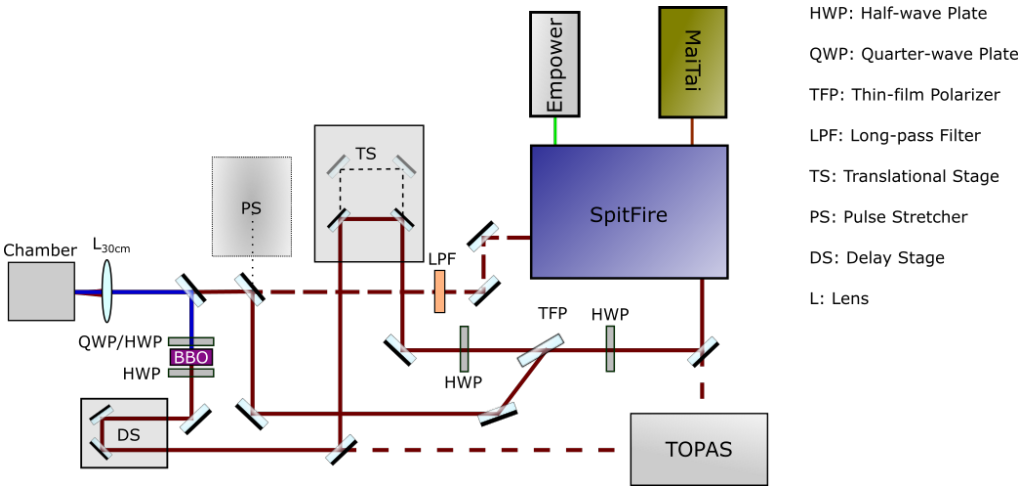


**Figure 2.4:** Schematic representation of the optical setup used throughout the experiments. The dashed lines correspond to alternative beam paths, see text for details.

Alignment experiments generally benefit from longer pulses, which can be produced either by stretching the compressed output of the amplifier by using a pair of prisms or gratings. Alternatively, the uncompressed pulses have been used in adiabatic alignment experiments. When the uncompressed output has been used in this thesis, a long-pass filter with a fast cut-off is used to produced truncated Gaussian pulses of around 160 ps in duration.
A 30 cm achromatic lens focuses the beams into the chamber. The spot sizes at focus used in the experiments presented here are generally found between 25-35 $\mu$m for the probe pulse and 35-40 $\mu$m for the pump pulse. Characterizing the laser pulses is a crucial part of the experiments. Each experiment presented in the chapters to follow has been carried out with different laser conditions and as such the information will be given separately when each experiment is introduced. In what follows some information will be provided about the general characteristics of the optical setups employed in each of the chapters.

### 2.6.1 Alignment experiments

Chapter 3 includes results on the alignment dynamics of carbon disulfide ($CS_2$), molecular iodine ($I_2$) and subphthalocyanine. The first two molecules ($CS_2$ and $I_2$) were nonadiabatically aligned by using the same optical setup: 2.3 ps pulses ($\lambda_0 = 800$ nm) induce rotation of the molecular ensemble and 40 fs pulses ($\lambda_0 = 800$ nm) are used to probe the system by Coulomb exploding the molecules.
The quasi-adiabatic alignment of subphthalocyanine molecules was performed by taking the uncompressed output (160 ps) from the amplifier and applying a long-pass filter with a sharp cut-off to afford truncated gaussian pulses with a slow turn-on and a fast turn-off. The pulse profile is shown in fig.3.11.

### 2.6.2 Photodissociation experiments

Chapter 4 concerns the photodissociation dynamics of molecules in helium nanodroplets. The dissociation of iodobenzene is induced by exciting with 266 nm pulses of ca. 1.2 ps duration. The 266 nm pulses were produced by frequency-tripling the 800 nm output from the amplifier. This was achieved by frequency doubling the 800 nm fundamental to produce 400 nm pulses and frequency summing thereafter the 400 nm with the residual 800 nm light.

The polarization of the 400 nm and 800 nm pulses must be made parallel before they are frequency summed, as they are perpendicular in polarization after the SHG process. Hence that the polarization of the 800 nm pulses is rotated $90^o$ by a wavelength-selective half-wave plate. An additional consideration that must be taken into account is the difference in refractive index between the 800 nm and 400 nm pulses, which leads to a temporal offset as the pulses travel through the crystal. This is corrected for by splitting the two different wavelengths in two separate branches and installing a delay stage in one of them, thus allowing to correct for the temporal difference by changing the distance travelled by the pulses. This can also be achieved by inserting a calcite plate at an appropriate angle, but after trying this approach it was concluded that despite its easier implementation, the calcite plate led to a worse spatial beam profile, which was deemed deleterious for the experiment.

The 266 nm pulses obtained after the procedure described above have a duration of around 120 fs. This pulse duration was found to be unsuitable for the experiment, as the experiment consisted in exciting iodobenzene to the A-band through one-photon excitation at 266 nm. Since the pulses were too short, obtaining a high efficiency for one-photon absorption was challenging due to competing multiphoton processes. Because of this, the pulses were stretched to 1.2 ps to minimize multiphoton process.

The pulses were stretched by means of a pair of prisms at a separation of 80 cm. The characterization of the 266 nm pump is shown in fig.2.5a, as recorded by frequency-resolved optical gating (FROG). It must be noted that the central wavelength indicated in the y axis (200 nm) corresponds to the result of frequency summing 800 nm and 266 nm, which is the optical scheme used to characterize the pulse in the FROG method.

Some of the experiments in chapter 4 make use of (2+1)-photon ionization of iodine by employing different probe pulse wavelengths within the range of 297-307 nm. The probing scheme aims at obtaining high selectivity towards the solvation state of iodine, thus requiring a narrow bandwidth. Selectivity is achieved due to the shift in the electronic structure induced by the surrounding helium, which blue-shifts the absorption of the iodine atom.

However, high spectral resolution comes at the cost of losing time resolution, as narrowing the spectral bandwidth implies the production of longer pulses. The pulses used for this purpose have an approximate duration of 4-5 ps and are generated by frequency doubling 594-614 nm pulses (from the TOPAS) in a thick (40 mm) potassium diphosphate (KDP) crystal. The use of a thick doubling crystal constrains the phase-matching length

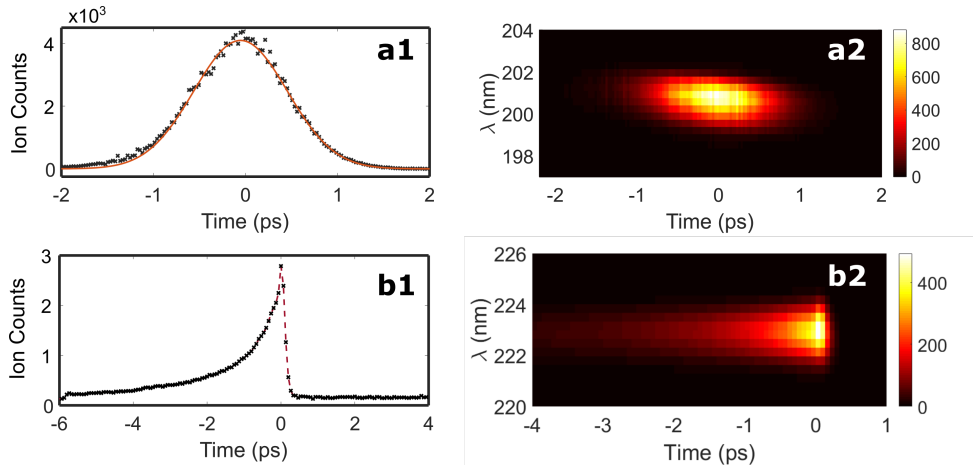


**Figure 2.5:** Characterization of the pump (266 nm, a1-a2) and probe (298 nm, b1-b2) pulses. Column (a) shows the cross-correlation as measured by fitting the ion counts as a function of time for a given wavelength and column (b) shows a colour map of the pulse which contains both spectral and temporal information, as obtained by frequency resolved optical gating (FROG).

to a narrower set of frequencies, hence the narrower spectral bandwidth of the pulses. The FROG characterization is shown in fig.2.5b2. As before, the central wavelength shown in the figure should be understood as the frequency mixing of the probe pulse and the fundamental 800 nm pulse.

### 2.6.3 Alkali co-doping

The optical setup used in chapter 5 consists of a defocused 800 nm beam directly taken from the amplifier. The probe pulse, with a wavelength centered at 800 nm, is focused by means of a 30 cm lens. The defocusing of the pump beam is achieved by including an out-of-focus telescope in the pump beam path. In the experiments where 400 nm probe pulses are employed, they are generated by frequency doubling the 800 nm fundamental by means of a BBO crystal.

## 2.7 Detection Setup

All the experiments exposed here rely on the detection of ions. The ions detected must originate from the interaction with the probe pulse, and must have previously interacted with the pump pulse, in order to carry temporal information. The ions are formed in the region where the molecular beam and the laser pulses cross (interaction region). As shown in fig.2.6, the interaction region is located in between two charged plates (electrodes) named the repeller (further from the detector) and the extractor (closer to the detector). The extractor (E) and repeller (R) are charged with different voltages, forming an electrostatic lens that accelerates (and focuses) ions towards the detector. If

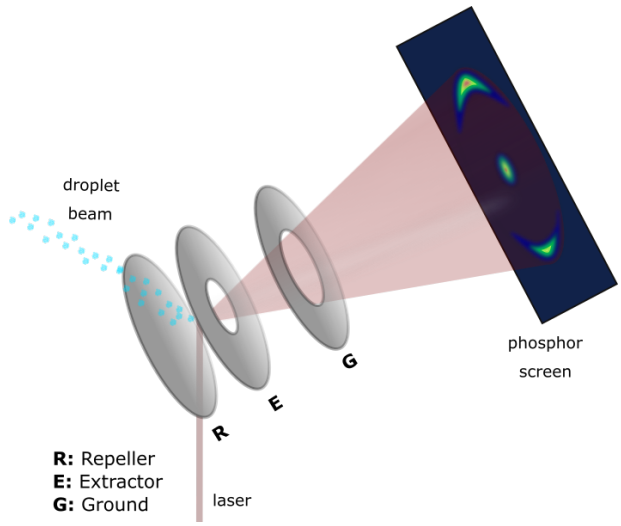


**Figure 2.6:** Schematic representation of the ion optics used in the VMI setup and a hypothetical ion distribution as recorded by the position-sensitive detector (phosophor screen).

the ratio R/E equals approximately 0.65, the ions are focused according to their velocity in the plane of the detector, independently (in the ideal limit) of their initial position; the possibility to obtain information about the energy of a fragment (by measuring its velocity) is what makes VMI detection a powerful tool in the study of molecular dynamics [32, 33, 34].

The velocity of a given ion in the detector plane is mapped into a point of the detector at a distance R of the center. For an ensemble of molecules that bears no preferential spatial orientation, fragmentation into ions of mass $m$ and velocity $v$ yields a ring of radius R. The distance from the center of the detector at which an ion hit is recorded is dependent on its velocity $(v)$ in the plane of the detector and the voltage applied to the repeller.

The ions produced in the interaction region are accelerated towards two microchannel plates (MCP, El Mul Technologies B050V) made up of channels of around 25 $\mu$m in diameter. Ions that impinge on the front of the MCP create a cloud of electrons that is accelerated towards the back of the MCP by a voltage difference of 1.8 kV. This generates an electron cascade with a gain of approximately $10^6$ electrons/ion. The electrons are further accelerated towards a position sensitive detector (P47 Phosphor screen) at a voltage difference of 2.4 kV with respect to the back of the MCP stack. When electrons hit the phosphor screen a flash ($\approx$100 ns), visible to the naked eye, is produced.

The blue light produced by the phosphor is detected by means of a camera. Two different cameras have been used in the experiments presented here, a CCD camera (Allied Vision Prosilica GE680) and a camera with enough time resolution to obtain velocity and time of flight information simultaneously (TimePix3 camera). The CCD camera was used for the experiments presented in chapter 3, and given its lack of time resolution requires

the use of an electrical signal that turns on the detector for ions with a specific time of flight. Gating on ions with a given time of flight is necessary to obtain images of ions with a single charge to mass ratio. On the other hand, the TimePix3 camera does not require gating on a specific time of flight, as it can record images fast enough to record radial and angular information, with an associated time stamp.

### 2.7.1 TimePix3

Chapters 4 and 5 rely on the use of the TimePix3 (TPX3) camera. For the technical details concerning the camera, the reader is referred to the literature [35]. In a nutshell, the TimePix camera enables a wider range of applications in time-resolved helium nanodroplet experiments, because it overcomes the limitation of detecting one single fragment per measurement. This is due to its faster time-resolution (few ns), which allows it to obtain simultaneously spatial and temporal information for a given event. The major practical consequence of this is that contrary to the previously used camera, gating (selecting an ion with a specific time of flight) is not necessary, given that the camera records all the fragments produced simultaneously. Obtaining dynamics for all the fragments produced during a process is advantageous when it comes to extracting information about chemical dynamics, as it will be later demonstrated. In addition, the TPX3 camera overcomes the limited frequency at which the CCD camera could operate (200 Hz). The TimePix3 can operate at the same frequency as the laser (1kHz), which ensures that the image recorded contains no averaging over multiple laser shots.

### 2.7.2 Calibration of the detector

Ions hitting the detector do so at a distance R from the center that is proportional to the velocity on the plane of the detector. The velocity of an ion (v) can be related to the radius (R) at which it impacts the detector by:

$$v = \sqrt{\frac{\alpha R^2}{m}} \tag{2.2}$$

where $\alpha$ is a constant that depends on the voltage applied to the VMI electrodes. The detector constant, $\alpha$, can be calculated by performing an experiment in which ions are produced with well-defined (and previously known) velocities, so that a calibration of the detector can be carried out.
The experiment chosen to calibrate the spectrometer is the photodissociation of molecular iodine ($I_2$). Molecular iodine produces iodine atoms with well defined energies, given that for atoms in a given electronic state, there are no additional internal degrees of freedom (vibrations, rotations) and that its photochemistry has been widely studied. The photochemistry of iodine will be analyzed in more detail later (chapter 4), but for now it must be considered that molecular iodine dissociates to produce two iodine atoms in two possible electronic (spin-orbit) states:

$$(1)\ I_2 \longrightarrow I(^2P_{3/2}) + I(^2P_{3/2}); \qquad D_0 = 12{,}441\ cm^{-1}$$

$$(2)\ I_2 \longrightarrow I(^2P_{3/2}) + I(^2P_{1/2}); \qquad D_1 = 20{,}044\ cm^{-1}$$

The dissociation energies $D_0$ and $D_1$ [36] correspond to the energies of the products in the two different channels with respect to the ground state of $I_2$. The energy of the photoproducts is dependent on the photon energy, but the energy difference corresponds to the spin-orbit splitting of iodine and is therefore independent of the photon energy. Hence that the $D_1$-$D_0$ magnitude is deemed a sufficiently accurate method to calibrate the detector. The ion image used to calibrate the spectrometer is shown in figure 4.3, and will be discussed in chapter 4.
Conversion from the radial space to the energy space is done by extracting a coefficient from the relation:

$$D_1\text{-}D_0 = K(P_{channel2} - P_{channel3})$$

$$K = (D_1\text{-}D_0)/(P_{channel2} - P_{channel3})$$

Which has been calculated to be $K = 1.4547\times10^{-5}$ eV pixel$^{-2}$ kV$^{-1}$.

## 2.8 Data Analysis

### 2.8.1 Image Reconstruction from Velocity Maps

When extracting energies from the ion images recorded, it must be taken into account that the ions are recorded by a 2D detector but are initially distributed in three dimensions (see fig.2.7 for illustration). In order to retrieve the 3D distribution and by extension the real energy distribution, the 2D image is conventionally transformed through Abel inversion of the images [37]. This usually requires the polarization of the laser to be parallel to the detector, in order to ensure cylindrical symmetry.

The reconstruction of the 3D ion distribution shown in this text has been obtained with a different approach than Abel inversion. Instead, the 3D distribution is retrieved by using a maximum entropy algorithm, which iteratively finds the most likely 3D distribution that would give rise to the 2D image recorded. A main advantage of this approach is that it reduces significantly the amount of data necessary to perform the analysis of the ion images, which is advantageous when performing experiments in helium nanodroplets due to their generally low signals. For more details on this algorithm, the reader is referred to the literature [38].

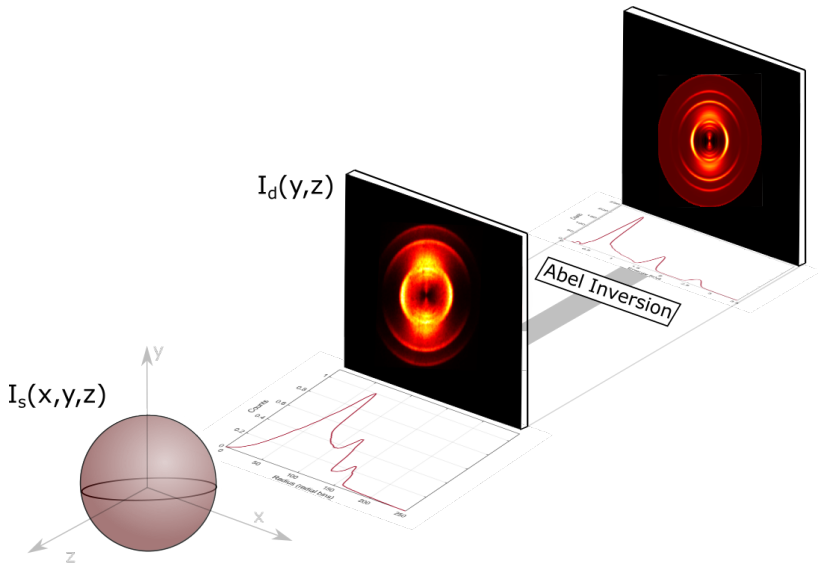


**Figure 2.7:** Scheme representing the projection of the Newton sphere (original 3D ion distribution) into the 2D detector, which gives rise to the 2D projection of the sphere, and its later reconstruction by e.g., Abel inversion.

### 2.8.2 Covariance

A useful tool to analyze the ion images is covariance analysis. Covariance determines whether two events correlate to each other, and thus provides a way to identify fragments that originate from molecules (or atoms) doped in the same droplet. For a more extensive description of covariance, the reader is referred to the literature [39]. A brief description of covariance analysis will be provided.
Mathematically, the covariance of variables X and Y can be written as:

$$cov(X,Y) = E[XY] - E[X]E[Y] \tag{2.3}$$

where E[X] corresponds to the expectation value of X and E[Y] to that of Y. The first term itself is a measure of the correlation of the two variables but can include false correlations. The false correlations are corrected for by the second term, which measures the uncorrelated expectation values. If X and Y are uncorrelated, then E[XY] = E[X] E[Y] and cov(X,Y) will be zero; it must be noted that a null covariance implies only that two variables are uncorrelated through a linear relationship, but could be related through a higher order relationship.

# 3

# Rotational Dynamics of Helium Embedded Dopants

In this chapter experiments concerning the rotational dynamics of molecules in helium nanodroplets are presented. First, a general background is introduced and thereafter Rotational Coherence Spectroscopy (RCS) is proposed as a means to studying the coupling of dopants to the helium solvent. Finally, results on the alignment of a large organic molecule (boron subphthalocyanine chloride) in helium droplets is presented and its potential as a tool in controlling chemical reactivity discussed.
The experiments in section 3.3 (RCS of Helium-Embedded $I_2$ and $CS_2$) were carried out together with Constant Schouder, Adam S. Chatterley and Simon H. Albrechtsen. The theoretical modelling was done entirely by our collaborators from the Institute of Science and Technology in Austria, Igor N. Cherepanov and Mikhail Lemeshko. The section 'Rotational Dynamics in Helium Nanodroplets' is based on the results published in the article "Excited Rotational States of Molecules in a Superfluid", published on the $30^{th}$ of December 2021 in Physical Review A, to which the main contribution has been taking part in the experimental measurements presented in the article.
The experimental results in section 3.6 were recorded together with Adam S. Chatterley. The simulations of rotational dynamics were carried out by using a code created by a former group member (Anders A. Søndergaard), and further developed by other members of the group.

## 3.1 Gas-phase Rotational Dynamics

Molecular rotation illustrates well some of the striking phenomena observed in the microscopic world. In the quantum picture, molecules present no rotation in the classical

sense, but are described by a rotational wavefunction from which its probability to be found in a given orientation can be determined. The rotational states of a linear molecule are represented by a wavefunction that is characterized by two rotational quantum numbers: J, which relates to the total angular momentum, and $m_J$, which corresponds to the projection of J into the molecular axis. Rotational wavefunctions can be determined by calculating the solutions to the rotational Schrödinger equation for a linear rigid rotor, which are spherical harmonics:

$$Y_J^{mJ}(\theta, \Psi) = \Theta_J^{|mJ|_J}(\theta)\Phi_{mJ}(\Psi) \tag{3.1}$$

The values of $\Phi_m(\psi)$ follow $\Phi_m(\psi) = (2\pi)^{-1/2}\mathrm{e}^{\pm im\psi}$, with m values of 0, ±1, ±2, ..., and the values of $\Theta(\theta)$ are determined to a series given by Associated Legendre Polynomials [40].
The probability density (modulus squared of the spherical harmonics) illustrates well the striking nature of quantum mechanical objects – contrary to classical rotation, molecular rotations include areas where their probability density is zero, which from a classical perspective would imply that a molecule in a specific rotational state does not visit all the angles in between 0 and 360° during a rotational period. As counterintuitive as this is if one were to apply the lessons learned from classical physics, this feature of molecular rotations simply underlines the wave-like nature of molecular mechanics.

In practice, following the rotational state of molecules must be done with reference to a known system of coordinates, which we will refer to as the laboratory frame and with relation to which we can follow the evolution of the molecular axes. Each state is given a series of quantum numbers J, K and $M_j$, whose definition will now be briefly introduced for the particular case of a symmetric rotor (i.e., a molecule in which two of its moments of inertia are equal). The quantum number J corresponds to its total rotational angular momentum, K is the projection of J onto the molecular axis, and $M_j$ the projection of J onto a laboratory fixed axis (by convention, the Z-axis). With the quantum numbers just introduced, the energy eigenvalues of the Hamiltonian for a rigid rotor can be found through:

$$E(J, K, M_J) = \frac{[J(J+1)\hbar^2]}{2I_\perp} + \big(\frac{1}{2I_\parallel} - \frac{1}{2I_\perp}\big)K^2\hbar^2 \tag{3.2}$$

Where:

$$\mathrm{J} = 0, 1, 2, \ldots \qquad \mathrm{K} = \mathrm{J}, \mathrm{J\text{-}1}, \ldots, -\mathrm{J} \qquad \mathrm{M}_J = \mathrm{J}, \mathrm{J\text{-}1}, \ldots, -\mathrm{J}$$

The expression of the energy eigenvalues is often simplified by introducing two rotational constants (one for each rotational axis), $\tilde{A}$ and $\tilde{B}$ (in wavenumbers):

$$\tilde{A} = \frac{\hbar}{4\pi c I_\parallel} \qquad \tilde{B} = \frac{\hbar}{4\pi c I_\perp} \tag{3.3}$$

The expression of the energy of the rotational states is thus simplified to:

$$\tilde{F}(J,K,M_J) = \frac{E(J,K,M_J)}{hc} = \tilde{B}(J+1) + (\tilde{A}-\tilde{B})K^2 \tag{3.4}$$

and in the particular case of linear molecules and spherical rotors (all rotation axes are equivalent) the expression is further simplified to:

$$\tilde{F}(J,M_j) = \tilde{B}J(J+1) - \tilde{D}J^2(J+1)^2 \tag{3.5}$$

Where $\tilde{D}$ is the so-called centrifugal distortion constant.

## 3.2 Laser-Induced Alignment

Aligning molecules means fixing the relative geometry of a (the) molecular axis (axes) to axes that are fixed in the laboratory. If the means to impose alignment on molecules is through the use of (laser) light, the laboratory frame is generally defined by means of the polarization vector of light.
When a molecule is subjected to a non-resonant laser field, multiple rotational states can be populated through Raman transitions, which creates a superposition of rotational states, a coherent wavepacket, which can be described as a superposition of field-free rotational eigenstates:

$$\Psi(\theta,\psi,t) = \sum_j a_J(t) Y_J^M(\theta,\psi) \tag{3.6}$$

where $a_J(t)$ represents the time dependent (complex) amplitudes. As mentioned above, the quantum number M is the projection of the total rotational angular momentum onto a laboratory axis.
The fact that there is a phase relationship between the states brings about a non-stationary interference between them, which can be used to extract dynamical information about the molecule.

In the study of rotational dynamics, it is useful to define a magnitude that quantifies the degree of alignment of a molecular ensemble; here, this is done through $<\cos^2\theta>$, where $\theta$ corresponds to the angular distribution of the ions. For illustration, the $<\cos^2\theta>$ value for an ensemble of randomly oriented molecules is 0.33. If the alignment is only considered in two dimensions, as it is the case in VMI detectors, the magnitude used is $<\cos^2\theta_{2D}>$ and has a value of 0.5 for randomly oriented molecules. Values above 0.5 indicate that the molecular ensemble possesses some degree of alignment, with a value of 1 for fully aligned molecules.

Wavepacket dynamics has been a central topic in the field of ultrafast spectroscopy, because populating multiple molecular states (generally rotational or vibrational) brings

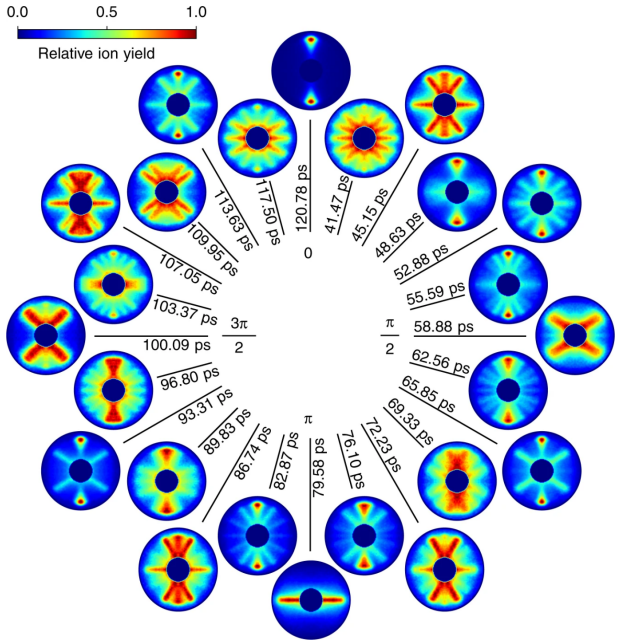


**Figure 3.1:** $O^+$ ion images at different time delays. See text for details on the experiment. Figure taken from reference [41].

the system to a non-stationary state from which dynamical properties of the molecule can be measured. An outstanding example of rotational wavepacket dynamics can be found in fig.3.1. This figure, extracted from a paper by Karamatskos et al.[41], reflects the rotational gas-phase dynamics of carbonyl disulfide (OCS) molecules. The authors use two near-IR pulses (250 fs) to achieve a degree of alignment ($<\cos^2\theta_{2D}> = 0.96$) higher than the theoretical limit (0.92) for a single-pulse experiment. To achieve this degree of alignment, the second pulse is sent 38.1 ps later than the first initial pulse, coinciding with a revival of the molecule. Each image is obtained by detecting the 2D momentum distribution of $O^+$ cations, formed by Coulomb explosion[1] of gas-phase OCS molecules. These beautiful ion images depict what was introduced earlier – that molecular rotations do not follow the angular motion that is to be expected for a macroscopic object.

## 3.3 Rotational Dynamics in HeNDs

The study of molecular rotations in a solvent has been elusive, despite the inherent interest of studying molecular dynamics of molecules in liquids. Experiments in solution are challenged by the high rate of collisions experienced in a liquid environment [42], which dephases molecular rotations, but also by the difficulty of aligning the molecule without perturbing the environment.

[1] the Coulomb explosion technique is covered in section 5.2.2

Helium nanodroplets offer the unique possibility of performing experiments on the rotational dynamics of molecules in a dissipative environment. This is possible partly due to the superfluid nature of helium, which preserves rotational coherence, and partly due to the low polarizability of helium (see table 1.1), which leaves it unaffected by the alignment pulses. In addition and contrary to most fluids, liquid helium is compatible with the high electrical fields used in alignment experiments due to a large ionization potential of 24.6 eV [43].
Given the novelty of alignment experiments in helium nanodroplets, a complete understanding of the interaction between the nanodroplet and rotationally excited molecules is still in progress. Some aspects of rotational spectroscopy in helium nanodroplets have puzzled the community for a while and our recent experiments, in a joint effort with theoretical work performed by Igor Cherepanov and Mikhail Lemeshko from the Institute of Science and Technology (Austria), have contributed to understanding better these systems.

### 3.3.1 Previous Studies on Helium-embedded Molecules

So far, the most widely used technique to study rotations in helium nanodroplets has been IR depletion spectroscopy [44]. Depletion spectroscopy consists on exciting a molecular vibration by using a laser in the IR frequency range. The molecule dissipates its excess energy by coupling with the solvent[2] and results in evaporation of helium atoms. The helium nanodroplet is hence "depleted" when the frequency of the IR laser is resonant with a molecular vibration and monitoring the loss in mass of droplets as a function of laser frequency provides a high-resolution IR spectrum of the dopant. Despite its high-resolution, the technique lacks time resolution and furthermore, selection rules of IR transitions constrain the scope of spectroscopy techniques with high-resolution on the frequency domain due to the selection rule:

$$\Delta J = \pm 1 \tag{3.7}$$

which states that rotational states that can be accessed are limited to one quantum number above the highest state populated at room temperature. This limitation is particularly stringent in the helium matrix, which has a temperature of 0.37 K, and therefore limits the scope of the technique to only a few rotational states.

Accessing energy states that are higher in energy than those accessible by IR spectroscopy is of particular interest for helium-embedded molecules because, as mentioned above, helium nanodroplets are interesting matrices to perform low-temperature spectroscopic studies in a dissipative medium. Nonetheless, some considerations must be taken into account in this regard. As shown in fig.1.1, helium nanodroplets have a low density of

[2] when this is possible, as it has been previously discussed

states up to 6 $cm^{-1}$, resulting in a gap in the excitation spectrum. The first excitation (6 $cm^{-1}$) is termed "roton" and the low density of states region below the "roton gap". The lack of acceptor states in the energy range that spans the roton gap means that the coupling between the molecule and the droplet in that range is weak, as manifested in the narrow linewidths compared to any other spectroscopic matrix [26]. The rotational transitions observed for most molecules at the temperature of the droplet lie in the phonon gap, consequently failing as a means of studying the relaxation of rotational states in a dissipative medium. Due to a lack of experiments on molecules rotationally excited states that lie above the phonon excitation, the coupling of rotationally excited molecules and liquid helium is not well understood.

Rotational Coherence Spectroscopy relies on the use of intense laser pulses that can excite molecules to highly excited rotational states through subsequent Raman transitions. This opens up the possibility of studying the relaxation of rotational states excited above the roton gap, and thus study the interaction between rotationally excited molecules and superfluid helium.

## 3.4 Rotational Coherence Spectroscopy

As introduced before, the energy levels of linear molecules can be described by equation 3.5, where B and D are molecule-specific parameters that suffice to reproduce the molecule's rotational energy structure. B and D parameters are routinely extracted from frequency-domain IR measurements [45] by fitting the peak frequencies to an expression derived from eq.3.5. In what follows, Rotational Coherence Spectroscopy (RCS) will be introduced as an alternative method and RCS experiments on gas-phase methyl iodide will be presented as an example.

### 3.4.1 RCS of Molecules in the Gas Phase

When a molecule interacts with the laser light used in frequency-domain IR spectroscopy, a transition to a well-defined quantum state is achieved. This means that if the molecular orientation were to be followed by, for instance, recording the time evolution of $<\cos^2\theta_{2D}>$, no dynamics are to be expected.
On the other hand, rotational coherence spectroscopy makes use of spectrally broad laser pulses that populate a manifold of rotational states through Raman-type transitions, forming a coherent superposition of rotational states, or rotational wavepacket, whose dynamics can be related to the energy difference between the rotational states forming the wavepacket. Since the time evolution of the rotational wavepacket is determined by the frequencies that compose it i.e., the manifold of rotational states that have been populated, the Fourier transform of the time-domain signal provides a frequency spectrum

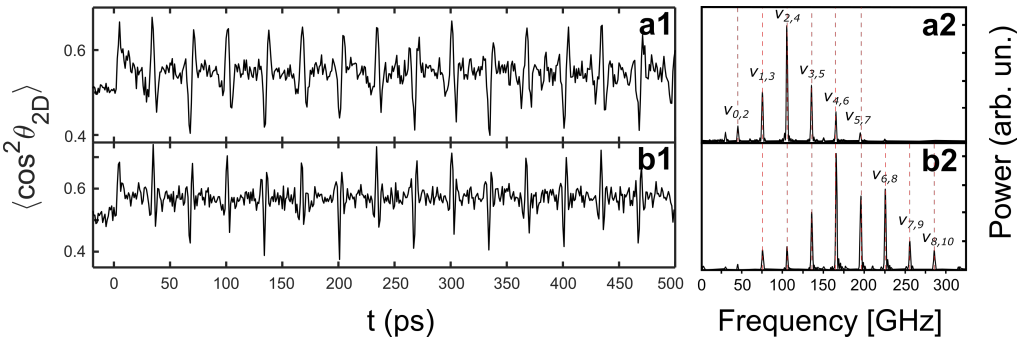


**Figure 3.2:** Temporal evolution of $<\cos^2\theta_{2D}>$ for pump intensities of (a1) 9.845 TW/cm$^2$ and (b1) 16.74 TW/cm$^2$. Their corresponding power spectra are shown in (a2) and (b2).

that contains the "beats" between the rotational states that form the wavepacket. In what follows, the principle of RCS will be illustrated with experiments carried out on methyl iodide.

A molecular beam of methyl iodide was generated by supersonic expansion using an Even-Lavie valve [46] operating at 200 Hz and a pulse length of 7.5 $\mu$s.
The time evolution of $<\cos^2\theta_{2D}>$ for methyl iodide was recorded in a pump-probe experiment, where the molecules were nonadiabatically[3] aligned using 800 nm pulses of 160 fs duration and pump intensities in the range 0.7-2.3$\times10^{13}$ W/cm$^2$. The molecules were Coulomb exploded with an intense probe pulse (3.2$\times10^{14}$ W/cm$^2$), and the resulting fragments were imaged by means of a VMI detection setup.
The frequency spectrum was obtained by applying a Fast Fourier Transform (FFT) algorithm to the alignment trace. In order to improve the FFT, the data was interpolated to obtain a constant sampling frequency and zero-padded to obtained a smaller frequency bin size.
The data shown in fig.3.2 corresponds to two experiments carried out for different pump intensities. The intensity determines the likelihood of multiple Raman transitions, with higher intensities leading to population of higher lying states. Fig.3.2.b1 (higher intensity) shows coherences with narrower revivals than those shown in fig.3.2.a1 (lower intensity), which is a first indication of a larger number of frequency components and thus that a higher number of rotational states have been populated.
This is more easily seen in the power spectra, shown in fig.3.2.a2 and fig.3.2.b2. The spectrum corresponding to the higher intensity trace (fig.3.2.b2) shows a larger number of peaks, which are also shifted towards higher energies. The peaks observed in the spectrum reflect coherences between rotational states in the wavepacket formed by the pump pulse. Only coherences between levels with $\Delta J = \pm 2$ have significant amplitudes due to negligible coupling elements with other states [48].

[3] for nonadiabatic alignment, the alignment pulse is shorter than the rotational period of the molecule, for details see ref.[47]

The frequency at which peaks appear can be related to the difference in energy between two rotational levels. As such, by plotting the transition frequencies as a function of the initial J levels, the B and D constants can be calculated through :

$$\nu_{(J,J+2)}(J) = B(4J+6) - D(8J^3 + 36J^2 + 60J + 36) \tag{3.8}$$

where $\nu_{J,J+2}$(J) is the frequency of a given coherence between states with $\Delta$J = $\pm$2. Fitting the peaks in the power spectrum as a function of J gives a B constant of 7.51 GHz, which is consistent with what has been reported in high-resolution IR spectroscopy studies [49]. A value for the centrifugal distortion constant could not be extracted from this experiments; the small value of D requires excitation to higher J values. The data obtained in this experiment was, nonetheless, considered sufficient as this is only shown as a proof of concept for RCS; our final goal is to carry out measurements in helium-embedded molecules, as it will be shown in the next section.

### 3.4.2 RCS of Molecules in Liquid Helium

Rotational spectroscopy experiments of molecules embedded in nanodroplets have shown that the energy of the rotational states of dopants in HeNDs can be fitted to the same equation as gas-phase molecules, provided that the D and B constants are renormalized (often expressed as $B^*$ and $D^*$ when referring to the values for helium-embedded molecules). In the case of light rotors such as hydrogen fluoride (HF), the rotational constant for helium embedded molecules is found to be very close to that of gas-phase HF ($B/B^*$=1.02). However, for heavier rotors, the rotational lines are found to appear at decreasingly lower intervals, indicating a smaller rotational constant. For instance, the $B/B^*$ ratios for OCS, $CO_2$ and $SF_6$ are found to be 2.78 [50], 2.53 [51] and 2.68 [5], respectively.
The ratio in rotational constants provides structural information about the change in moment of inertia for helium-embedded molecules brought about by the microsolvation environment but nonetheless, dynamical studies must be carried out to study whether the rotational motion of molecules in helium is analogous to gas-phase molecules (with the aforementioned change in rotational constant) or its interaction with helium modifies its dynamical behaviour.
Building on the recent demonstraton of RCS as a tool to study rotational dynamics in liquid helium [52], results on the RCS of helium embedded OCS will be presented as an illustration of the technique, and as a starting point for the discussion of how does the helium environment affect the rotational properties of molecules.
In this experiment, OCS molecules are subjected to an 800 nm laser pulse of 15 ps duration ($4.67\times10^{10}$ W/cm$^2$), thereby triggering a dynamical response through the formation of a rotational wavepacket. The time evolution of the molecular orientation is followed by sending an 800 nm pulse of 40-fs duration ($6\times10^{14}$ W/cm$^2$), which Coulomb explodes the molecule. The time evolution of the molecular orientation is followed by recording the $S^+$ fragments up to 400 ps time delay (fig.3.3a). As shown earlier for methyl iodide,

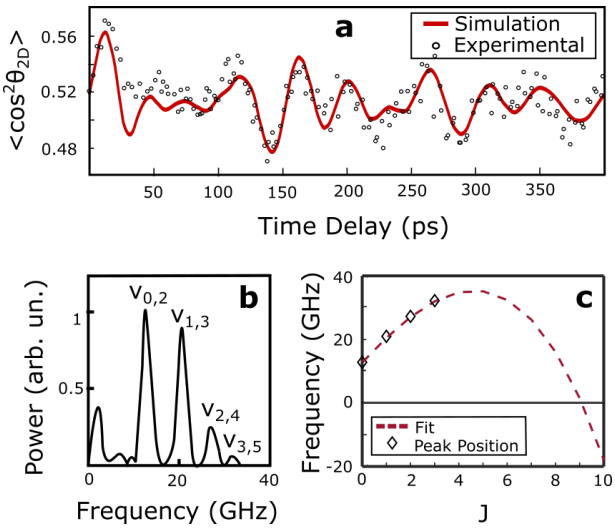


**Figure 3.3:** (a) Time evolution of $<\cos^2\theta_{2D}>$ of helium-embedded OCS as experimentally determined by measuring the angular distribution of $S^+$ (black circles) and simulated by solving the time-dependent Schrödinger equation for an isolated molecule (in red) (b) power spectrum obtained from the Fourier transform of the experimental data (c) peak positions as a function of J and fit to eq.3.8.

the rotational coherences that bring about the time evolution of the wavepacket can be extracted by Fourier transforming the alignment trace. The resulting power spectrum is shown in fig.3.3b, where four coherences are observed. Fitting the peaks to eq.3.8 (fig.3.3) gives a B value of 2.18±0.10 GHz and a centrifugal constant, D, of 9.69±3.26 MHz. A more accurate determination of the constants can be done by populating a larger number of rotational states. This is reflected in the lower uncertainties reported in the literature [52].
For comparison, measurements done by means of depletion spectroscopy [50] report a value of 2.19 GHz for B and of 10.0 MHz for D, which lie well in agreement with the values reported here. In the same work, the authors report a gas-phase rotational constant of 6.08 GHz for OCS, 2.78 times larger than the value in helium nanodroplets. The increase in rotational constant is assigned to 6 helium atoms positioned around the OCS molecule. The helium atoms affect the rotational constant by increasing the molecule's moment of inertia, provided that the rotational frequency is low enough that the helium atoms can "follow along". If enough energy is provided to the molecule, the helium atoms are found to detach, or "break-free", from the helium solvent [53].

Besides the difference in rotational constant, the dynamics of the molecule are markedly different to the gas-phase dynamics [41]. The distinct revivals observed in the gas-phase (as shown for methyl iodide) become blurred and the alignment trace appears as an oscillatory signal with a much less defined structure. A possible origin for this is

the inhomogenous broadening caused by the distribution in droplet sizes; it has been previously reported that the rotational lines of molecules embedded in helium are affected by the droplet size, as the molecule can couple to the surface modes (ripplons) of the droplet [54]. In effect, the alignment trace results from contributions of molecules with a range of effective rotational constants given that the droplet beam is made up of a distribution of droplet sizes, as it was shown in fig.2.1. In order to explore this, alignment traces are averaged out over a range of B constants and combined by means of a weighted Gaussian function. A varying FWHM of the Gaussian distribution is applied in order to determine which value produces the best fit. For OCS, the best fit (as shown in fig.3.3a) was found for a Gaussian distribution of 13 MHz FWHM. The fit shows that the main features of the alignment trace can be reproduced by applying a contribution from inhomogeneous broadening caused by the droplet and strongly indicate that the coupling between the molecule and the surface modes of the droplet is responsible for the loss of the characteristic rotational features of gas-phase molecules.

Moving on to panel 3.3c, the evolution of the difference in energy between $\Delta J=\pm 2$ states as higher J states are initially populated shows that extrapolating the B and D values obtained for OCS to larger J values (through eq.3.8) predicts two features that are in stark contrast with molecules in the gas-phase: a maximum is to be expected for J=5 and, most strikingly, the energy becomes zero at J=9 and negative thereafter. This plot sets the background for the next section, where the states at which these peculiar features are found will be experimentally accessed by using RCS.

## 3.5 Highly Excited Rotational States of Linear Molecules in HeNDs

Building on the observations presented in the last section, it follows naturally that the RCS technique presents itself as a useful tool to explore the rotational energy structure of highly excited rotors in liquid helium. Further experiments were carried out on carbon disulfide ($CS_2$) and on molecular iodine ($I_2$) in order to investigate the evolution of the rotational energy levels as the molecules are excited to higher lying J levels.

### 3.5.1 Experimental Results

Fig.3.4 summarises the experimental results obtained for $CS_2$ and $I_2$. Analogously to fig.3.3c, both molecules show a maximum and a subsequent decrease in energies if applying eq.3.8 to the experimentally determined B and D constants (green triangles). The experimental data (black squares), however, shows that the maximum predicted is not experimentally observed and that instead, the energies seem to assymptotically converge to a constant value (after J=10 in the case of $CS_2$).

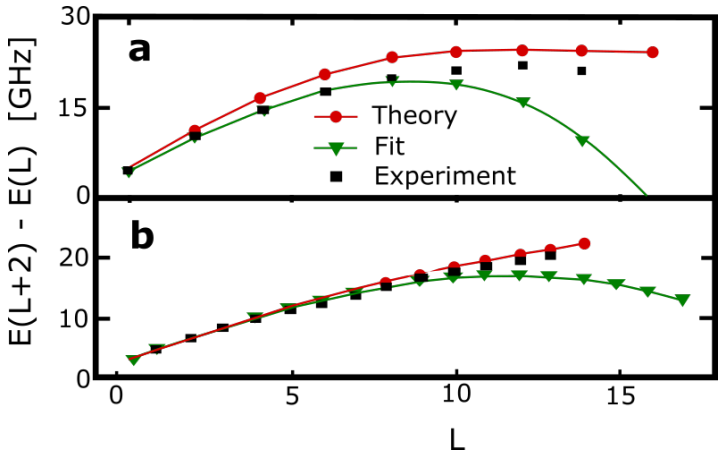


**Figure 3.4:** Frequencies of the coherences (L+2),L for (a) $CS_2$ and (b) $I_2$. The black squares are obtained from the peaks and the red circles are calculated from the theoretical model introduced in [55]. The green triangles are taken from applying eq.3.5 to the B and D values extracted from previous experiments. Figure adapted from ref.[55].

### 3.5.2 Theoretical Modelling: Explanation of the Experimental Results

A theoretical model that successfully describes the results obtained for $I_2$ and $CS_2$, and that shows also predictive power, has been developed by our collaborators in Austria. Even though the theoretical modelling is not a part of this thesis, it provides a framework for the experimental work carried out here. Details on the theoretical model can be found in [55]. The main conclusion from the theoretical modelling of the experimental results is that the rotational energy of molecules embedded in liquid helium can be described well by the amount of angular momentum transferred from the molecule to the helium droplet, causing a divergence from gas-phase behaviour as the energy of the rotational level approaches the energy of a droplet excitation.

## 3.6 Laser-induced Alignment of Boron Subphthalocyanine Chloride

### 3.6.1 Steric Considerations for Chemical Reactions

It has long been established within chemistry that many chemical reactions show a strong orientational dependence [56] (fig.3.5). Despite this, the focus is often set on the energetics of the reaction, averaging the impact parameters over all possible orientations. This approximation is often valid due to orientational averaging imparted by the multiple collisions experienced between the reactants and the solvent molecules. Besides this, the solvent acts as a facilitator of the reaction, serving as a third body that can absorb

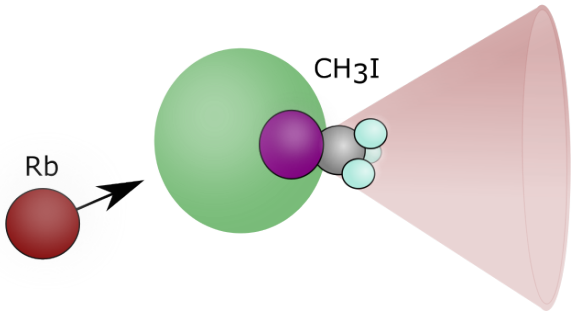


**Figure 3.5:** Schematic representation of the probability of a collision between two reactants (Rb and $CH_3I$) leading to a reactive encounter (forming RbI and $\cdot CH_3$) as a function of the relative orientation of the reactants. The green sphere marks the volume of highest probability and the red cone the angles of approach for which the reaction cannot occur.

excess vibrational energy and bring about a bound state. The orientational averaging and energy provided by the solvent is, however, not applicable to reactions in helium nanodroplets. A temperature of 0.37 K and the superfluid nature of the solvent means that the molecule shows a behaviour analogous to that found in the gas phase, but in the presence of a dissipative environment and at a lower temperature, which enables the formation of weakly bound complexes that can only exist at such low temperatures. When a bimolecular complex is assembled in helium nanodroplets, its conformation is mainly driven by long range forces that assemble the molecules in a specific geometry (section 1.2.4); even if a complex is assembled in a shallow potential energy well it will stay in the geometry of the encounter, given the low energy available in the environment. A direct implication of this is that if the complex is formed in a non-reactive geometry the reaction will not occur, due to the absence of thermal energy that can produce the fluctuations necessary to visit the reactive geometry. Controlling the geometry of a complex is thus paramount in the study of chemical reaction in helium nanodroplets. Laser-induced alignment is proposed as a strategy to overcome this difficulty in some circumstances. As a first step towards this goal, results concerning the alignment of a large organic molecule will now be reported.

### 3.6.2 Alignment of Boron Subphthalocyanine Chloride

Porphyrins are well-known molecules for most chemists, but specially in the fields of organic chemistry and biochemistry. They are classified as heterocyclic macrocycles that feature four pyrrole subunits. They constitute the basic unit of the pigment heme, which is a cofactor of hemoglobin. Hemoglobin takes care of oxygen transport in the vast majority of vertebrates, thereby drawing a significant amount of attention from the scientific community. On a broader scope, porphyrins give name to a family of molecules termed porphyrinoids, which are a large family of compounds that feature porphyrin as its fundamental subunit. Perhaps the most well-known members of the

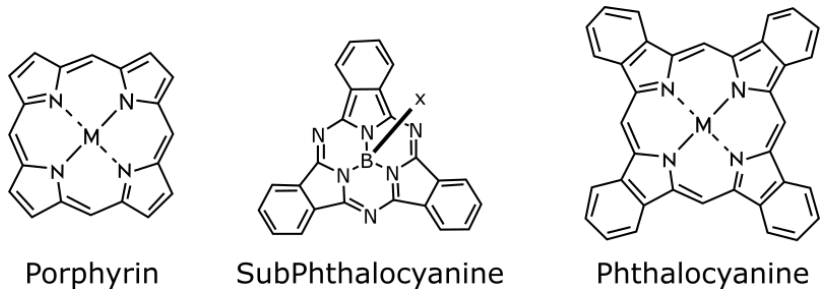


**Figure 3.6:** Three examples of the porphyrinoid family: porphyrin, subphthalocyanine (X: halogen atom) and phthalocyanine (M: metal atom.

porphyrinoids (besides porphyrins themselves) are phthalocyanines. Phthalocyanines can be found as active components of many dyes, including those used as pigments in organic photovoltaic cells. Nonetheless, phthalocyanines are difficult to synthesize and present some challenges such as aggregation, which hamper their application into, for instance, photovoltaic devices [57].
In recent years, a new class of porphyrinoids has gathered interest, namely subphthalocyanines (SubPcs). SubPcs are contracted analogs of phthalocyanine, meaning that instead of four isoindole units they are conformed by only three. Subphthalocyanines are easy to synthetize and are less prone to aggregation, due to the curvature of the aromatic ring, which minimizes $\pi$-stacking [58]. Recently, subphthalocyanines have been used as photosensitizers in Dye-Sensitized Solar Cells [59, 60]. Despite the lower efficiency realized for the SubPc-based devices, the rather low amount of work devoted to understanding their photophysics leaves room for improvement. Additionally, SubPcs present higher stability than many other dyes, which is a commonly encountered problem in the context of organic photovoltaics [61].

Due to their properties, boron subphthalocyanine was envisioned as a suitable candidate in an electron transfer reaction. Achieving the time-resolved study of an electron transfer reaction in HeNDs can be considered a milestone in the development of HeNDs as nanocryostats, but it is also of great interest from the perspective of measuring an electron transfer reaction at a temperature close to absolute zero.
SubPcs are characterized by a large polarizability anisotropy (45 $Å^{-3}$), which is a requirement if orientational control of the molecule is to be achieved through laser-induced alignment. Furthermore, it possesses enough stability to withstand being heated to high temperature in the doping oven used to bring the molecule into the gas-phase prior to introducing it into a helium droplet.
The presence of a chlorine/bromine-boron bond oriented perpendicularly to its aromatic ring provides the molecule with a good observable in VMI experiments: the angular distribution of chlorine/bromine atoms can be directly related to the orientation of the aromatic ring, thus providing a picture of any structural/orientational changes of the

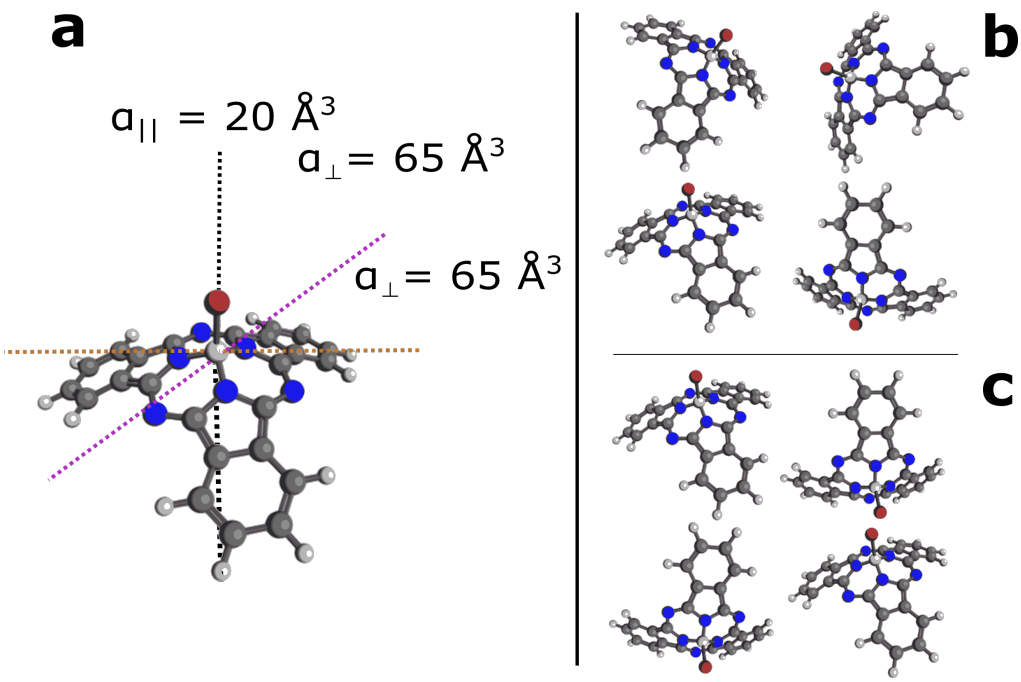


**Figure 3.7:** (a) The polarizabilities of subphthalocyanine along the three different coordinates. The right side of the figure shows an ensemble of (b) unaligned molecules and (c) 1D aligned molecules.

molecule during a chemical reaction or during an alignment experiment. The masses of chlorine and bromine are different from the most common fragments produced in the fragmentation of hydrocarbons and from the most common contaminants in the vacuum chambers ($H_2O$, $O_2$).

### 3.6.3 Structural characteristics of SubPc

A 3D representation of subphthalocyanine is shown in fig.3.7, together with its three rotational axes and their respective polarizability. The molecule belongs to the $C_{3v}$ point group, with the polarizabilities of the axes perpendicular to the $C_3$ symmetry axes being equal. The polarizabilities, calculated at the 6-31+g(d)/lc-wpbe theory level, are shown in fig.3.7. Furthermore, the molecule features two equal moments of inertia perpendicular to the $C_3$ symmetry axis, meaning that the molecule classifies as a symmetric top rotor. The largest moment of inertia is found for the axes perpendicular to the $C_3$ symmetry axis, thus making it an oblate symmetric top.

### 3.6.4 ToF-MS of Helium-Embedded SubPc

The ion fragments produced after ionizing helium-embedded boron subphthalocyanine chloride molecules have been measured by time-of-flight mass spectrometry (ToF-MS).

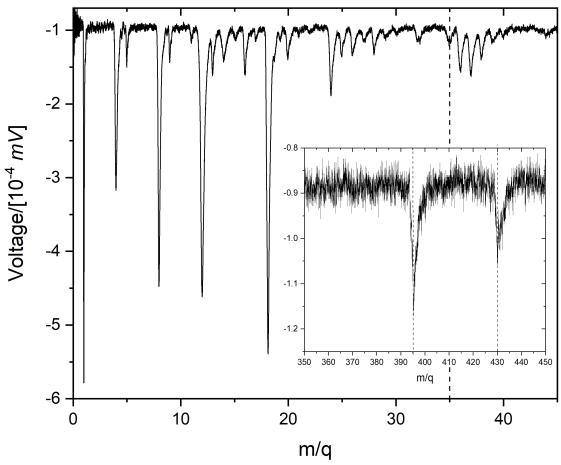


**Figure 3.8:** ToF-MS of helium-dopped BsubPcCl obtained by ionization with a 100 fs linearly polarized, 800 nm, $1.6\times10^{14}$ W/cm$^2$ probe pulse. The dashed lines mark the peaks corresponding to the parent ion (BsubPcCl$^+$,m/q=430), the dechlorinated parent ion (BsubPc$^+$, m/q=395) and the chlorine ion (Cl$^+$, m/q=35).

The presence of a peak at m/q = 430 and m/q = 432 indicates the presence of two isotopes of unfragmented parent molecules (BSubPc$^{35}$Cl$^+$ and BSubPc$^{37}$Cl$^+$). The observation of the parent ion indicates that the molecule does not decompose (or at least a significant part of it does not) when heated in the doping oven, although some fragmentation does takes place, as indicated by the presence of dechlorinated-parent ion (BSubPc$^+$, m/q = 395). However, the loss of a chlorine atom by the parent molecule is likely to occur through interaction with the laser pulse, not as a consequence of the heat applied during the doping process. A signal arising from one of the isotopes of chlorine is also detected (Cl$^+$, m/q = 35) and is chosen as the main observable for the alignment experiments. The $^{37}$Cl$^+$ signal appears close to hydrocarbon fragments, which makes it a worse observable than $^{35}$Cl. Even though there is not, to our knowledge, precedent in doping helium droplets with subphthalocyanine molecules, previous work on similar molecules (phthalocyanine and porphyrin) was carried out by the group of A. Slenczka [62, 63, 64].

### 3.6.5 Ion Images

ToF-MS measurements indicate that the $^{35}$Cl$^+$ ion signal is distinct and intense enough to be used as an observable. Assuming that the axial recoil approximation holds well, the ejection direction of Cl$^+$ can be considered as a measure of the spatial orientation of the B-Cl bond and, by extension, of the whole molecule. The validity of the axial

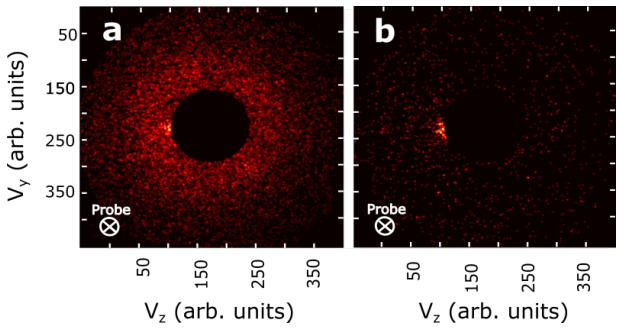


**Figure 3.9:** $Cl^+$ images of unaligned BSubPc molecules. The probe is a 50 fs linearly polarized 800 nm beam ($8.3\times10^{13}$ W/cm$^2$). The polarization is perpendicular to the detector, as indicated in the image. (a) image taken with a helium droplet beam present and (b) with the helium beam blocked. The (black) filter in the central part of the image covers the effusive signal.

recoil approximation relies on the high degree of symmetry of the molecule and on that internal modes (SubPc-B-Cl bending) are not expected to contribute significantly during the dissociation.
A chlorine ion image of unaligned BSubPcCl molecules is shown in fig.3.9. Image 3.9b corresponds to gas-phase (effusive) molecules and 3.9a to molecules embedded in helium nanodroplets (with an average size of 10,000 atoms). The chlorine fragments are produced following multiple ionization of the SubPc molecule:

$$(\text{SubPcCl})^{2+} \longrightarrow \text{SubPc}^+ + \text{Cl}^+$$

which corresponds to the Coulomb channel i.e., multiple ionization of the parent molecule that leads to fragmentation into charged fragments. As it will be argued for more extensively in the next chapter, this dissociation channel provides generally a good dissociation pathway given the simplicity of the Coulomb (point charge-point charge) potential. Assigning the $Cl^+$ fragments to the Coulomb channel can be done on the grounds of the high intensity of the probe pulse ($8.3\times10^{13}$ W/cm$^2$), which makes any other dissociation pathway highly unlikely. A more convincing assignment would require the detection of the $SubPc^+$ and $Cl^+$ ions in coincidence, which is accessible with the detection setup (the TPX3 camera) used in the experiments presented in later chapters, but was not possible for the experiments carried out on this chapter due to the necessity to gate on one specific ion.

In the absence of the helium nanodroplet beam, the ion signal is negligibly low (fig.3.9b), while the signal stemming from molecules doped in helium droplets shows an isotropic distribution of ions, as it is to be expected from a randomly oriented ensemble of molecules ($<\cos^2\theta_{2D}> = 0.5$). A spatial confinement of the molecules is sought after by including an alignment pulse. The pulse profile, shown as a grey area in fig.3.11, is a 160 ps truncated gaussian pulse of 800 nm central wavelength. The truncated pulse is

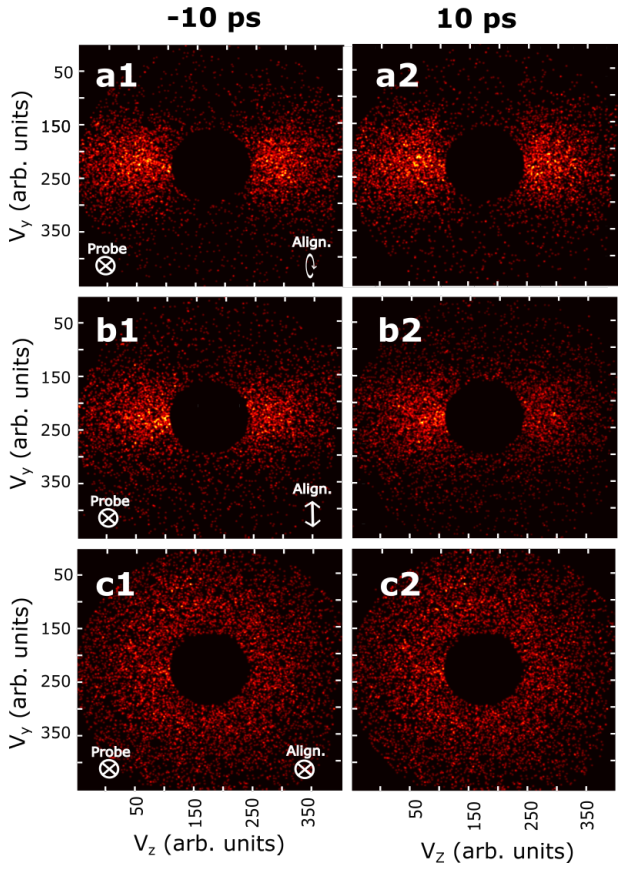


**Figure 3.10:** $Cl^+$ images of BSubPc molecules aligned by an 800 nm 160 ps truncated gaussian pulse. The probe is a linearly polarized 800 nm focused beam ($8.3\times10^{13}$ W/cm$^2$). The polarization of both pulses is indicated in the corner of the image. Images in the left column (a1-c1) are recorded while the alignment pulse is turned on and those in the right column (a2-c2) correspond to molecules in field-free conditions.

characterised by a slow turn-on and a fast turn-off, achieved by frequency filtering by means of a long-pass filter. This method was introduced for gas-phase molecules [65] and extended to helium-solvated molecules later on [66].

The inclusion of the alignment pulse drastically changes the angular distribution of the ions (fig.3.10). As a first example, the case of alignment by means of a circularly polarized pulse will be discussed. The ion distribution obtained by probing 10 ps before (fig.3.10.a1) and 10 ps after (fig.3.10.a2) is in essence the same and as such no differentiation will be made in the discussion.

The ion images show that ion hits become confined along the Z-axis i.e., the laser propagation direction. This observation means that the B-Cl axis is confined along the laser propagation axis and that, as expected, the most polarizable axis (the aromatic ring) is confined to the polarization plane [67]. The case for a circularly polarized alignment

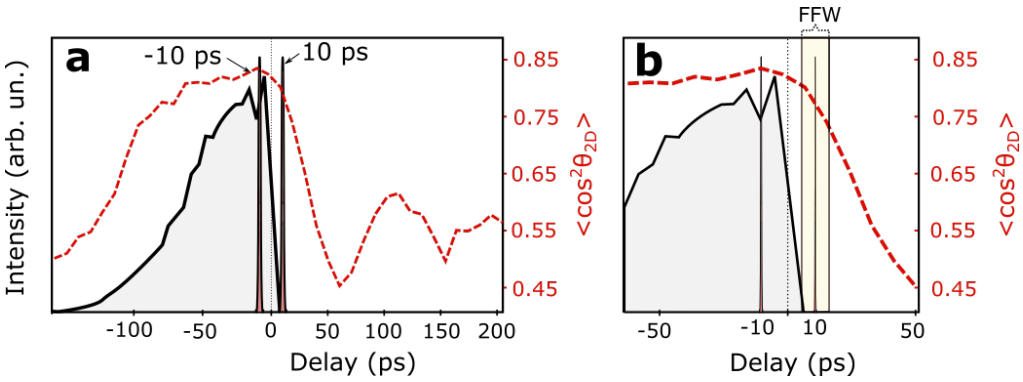


**Figure 3.11:** (a) Time dependence of $<\cos^2\theta_{2D}>$ (in orange) for boron subphthalocyanine chloride molecules embedded in helium, after quasi-adiabatic alignment induced by an 800 nm, 160 ps truncated pulse (in grey in the figure). The time delays corresponding to the field-free and the field-present measurements, as shown in fig.3.10, are indicated by the pulses at -10 and 10 ps (b) zoom in of figure (a) highlighting the field-free window i.e., the range of time delays for which the alignment loses less than 10% of its value after the alignment pulse is switched off.

pulse is illustrated in fig.3.11a. A high degree of alignment is reflected in the $<\cos^2\theta_{2D}>$ value of 0.82, a value that has been shown to underestimate the real degree of alignment [68] for molecules in helium droplets due to scattering of the escaping fragments with helium atoms, meaning that the real degree of alignment achieved is higher than 0.82. Correcting for the non-axial recoil can be done by recording the covariance of the recoil ions, as shown in reference [68]. This requires that the covariance can be measured, as the authors did for molecular iodine, but in the present case the nature of the molecule does not allow for a measurement of the covariance.

A similar ion image is found if the polarization of the alignment pulse is linearly polarized along the Y-axis (that is, parallel to the detector). The polarization along the Y-axis does not confine the aromatic ring to the XY-plane as in the case of circularly polarized light and instead the molecule is free to rotate along the Y-axis, as depicted in fig.3.12b. The free rotation around the Y-axis creates a doughnut shaped $Cl^+$ ion distribution which, when projected into the 2D detector, produces the ellipsoid shown in the figure and observed in the ion image 3.10b.
The effect of the free rotation is more easily seen when the polarization vector is shifted to perpendicular to the detector plane. In this case, as shown in fig.3.12c, the free rotation takes place along the X-axis and leads to the ring observed in the ion images.

We now set ourselves to explore the effect of the alignment pulse intensity in the degree of alignment. To do so, we perform a series of measurements at pump intensities ranging from 0-4.35 TW/cm$^2$, keeping the probe intensity constant at $8.3\times\times10^{13}$ W/cm$^2$. These measurements, shown in fig.3.13, reveal that the degree of alignment is very close to that expected for an ensemble of randomly aligned molecules ($<\cos^2\theta_{2D}>\approx 0.51$ in absence of alignment pulse) and increases with the alignment beam intensity until it reaches

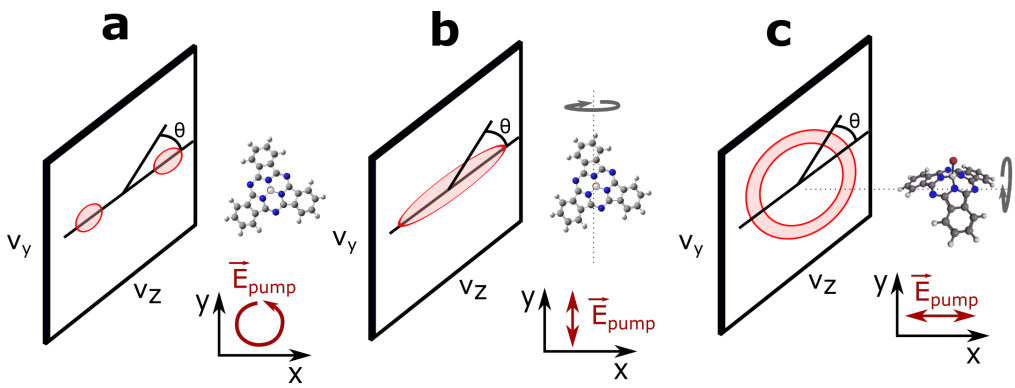


**Figure 3.12:** Scheme showing the alignment of subphthalocyanine molecules for (a) circularly polarized light (b) linearly polarized light with the polarization vector parallel to the detector and (c) linearly polarized with the polarization vector perpendicular to the detector (X-axis). See text for details.

a maximum alignment of $<\cos^2\theta_{2D}> = 0.82$ at 3.11 TW/cm$^2$, where it saturates. As mentioned earlier, this value does not include a correction for the non-axial recoil effect caused by interaction of the escaping fragments with the helium droplet, meaning that the real degree of alignment is higher than that recorded.
With the dependence of the degree of alignment on the intensity in mind, the alignment intensity chosen for the images shown above was of 3.11 TW/cm$^2$. This value was chosen as it produces the highest degree of achievement recorded at the lowest alignment intensity; in this way, the lowest degree of ionization by the alignment pulse is caused without sacrificing the degree of alignment of the molecules.

A last observation concerns the rotational dynamics of the system. The large rotational constants of subpthalocyanine mean that if any revivals are measurable, they will occur at significantly long time delays. An estimation of the time delay for the first revival can be made, if the rotational constant is known, according to:

$$T_{rev} = \frac{1}{2B} \tag{3.9}$$

with this in mind, and using a calculated rotational constant (6-31+g(d)/lc-wpbe) of 0.15026 GHz for the axis perpendicular to the symmetry axis ($B_\perp$), an estimated time of 3.3 ns is expected for the first revival. This time corresponds to the gas-phase revival and therefore a correction factor for helium-embedded subphthalocyanine must be applied. Given that this value is unknown and cumbersome to obtain computationally, a simple constant extracted from molecules of similar size will be applied. As introduced earlier, rotational constants approximately three times lower than the gas phase values have been recorded for molecules in helium nanodroplets. This would correspond to a first revival on the order of 10 ns, which is much larger than the 200 ps time window recorded in this experiment. Despite the limited dynamical information available in this experiment, it

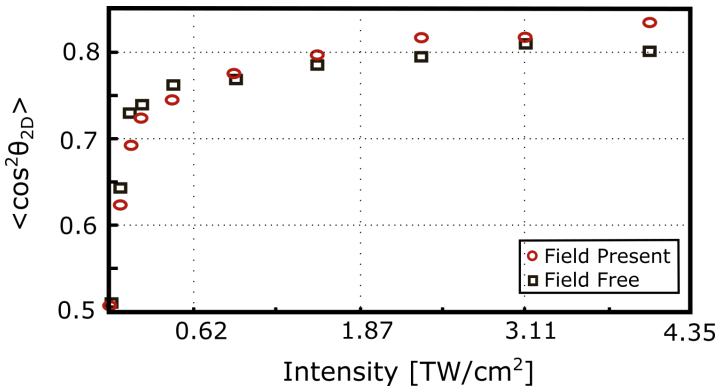


**Figure 3.13:** Dependence of the degree of alignment on the pump intensity, as reflected by the $<\cos^2\theta_{2D}>$ extracted from the $Cl^+$ ion images recorded after inducing alignment of an ensemble of SubPc molecules by means of an 800 nm circularly polarized, 160 ps pulse. The red hollow circles correspond to the value of $<\cos^2\theta_{2D}>$ while the alignment pulse is on, and the black squares to the field-free regime. The probe intensity was kept at $8.3\times10^{13}$ W/cm$^2$ for all the measurements.

is possible to observe clear dynamics after the drop in the $<\cos^2\theta_{2D}>$ value when the pulse is turned off, leading to some degree of anti-alignment ($<\cos^2\theta_{2D}> = 0.45$) at a time delay of 60 ps (see fig.3.11). After 200 ps, the degree of alignment remains at 0.55 indicating some degree of permanent alignment in the molecular ensemble.

### 3.6.6 Alignment-enhanced REMPI Probing

Ionizing molecules and molecular fragments is a requirement to study molecular dynamics with the VMI detection scheme used throughout the experiments presented in this thesis. Furthermore, the optical scheme used to achieve ionization is a key element in the experiments and the choice of colour is determined by experimental requirements and limited by the technical aspects of producing laser pulses. The high intensities achievable with femtosecond pulses makes strong-field ionization schemes routinely accessible, which gives access to ionizing species with high ionization potentials that would otherwise remain inaccessible. Nonresonant multiphoton ionization is, however, not selective and as such can be inappropriate in experiments with multiple dopants in the droplet and can provide limited information as a spectroscopic tool.
Resonantly Enhanced Multiphoton Ionization (REMPI) provides a probing method that has the advantage of selectively probing a species by tuning the laser wavelength to (m+n)-photon ionize a specific atom or molecule. This is possible because at nonresonant wavelengths the ionization probability is so low that it leads to negligible ionization, but when light has the right wavelength it can populate an excited state through an m-photon excitation, and be subsequently ionized by absorption of n photons.

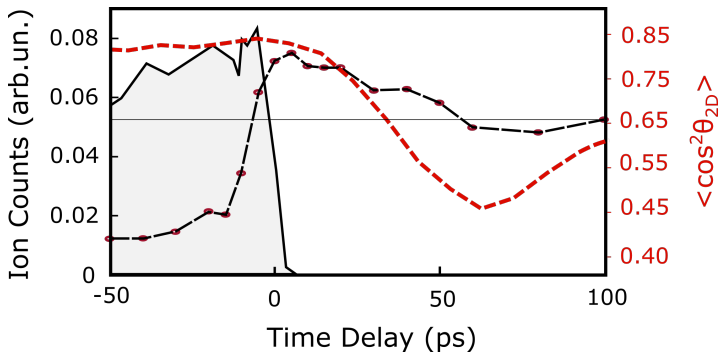


**Figure 3.14:** $BSubPc^+$ ion yield as a function of time (black dashed line). The intensity profile of the alignment pulse corresponds to the grey area and the ion yield in absence of an alignment pulse is shown as a grey solid line. The alignment beam is circularly polarized and has an intensity of 3.11 TW/cm$^2$. The degree of alignment is plotted as an orange dashed line, and is extracted from the angular distributions of $Cl^+$ ions.

Regarding subphthalocyanine, to our knowledge the only absorption spectra available in the literature have been recorded in solution. The absence of absorption data in liquid helium or in gas phase meant that the information for molecules in solution had to be taken as a starting point. The absorption spectrum of SubPc is characterised by two intense bands corresponding to the $S_1 \longleftarrow S_0$ and the $S_2 \longleftarrow S_0$ transitions. In benzene, the spectrum features maxima at 569 nm and at 306 nm [58].
Subphthalocyanines show small stokes shifts and as such its helium-embedded absorption spectrum was expected to be close to that observed in an apolar solvent such as benzene. With this in mind, we scanned the probe wavelength by sending the 800 nm output from the amplifier to an optical parametric amplifier (TOPAS in fig.2.4) in order to generate light in the wavelength range corresponding to the $S_1 \longleftarrow S_0$ transition.
After failed attempts at finding a clear resonance for the lowest energy transition, a BBO crystal was inserted to frequency-double the light produced in the OPA and access the $S_2 \longleftarrow S_0$ transition region. Clear indication of [1+1]-REMPI was found at 300 nm, hence we moved on to investigate the alignments dynamics probed with 300 nm light. The results, displayed in fig.3.14, show two main features; the $SubPc^+$ ion yield in experiments where an alignment pulse was employed (black dashed line) show higher ion yields than those recorded in experiments where only the probe pulse is present (solid grey line) for the first ≈50 ps. The ion yield decreases until it reaches the same value as in the experiment employing only a probe pulse at 50 ps. A second observation is that the ion yield observed in field-free conditions is higher than that observed while the alignment field is present.
Concerning the first observation, further inspection reveals that the increased ion yield, relative to the probe only experiment, corresponds well with the time window where some degree of alignment is found in the molecule (as argued in the previous section). Furthermore, despite this being less marked than the previous observation, the signal

falls below the probe only level as the molecules become antialigned, strengthening the link between the molecular alignment and the ionization probability.
Secondly, the increase in ion yield as the alignment pulse is turned off must be considered. Given that molecules possess an almost constant degree of alignment 50 ps before the alignment is turned off, this cannot be assigned to an alignment effect. Instead, as it has been reported previously [66], the reduction in ion counts when the alignment pulse is present is due to destruction of the parent ion by absorption of photons from the alignment pulse. Even though the neutral molecule does not absorb 800 nm light, cations are known to possess red shifted absorption and absorb 800 nm light leading to destruction of the parent ion through further multiphoton ionization.

As it was discussed earlier and shown in fig.3.12, the circularly polarized alignment pulse confines the aromatic plane of the molecule to the XY-plane and the B-Cl bond aligned along the propagation direction of the laser pulse (Z-axis). Given that the probe pulse is linearly polarized and perpendicular to the detector plane, the increase in ion yield observed for the aligned molecule indicates that the transition dipole moment of the $S_2 \longleftarrow S_0$ transition is located in the aromatic ring, as can be concluded from the dependence on the probability of ionization and the relative orientation of the transition dipole moment with respect to the polarization vector:

$$P \propto (\vec{E} \cdot \vec{\mu})^2 \tag{3.10}$$

where $\vec{E}$ is the polarization vector and $\vec{\mu}$ the transition dipole moment. Following this relation, resonant probing in conjunction with laser-induced alignment can be employed as a method to gather structural information about the transition dipole moment of a specific electronic transition.

# 4

# Photodissociation of Helium Embedded Molecules

In this chapter experiments concerning the photodissociation of helium-embedded dopants are presented. First, a general background concerning photodissociation of molecules will be provided, starting from the case of photodissociation of gas-phase molecules. Finally, results concerning the photodissociation of molecules in liquid helium will be presented. The experiments on the photodissociation of molecular iodine were carried out together with Adam S. Chatterley, and the experiments on iodobenzene in collaboration with Constant Schouder.

## 4.1 Photodissociation Dynamics

As mentioned in the introduction, the use of light to steer chemical reactions is perhaps the Holy Grail within physical chemistry. The unique degree of control that light offers is due to the nature of light itself. As the element that unveiled the revolution of quantum physics, light is known to come in "packets" or quanta, that we call photons. Photons have very well defined energies, and when they are absorbed by molecules their energy is incorporated to the molecule and the molecule becomes energetically excited. Given that molecules' energy states are also quantized, the amount of energy that can be absorbed from a photon is restricted to amounts that correspond to the energy difference between molecular states.

The main focus of these experiments, however, is not to use light to study the energy differences between molecular states (as done in traditional spectroscopy) but rather follow the processes through which the energy absorbed from the photon is redistributed

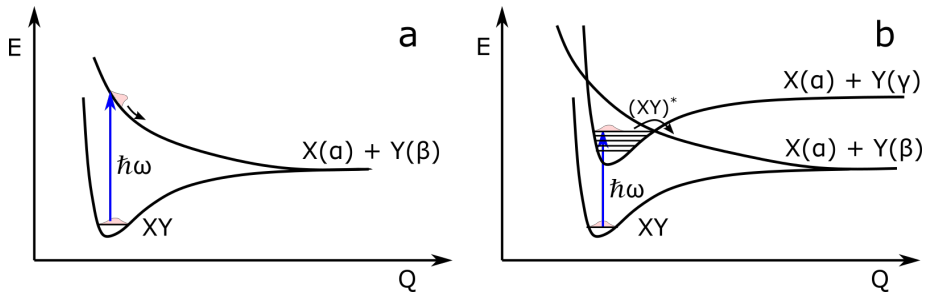


**Figure 4.1:** Schematic representation of two possible photodissociation mechanisms. (a) direct photodissociation by excitation to a dissociative state (b) predissociative photodissocyation through excitation to a bound state and subsequent nonadiabatic coupling to a dissociative state.

within the molecule.

More specifically, the process of interest in this chapter is the break-up of a molecule after it has been excited electronically, which is referred to as photodissociation. A general photodissociation reaction can be described as follows:

$$\mathrm{XY} + \mathrm{N}\hbar w \xrightarrow{(1)} (\mathrm{XY})^* \xrightarrow{(2)} \mathrm{X}(\alpha) + \mathrm{Y}(\beta) \tag{4.1}$$

here N is the number of photons absorbed by molecule XY, which is excited as depicted by the asterisk in $(\mathrm{XY})^*$ and subsequently breaks into fragments X and Y, which are found in the quantum states $\alpha$ and $\beta$, respectively. Studying the dynamics of this process implies asking questions such as - does the excited molecule, $(\mathrm{XY})^*$, photodissociate directly or does it change its electronic state before breaking into X and Y? What are the quantum states, $\alpha$ and $\beta$, of the products X and Y? Figure 4.1 shows two different photodissociation mechanisms - (a) direct photodissociation via a repulsive state and (b) excitation to a bound state, $(\mathrm{XY})^*$, followed by coupling to a repulsive state. Bound states such as the one shown in (b) can evolve into dissociative states through non-adiabatic coupling to a repulsive electronic state or by redistribution of the excitation energy into other modes along which the dissociation can take place. Following the temporal evolution of the molecule's electronic and vibrational states is one of the main goals in photochemistry, as detailed knowledge of the excited state dynamics are key in controlling the outcome of a photoinduced reaction.

### 4.1.1 A Model System: Photodissociation Dynamics of Molecular Iodine

Molecular iodine ($\mathrm{I}_2$) is one of the most extensively studied molecules within gas-phase photodissociation dynamics. A diagram depicting some of the electronic states of $\mathrm{I}_2$ can be found in fig.4.2. The ground state is labelled X and the subsequent (bound) excited electronic states are labelled A and B. The I-I bond can be broken in several ways, including excitation to a vibrational state with energy higher than $\mathrm{D}_0$, a process

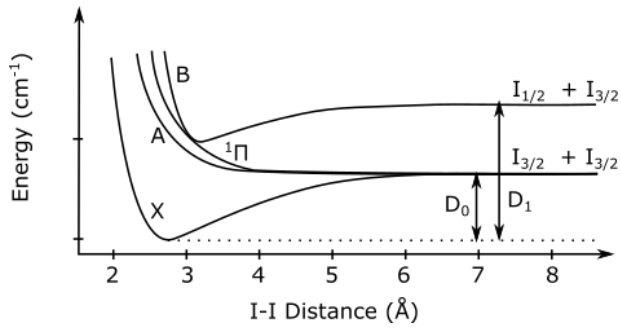


**Figure 4.2:** Selected potential energy curves for molecular iodine ($I_2$).

that occurs fully in the electronic ground state. Due to iodine being a homonuclear diatomic molecule, purely vibrational excitation cannot be achieved by photoexcitation, as selection rules dictate that photoinduced vibrational transitions can only occur if the transition is associated associated to a change in the dipole moment. However, dissociation of $I_2$ into two ground state iodine atoms ($^2P_{3/2}$) can be brought about by thermal excitation of the molecule.
Equally to thermally induced dissociation, photodissociation through the weakly bound A state yields two ground state iodine atoms, as it converges to the same products as the X state. In this case, the excess energy deposited into the molecule to populate the A state results in a higher kinetic energy of the iodine fragments.

Detecting $I^+$ ions produced after photodissociation at 600 nm by means of a 298.2 nm probe yields a series of channels that can be attributed to the aforementioned potential energy surfaces. The ion image obtained in this experiment is shown in fig.4.3a, together with the kinetic energy distribution of the fragments (fig.4.3b). The three distinct energy channels observed in the ion image shown in fig.4.3 will now be assigned.
Channel (1) stems from a perpendicular transition ($\Omega = 1$). The formation of $I^+$ channels takes place after dissociation from either the $I_2(I_u^1\Pi)$ or $I_2(A\ I_u(^3\Pi))$ state, prepared by one-photon excitation from the ground state, as summed up by:

$$(1) \qquad I_2(I_u^1\Pi)/I_2(A\,I_u(^3\Pi)) \longrightarrow I(^2P_{3/2}) + I(^2P_{3/2})$$

The ions corresponding to channels (2) and (3) are found to be emitted parallel to the pump pulse. In this case, however, both can be assigned to photofragments produced after two-photon excitation to the B $O_u^+(^3\Pi)$ and $I_2(I_u^1\Pi)$ states, respectively:

$$(2) \qquad I_2(B\,O_u^+(^3\Pi)) \longrightarrow I(^2P_{3/2}) + I(^2P_{1/2})$$
$$(3) \qquad I_2(I(^1_u\Pi)) \longrightarrow I(^2P_{3/2}) + I(^2P_{3/2})$$

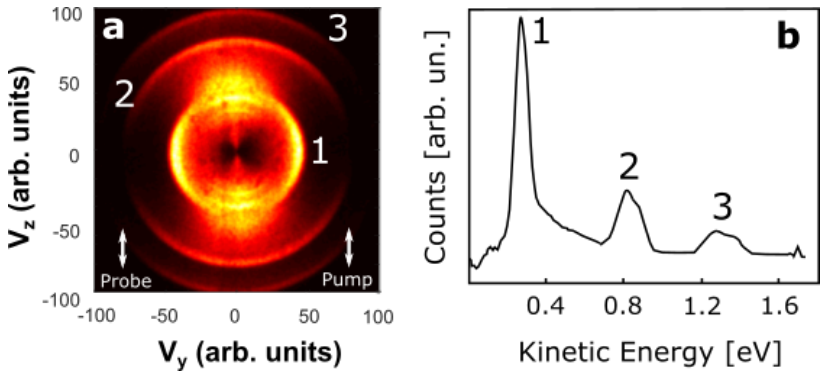


**Figure 4.3:** (a) Ion image of $I^+$ fragments stemming from molecular iodine excited at 600 nm and probed with 298.2 nm light 700 ps after excitation. The arrows in the image indicate the polarization of the pump and probe.(b) Kinetic energy distribution resulting from (2+1)-photon ionization of the iodine fragments.

these two-photon channels are enhanced by a resonance with the B state, which has a high probability of being excited at 600 nm [69].

The energy of each dissociation channel can be related to the kinetic energy of the fragments if the dissociation energy and the photon energy are known:

$$E_{kin} = \frac{1}{2}(nh\nu - D_i) \tag{4.2}$$

where $D_i$ is the dissociation corresponding to the photoproducts ($D_0$ = 12441 cm$^{-1}$ and $D_1$ = 20044 cm$^{-1}$) and $n$ the number of photons of energy h$\nu$ needed to populate the excited state. This equation is applicable to iodine because the photofragments are produced in well-defined quantum states and for iodine atoms in a given electronic state, all of the photon energy can be assumed to transform into kinetic energy. This leads to a much sharper kinetic energy distribution than in the photodissociation of polyatomic molecules, where the existence of vibrational and rotational states for the photofragments produces a broadening of the kinetic energy distribution.

The probing scheme used to obtain the image shown in fig.4.3 (298.2 nm) relies on [2+1]-REMPI ionization (more details in sec.3.6.6), which means that, for the image shown here, only iodine atoms in the electronic ground state ($^2P_{3/2}$) are ionized. The ionization scheme can also be tuned so that spin-orbit excited iodine atoms ($^2P_{1/2}$) are selectively detected, as it will be shown later in this chapter.

As mentioned earlier, two ground-state iodine atoms are produced in channels (1) and (3). Contribution from the Coulomb repulsion between the two $I^+$ fragments can be neglected because the probing is performed at a long time delay (700 ps), which ensures that the fragments are far and that a negligible amount of kinetic energy is supplied to the ions through Coulomb repulsion.

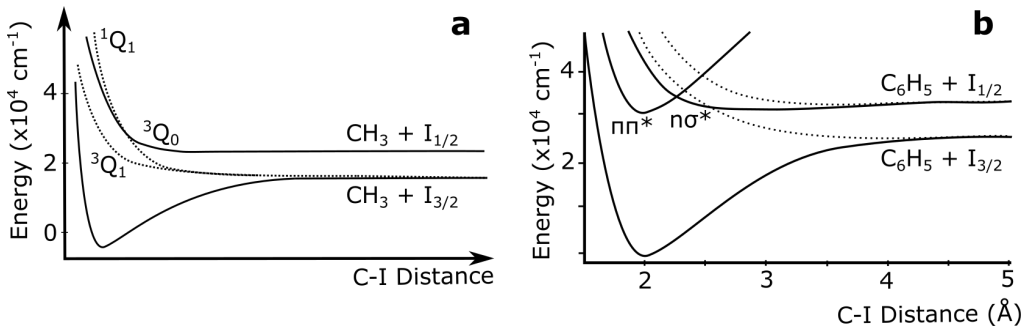


**Figure 4.4:** Selected potential energy curves of iodomethane (a) and iodobenzene (b).

### 4.1.2 Photodissociation Dynamics of Alkyl/Aryl Iodides

Methyl iodide was one of the first molecules used in photodissociation studies [70] and its photochemistry is well understood. This molecule, together with other alkyl halides, are good candidates for experiments because their photofragments have well-defined REMPI schemes that make it possible to access them selectively.

Methyl iodide undergoes dissociation when it is excited to a manifold of states ca. 6.7 eV above the ground state, known as the A-band [71]. Excitation to the A-band produces a methyl fragment and an iodine atom, which is found either in its spin-orbit ground state ($^2I_{3/2}$) or spin-orbit excited ($^2I_{1/2}$). Non-adiabatic coupling of the $^1Q_1$ and $^3Q_0$ surfaces produces a distribution of states for the iodine fragments, as it was also the case for the previous example concerning molecular iodine. The potential energy curves corresponding to the different electronic states that form the A-band are shown in fig.4.4a. From a molecular orbital point of view, excitation promotes an electron from a non-binding orbital to an antibonding orbital, labelled $\sigma^* \leftarrow$n. Excitation of an electron from a nonbonding orbital to an antibonding orbital can be regarded as the mechanistic explanation for the breakage of the C-I bond.

The photochemistry of methyl iodide is representative of that of other alkyl iodides but differs to that of aryl iodides, such as iodobenzene, in that there are additional states of $\pi$ symmetry that can be excited at 266 nm. The photochemistry of aryl iodides is characterized by excitation to dissociative n$\sigma^*$ states and to bound $\pi\pi^*$ states. Excitation of the bound $\pi\pi^*$ states can evolve towards dissociation by direct coupling to a repulsive n$\sigma^{/}$ surface of through vibrational energy redistribution [72].

As with iodomethane, photodissociation of iodobenzene at 266 nm yields iodine fragments in either $^2I_{3/2}$ or $^2I_{1/2}$, although with different quantum yields than iodomethane, due to the presence of the aforementioned $\pi\pi^*$ states (see fig.4.4b).

## 4.2 Photodissociation Experiments in Solution

The photodissociation dynamics discussed so far correspond to molecules in the gas phase, where the evolution of the fragments is fully determined by the intramolecular potentials. Photodissociation of molecules in solution changes significantly the dynamics of the process, as has been reported before [73, 74, 75]. A striking effect observed in solution is the geminate recombination of photofragments, that leads to reformation of the parent molecule in a vibrationally excited state. In conventional solvents, recombination occurs because collisions with the solvent decelerate the fragments to the point where their mutual attraction overcomes the kinetic energy that initially ejects them far from each other. This can occur provided that the solvent decelerates the photofragments quick enough and is reflected in the dependence of the photodissociation quantum yield and the viscosity of the solvent [76].

### 4.2.1 Photodissociation Reactions in HeNDs

Time-resolved experiments on photodissociation dynamics in helium nanodroplets are lacking. Liquid helium is an interesting matrix because its interaction with the dopant is gentle and hence the photodissociation process takes place relatively unhindered, which suggests that a higher photodissociation quantum yield can be expected as compared to other matrices. Furthermore, liquid helium provides a dissipative environment that is easier to model than molecular solvents due to its structural simplicity.

In a series of three papers, Andreas Braun and Marcel Drabbels [77, 78, 79] reported photodissociation experiments of alkyl and aryl iodides performed in helium nanodroplets. Their experiments focus on the energy dissipation of photofragments stemming from photodissociation of alkyl iodides and fluorinated alkyl iodides. The experimental approach followed by Braun and Drabbels is that of a pump-probe experiment with a fixed delay of 50 ns. The dissociation takes place after excitation to the A-band with a 266 nm pulse of 5 ns duration and is probed with a strong-field 800 nm probe pulse, and with a resonant probe pulse (333 nm) for the methyl fragments. The authors found that the kinetic energy of the alkyl fragments decreases with increasing droplet size and saturates at a droplet radius of 40 Å. The fragments were found to have a more anisotropic distribution for lower speeds and for lighter fragments.
The use of a resonant probe pulse (333 nm) gave access to methyl fragment in a quantum-state-selective manner, and revealed that only partial vibrational relaxation was achieved as a significant amount of methyl fragments in the first excited state of the umbrella mode were detected ($\nu_2 = 1$). Furthermore, the speeds and anistropy of the vibrationally excited fragments were found to match those of the fragments in the ground state, indicating that the interaction with the helium is not affected by the vibrational state of the escaping fragment.

In the third paper in the series, Braun and Drabbels elaborate on the observation of a "recombination signal", which can be thought of as the analog of the geminate recombination widely reported in other solvents [80, 81, 82].
This observation points out that despite the gentle nature of the helium nanodroplet, some fragments get cooled down enough to be dragged back into the center of the droplet and recombine, thus reforming the parent molecule.

## 4.3 Experimental Premise

As a part of our goal to study chemical reactions in helium nanodroplets, these series of experiments aim at measuring the effect of the nanodroplet in photodissociation experiments of two molecules that have been extensively characterised in the gas-phase (iodobenzene and iodine). The central question that motivated these experiments initially was - how long does it take for a fragment to leave the droplet?
Through this question, we were set to develop a better understanding of the fragment-droplet interaction and to observe any additional dynamics that could arise on top of those pertaining to the photodissociation process *per se*.

### 4.3.1 Experimental Scheme

A schematic diagram of the pump-probe scheme used in this experiment is shown in fig.4.5. The 266 nm pump excites the molecule to a dissociative state which produces two fragments that travel away from each other and towards the outside of the droplet. The focus is on detecting iodine atoms and measuring how long does it take for the iodine photofragments to exit the droplet. This is achieved by using a spectrally narrow probe pulse that brings iodine to an electronically excited state through a two-photon transition and ionizes with a third photon. When the atom is surrounded by helium atoms, the two-photon transition required to promote iodine to an excited state is blue-shifted and therefore the ionization probability sharply falls. Only when iodine escapes the droplet, therefore being in the gas-phase, can the probe pulse detect iodine atoms. With this in mind, it is expected that the signal should remain flat until the fastest iodine atoms escape the droplet, leading to a rise that plateaus as soon as all atoms have escaped the droplet.

### 4.3.2 Resonantly Enhanced Multiphoton Ionization

REMPI detection of photofragments has already been introduced in section 3.6.6. In this experiment the iodine atoms in the gas-phase are ionized selectively by exploiting this principle. Resonantly enhanced multiphoton ionization (REMPI) relies on molecular or atomic transitions to increase the probability of ionization and thus provides an effective ionization scheme even at low intensities. The scheme employed to ionize is represented

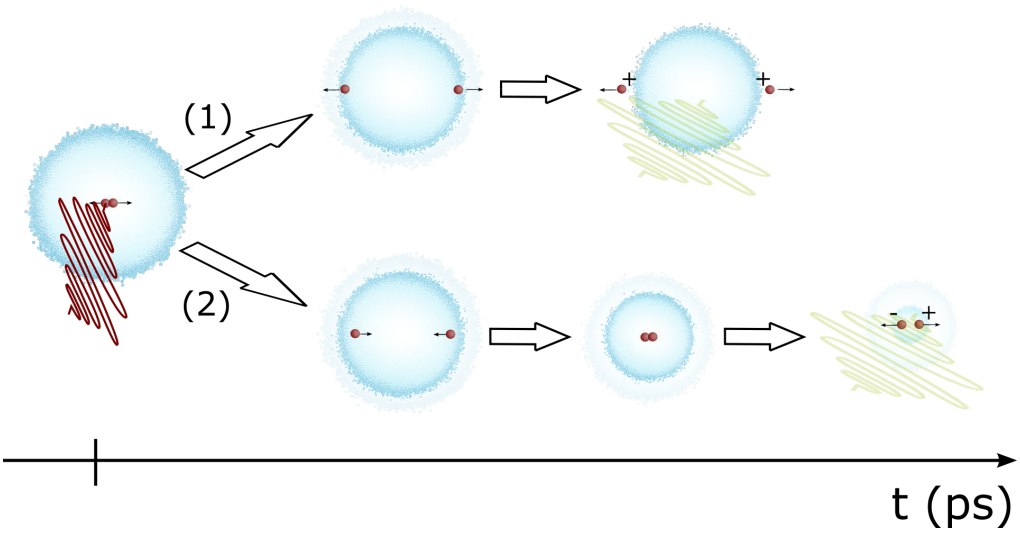


**Figure 4.5:** Schematic representation of the pump-probe experiment performed on iodine. The pump pulse is a 266 nm pulse of 1.2 ps duration. Dynamics are investigated by means of three different probe colours, 298 nm (≈4 ns), 800 nm (40 fs) and 400 nm (100 fs). The two possible outcomes of the photofragment are indicated as (1) escaping the droplet and (2) being trapped in the droplet and subsequent recombination. The shaded area of the droplets indicates the shrinking of the droplets by evaporation of helium atoms that carry away the energy dissipated by translational relaxation of the photofragments and later, by vibrational relaxation of the vibrationally-hot molecule.

as [m+n]-REMPI, where m is the number of photons used to excite the molecule/atom and n is the number of photons needed to ionize.
Previous work on the [2+1]-REMPI detection of iodine can be found in the literature [83, 84, 85]. The peaks extracted from the two-photon atomic spectrum of iodine from photodissociation of methyl iodide, as recorded by Eppink and Parker [86], are shown in table 4.1. The REMPI schemes for atomic iodine found in the literature generally tune the probe laser to the atomic line at 304.5 nm, which corresponds to iodine atoms in the spin-orbit ground state, due to the large oscillator strength of the transition.

## 4.4 Results

### 4.4.1 Two-photon Absorption Spectrum of Atomic Iodine

We first set ourselves to test the resonant probing scheme by aiming at recording a two-photon absorption spectrum of iodine produced by photodissociation of gas-phase iodobenzene molecules with 266 nm pump pulses. The 266 nm light is produced by frequency-tripling the 800 nm output from the amplifier. The resulting 266 nm pulses lead to excessive ionization due to their short duration, which lowers the efficiency of

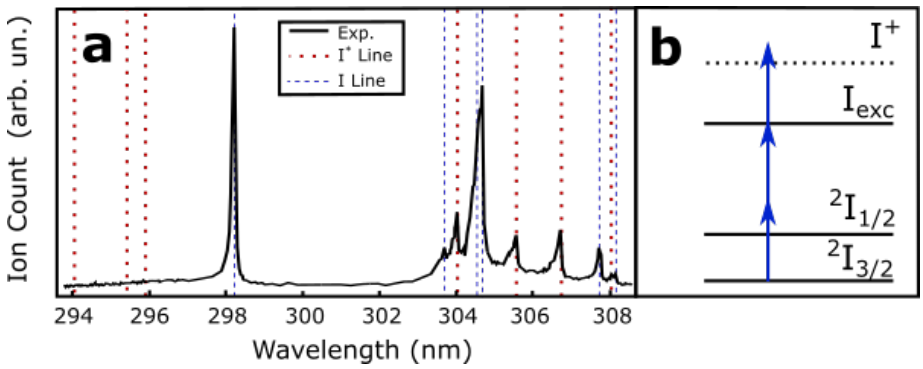


**Figure 4.6:** (a) Two-photon absorption spectrum of atomic iodine recorded after photodissociating iodobenzene by means of 266 nm light and scanning the wavelength of the probe by scanning the angle of the doubling crystal (KDP, 40 mm thickness). The lines are assigned to either ground state iodine atoms (I, blue dashed lines) or spin-orbit excited iodine atoms ($I^*$, red dotted lines). (b) schematic energy diagram of (2+1)-photon ionization of ground state iodine atoms.

the one-photon excitation. In order to minimize undesired multiphoton processes, the 266 nm pulses are stretched by means of a pair of prisms placed at 80 cm distance, with which an optimum pulse duration of 1.2 ps was found.

The probe pulse was produced by sending the amplifier output to an optical parametric amplifier, where 600 nm light is generated and subsequently frequency doubled through a 40 mm KDP crystal. The thick crystal produces spectrally narrow pulses of ca. 5 ps duration, whose wavelength can be adjusted by controlling the angle of incidence on the crystal through a motorized stage controller. The tunability is limited by the geometry of the crystal - if the angle diverges too much, the beam does not fully go through the crystal. The resulting wavelength range accessible from this optical scheme spans from 306.9 to 297.4 nm. Pumping iodobenzene with 266 nm light and probing with this range of wavelengths yields a two-photon absorption spectrum of gas-phase atomic iodine, as shown in fig.4.6. The values of the atomic lines and a comparison to values from the literature [87, 86] are included in table 4.1. Assignment of the lines reveals the presence of spin-orbit excited iodine atoms, which is consistent with the photochemistry of iodobenzene excited at 266 nm. The peaks corresponding to spin-orbit excited iodine atoms are marked with a blue dashed line, while those corresponding to ground state iodine atoms are marked with a dotted red line. The strongest line in the two-photon spectrum in fig.4.6 is found at 298.2 nm (8.32 eV), which corresponds to ionization following the atomic transition $I(^3P_2)6p(^2[1]_{3/2}) \longleftarrow I(5p^2P_{3/2})$.

### 4.4.2 Gas-Phase Photodissociation Dynamics

The time evolution of iodine ions after photodissociation at 266 nm was followed by both means of (2+1)-photon ionization with a resonant (298.2 nm) probe pulse and by

| State | Intermediate State | $E_{ref}$ (eV) | $E_{meas}$ (eV) |
|---|---|---|---|
| $I(5p^2P_{3/2})$ | $(^3P_2)6p(^2[1]_{3/2})$ | 8.314 | 8.320 |
| $I(5p^2P_{3/2})$ | $(^3P_2)6p(^2[1]_{1/2})$ | 8.166 | 8.170 |
| $I^*(5p^2P_{1/2})$ | $(^3P_1)6p(^2[1]_{1/2})$ | 8.158 | 8.162 |
| $I(5p^2P_{3/2})$ | $(^3P_2)6p(^2[3]_{7/2})$ | 8.144 | 8.146 |
| $I(5p^2P_{3/2})$ | $(^3P_2)6p(^2[3]_{5/2})$ | 8.140 | 8.144 |
| $I^*(5p^2P_{1/2})$ | $(^3P_1)6p(^2[1]_{3/2})$ | 8.120 | 8.120 |
| $I^*(5p^2P_{1/2})$ | $(^3P_1)6p(^2[2]_{3/2})$ | 8.086 | 8.090 |

**Table 4.1:** Absorption lines of atomic iodine as extracted from the two-photon spectrum recorded in this experiment and their comparison to values from the literature [87, 86]

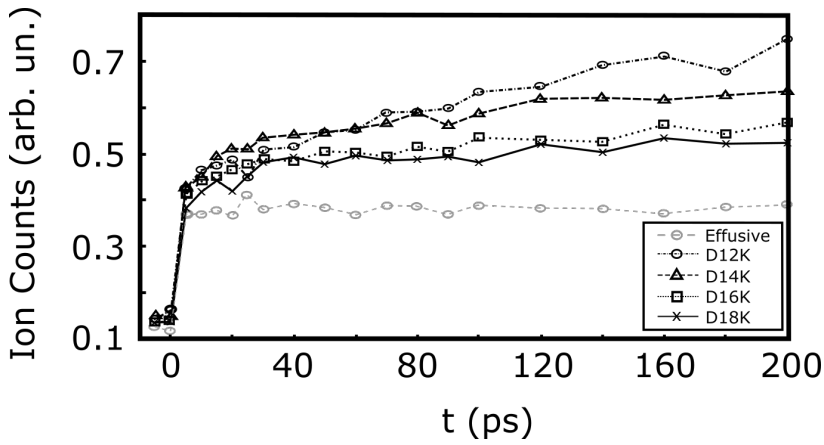


**Figure 4.7:** Time evolution of $I^+$ ions after 266 nm photodissociation of helium-embedded iodobenzene molecules and (2+1)-photon resonant ionization probing. Each data set corresponds to droplets formed at a given nozzle temperature, see text for details.

nonresonant (strong-field) ionization with an 800 nm probe pulse.

The ion yield evolution after photodissociation of IB molecules at 266 nm and probed with 298.2 nm light is shown in figure 4.7 (grey circles, 'effusive'). The C-I bond in iodobenzene breaks within a few hundred femtoseconds [88], which is much faster than the pump-probe cross-correlation, and thus the dynamics of bond breaking cannot be measured in this experiment. The rise in ion yield at time zero is hence determined by the pump-probe cross-correlation width of around 5 ps, as observed in the initial rise of the ion yield. This provides the baseline for further studies on helium nanodroplets; any deviation from the fast bond breakage can be related to dynamics arising from the interaction of the fragments with the helium environment.

### 4.4.3 Photodissociation Dynamics in HeNDs

The resonant probing scheme just introduced for gas-phase iodobenzene molecules is now applied to helium-embedded molecules. If the photofragments were to follow a simple escape mechanism where they travel directly out of the droplet, no ions are expected to hit the detector (with the exception of those produced from effusive molecules) until the iodine atoms have escaped the droplet, given that the probe is chosen to be selective towards unsolvated iodine atoms. Once all of the iodine atoms have escaped the droplets (with the slowest corresponding to the largest droplet), the ion count is expected to plateau as there should be no other source of photofragments. Fig.4.7 shows the time evolution of the iodine ion yield during the first 200 ps after excitation at 266 nm. Contrary to what was expected, the signal does not show a delayed rise and a subsequent plateau, but rather keeps increasing for hundreds of picoseconds.
The rise in ion yield is found to be droplet size dependent, with larger droplets showing a steeper rise. As a reference, the signal stemming from effusive molecules (i.e. gas-phase molecules) is also included in the figure. The effusive signal shows dynamics identical to those of gas-phase molecules, as it is to be expected, and additionally serves the purpose of ruling out possible artefacts that arise from a misalignment of the lasers as the delay stage is moved.
The signal rise takes place on a timescale much larger than what is to be expected for a direct escape mechanism. In order to find when the signal plateaus for the large droplets (13K), a measurement was carried out to 3.5 ns after excitation. The signal keeps increasing, strongly indicating a contribution from ions produced through a different mechanism than ionization of atoms directly escaping the droplets after photodissociation. Following this observation, our experimental efforts were directed towards elucidating the mechanism through which iodine atoms were found to become unsolvated in the nanosecond timescale.
Initially, it was hypothesised that due to the sensitivity towards iodine atoms in the electronic ground state, spin-orbit relaxation of iodine atoms produced in the $^2P_{1/2}$ state could account for the slow dynamics. This assumption was made based on previous evidence found in the literature, in which the ejection of rubidium atoms from the helium nanodroplet was reported to be caused by spin-orbit relaxation [89].

In order to find out whether spin-orbit relaxation has a contribution on the observed dynamics, we set ourselves to investigate the dynamics of spin-orbit excited iodine atoms. To achieve this, the wavelength of the probe pulse is tuned to (2+1)-photon resonantly ionize spin-orbit excited iodine atoms, relying on the available two-photon excitation of iodine at 306.7 nm (see table 4.1). The time evolution of spin-orbit excited iodine atoms is shown in fig.4.8, and the ion images corresponding to the two different resonant probes used are shown in fig.4.9. The dynamics observed show the same trend as iodine atoms in their ground state, which rules out that it is the gradual decay of $I^*$ atoms that produces additional I atoms which upon state-selective ionization results in the gradual

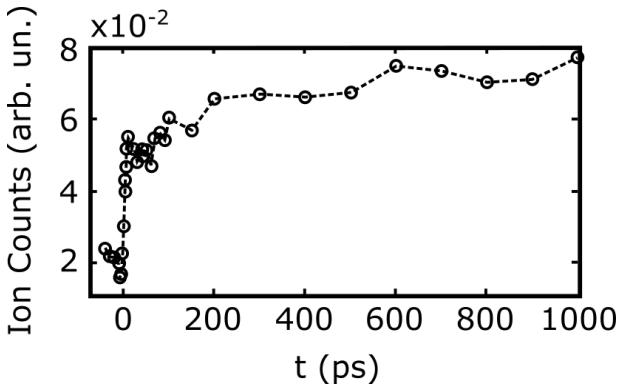


**Figure 4.8:** Time evolution of the ion yield for spin-orbit excited iodine atoms after photodissociation of helium-embedded iodobenzene at 266 nm. The probe was tuned to 306.7 nm, which corresponds to an $I^*$ resonance (see table 4.1). The helium nanodroplet beam was formed at a temperature of 13K and stagnation pressure of 40 bar.

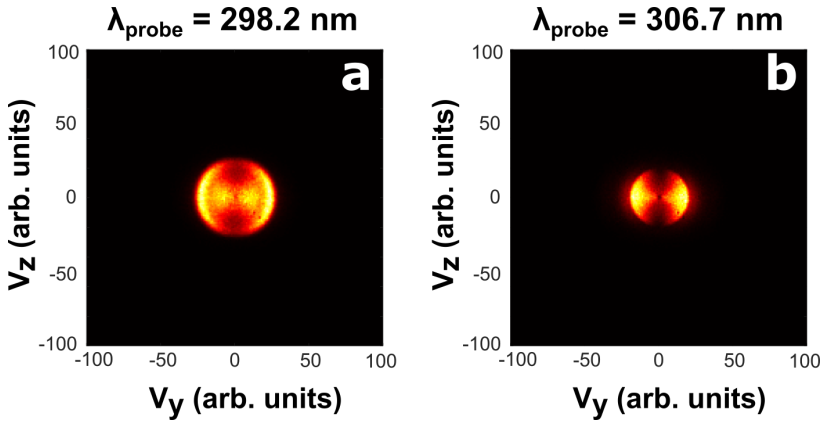


**Figure 4.9:** $I^+$ ion images obtained 700 ps after 266 nm photodissociation of iodobenzene and probed with (a) 298.2 nm, which corresponds to ground state iodine atoms and (b) 306.7 nm, which corresponds to spin-orbit excited iodine atoms.

rise of the $I^+$ signals observed in fig.4.8.

Resonant probing has proven to be an effective way to measure the formation of gas-phase iodine atoms, but it fails at providing insight into the dynamics of the phenyl fragments or the parent ion dynamics, as well as those iodine atoms that are solvated by helium. Experiments with an 800 nm nonresonant probe were carried out to investigate the dynamics of the phenyl fragments and the parent ions, aiming at obtaining a more complete picture of the processes that lead to the production of gas-phase iodine atoms at long timescales.

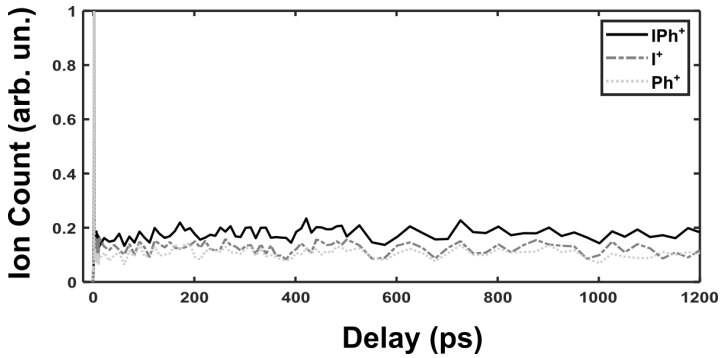


**Figure 4.10:** Time evolution of the iodobenzene ($IPh^+$), iodine ($I^+$) and phenyl ($Ph^+$) ion yield. Gas-phase iodobenzene molecules were dissociated by means of 266 nm light and probed with 800 nm pulses.

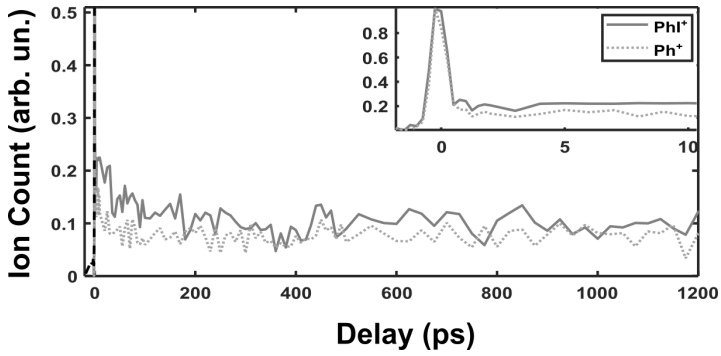


**Figure 4.11:** Time evolution of the iodobenzene ($IPh^+$) and phenyl ($Ph^+$) ion yield. Helium-embedded (13K, 50bar) iodobenzene molecules were dissociated by means of 266 nm light and probed with 800 nm pulses.

A first step in extending the experiment towards strong-field probing of helium-embedded molecules is to investigate the gas-phase dynamics with the 800 nm strong-field probe. Contrary to the resonant probe, strong-field ionization is not sensitive towards a single solvation state or quantum state of the fragments. Instead, the ion yield is related to the ionization potential of the species, with the probability of a fragment being ionized decreasing as the ionization potential increases. The ionization potentials of relevant fragments and molecules are listed in table 4.2.

The resulting time evolution of the ion yield is presented in fig.4.10. As mentioned earlier, excitation of iodobenzene (IPh) at 266 nm leads through direct dissociation via $n\sigma$ states or predissociation through excitation to a bound state ($\pi\pi^*$) that can couple directly or through vibrational energy redistribution to dissociative potential energy surfaces. The duration of the pump pulse (266 nm) limits the time resolution of the experiment, and the two channels are indistinguishable, as dissociation through both channels occurs on a sub-picosecond timescale [75].

| Fragment | IP (eV) |
|---|---|
| Iodine | 10.45 |
| Phenyl | 8.32 |
| Iodobenzene | 8.72 |
| $I_2$ | 9.3 |

**Table 4.2:** Ionization energies of molecules and molecular fragments produced in the experiment (source: NIST).

The production of phenyl (Ph) and iodine (I) fragments is seen as an increase their respective ion yield at positive timescales. As for $IPh^+$, the increase in ion counts at positive time delays can be understood by a lowering of the ionization potential as some molecules remain in an excited bound state.

After the gas-phase experiments, we set ourselves to study the dynamics of the $Ph^+$ and $PhI^+$ fragments stemming from 266 nm photodissociation of helium-embedded iodobenzene and probed with 800 nm, as shown in fig.4.11. It was not possible to record a clear iodine signal, most likely due to a mixture of two factors - the high ionization potential of atomic iodine and the low signals recorded in helium-embedded species.
The $IPh^+$ ion count decays to around 20% of its peak value, as observed in gas-phase molecules, but differs from the former case in that the signal keeps decaying until 10% of its value at time zero within 200 ps. This decay can be understood as a relaxation of the molecules in an excited bound state mediated by the helium environment, which results in a progressive increase of the ionization potential as vibrational relaxation takes place. As for the phenyl fragments, the signal decays to around 20% of the peak value as in the gas-phase experiment, but instead of remaining constant decays to 10% of the peak value within 100 ps. This implies that there is a mechanism by which phenyl fragments are transformed into other species or become harder to ionize. Alternatively, it is possible that the production of some phenyl fragment stems from breakage of excited parent molecule. As the production of $Ph^+$ would be linked to the population of excited parent molecules, the decay of IPh would lead to a decrease of $Ph^+$ fragments as the molecule relaxes.

The dynamics of the system are further investigated by changing the probe colour to 400 nm, as shown in fig.4.12. Significantly different dynamics are observed, especially for the parent ion signal ($IPh^+$). After time zero the signal is found to decrease to around 60% of the peak value, followed by an increase in yield for the parent ion ($IPh^+$) and a change in slope for the phenyl fragment. The iodine fragment reaches 20% of the peak value within 20 ps, while it takes 100 ps for the phenyl fragment to reach the same relative value.

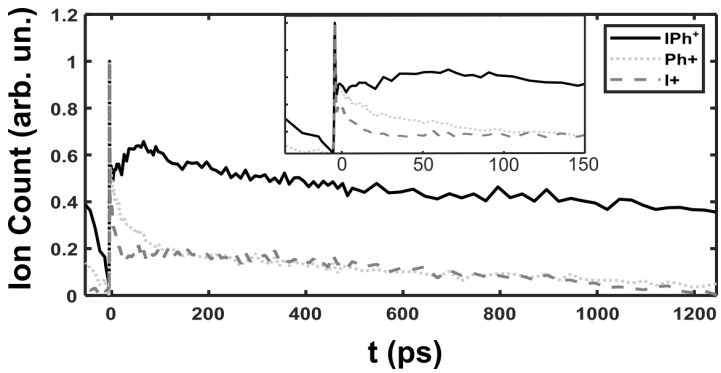


**Figure 4.12:** Time evolution of the iodobenzene ($IPh^+$), phenyl ($Ph^+$) and iodine ($I^+$) ion yield. Helium-embedded (13K, 50bar) iodobenzene molecules were dissociated by means of 266 nm light and probed with 400 nm pulses.

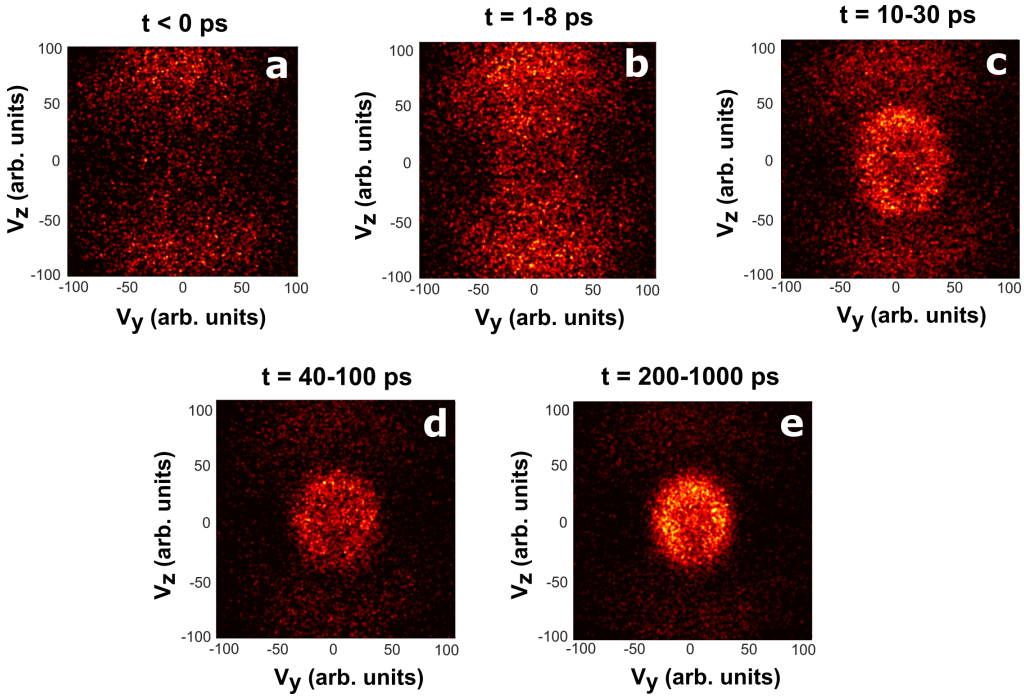


**Figure 4.13:** (a-e) $I^+$ ion images of helium-embedded $I_2$ (nozzle conditions: 14K and 40 bar) recorded for a range of pump-probe time delays after 510 nm photodissociation of iodine ($I_2$) molecules and probed with 800 nm pulses (40 fs).

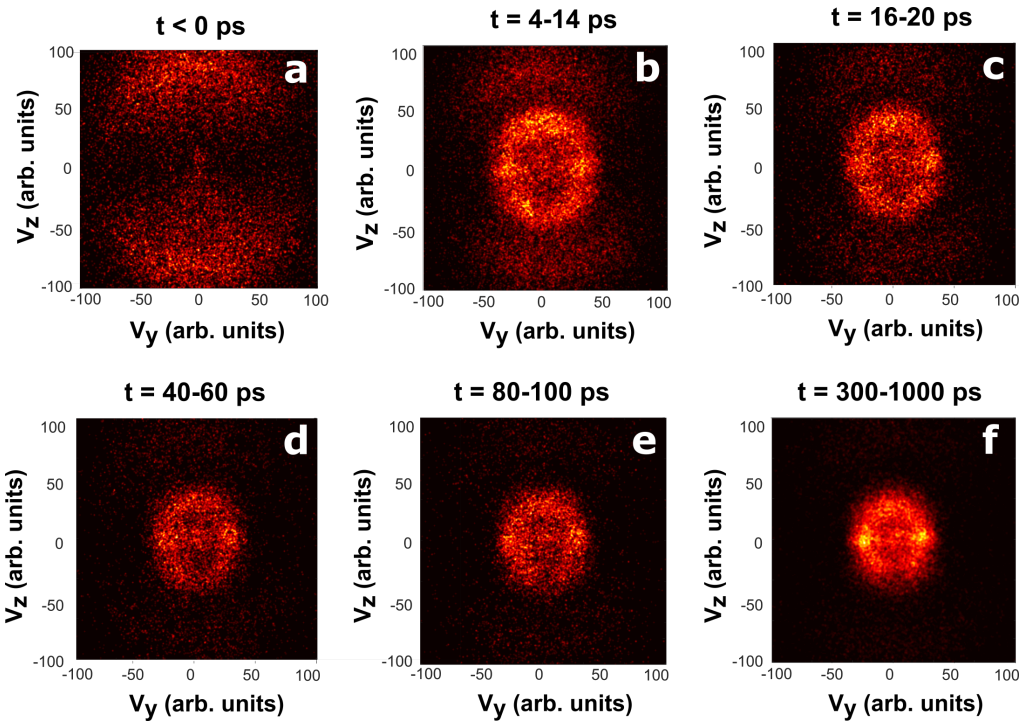


**Figure 4.14:** (a-e) $I^+$ ion images of helium-embedded $I_2$ (nozzle conditions: 18K and 40 bar) recorded for a range of pump-probe time delays after 510 nm photodissociation of iodine ($I_2$) molecules and probed with 800 nm pulses (40 fs).

### 4.4.4 Ion Images: $I_2$

The data recorded for iodobenzene has been complemented by measuring the photodissociation dynamics of another iodine-containing species, iodine ($I_2$). It must be noted that the data presented now does not suffice to perform a quantitative analysis of the energy distribution of the ions. Nonetheless, some trends are apparent and the images shown as follows are considered useful to back the hypothesis presented in this chapter.

$I^+$ ion images obtained after photodissociating helium-embedded iodine ($I_2$) by excitation at 510 nm are shown in fig.4.13 for droplets formed at 14K and 40 bar, and in fig.4.14 for droplets formed at 18K and 40 bar. The limited statistics for these images requires that images for a broad range of time delays are stacked. The result is a clear change in the ion distribution characterized by a relative increase of ions with low velocities as time increases. An intriguing feature observed most clearly for molecules embedded in droplets containing an average of 4,500 atoms (nozzle conditions: 18K, 40 bar), as shown in fig.4.14. Panel (f), which corresponds to the image taken at the longest time delays (300-1000 ps) shows a highly confined ion channel, not observed for gas-phase iodine molecules (see fig. 4.3).

## 4.5 Discussion

Resonant probing of iodine fragments revealed a sustained increase of the ion signal at longer times than it would be expected for a direct escape mechanism. By direct escape mechanism, it is meant that the fragments follow a quasi-straight path out of the droplet, and thereby a lower and upper limit can be set for the timescale of this process, based on the initial speed of the fragments and the size of the droplets. Considering that iodine fragments are produced with a speed of approximately 850 m/s from the dissociation process and an upper limit of 60 Å for the droplet radius, the escape time is expected to be under 10 ps (precisely 7 ps for the values considered), in line with the values reported by Braun and Drabbels [77].

Our results pose the question of where do the slow dynamics observed in our experiments stem from; they occur on the nanosecond timescale for the largest droplet studied in the experiments, which was detected by means of a resonant probe. In this regard, the strong-field data recorded with a 400 nm probe adds evidence that the slow dynamics can be related to the geminate recombination of iodine and phenyl fragments, a mechanism that was also proposed by Braun and Drabbels as they observed a zero energy channel in their ion images. The increase in ion yield for $IPh^+$ up to around 80 ps points towards a recombination mechanism, but the dynamics of the system are complicated and must be accounted for by considering also the dynamics observed for all photofragments.

The discussion will be started by going two steps back and analyzing the gas-phase data obtained for the 800 nm and 400 nm strong-field probes. The gas-phase dynamics of iodobenzene, shown in fig.4.10 reveal a decay of the parent ion signal on a timescale below the time resolution of the experiment. This has been reported in previous studies [90, 91], where two time constants of 400 and 600 fs were assigned to the photodissociation event. The most prominent feature is that the $IPh^+$ signal is higher at positive time delays. This increase in signal can be assigned to excited molecules that remain in the $\pi\pi^*$ state. Due to the higher energy of the excited state, the energy needed to ionize the molecule is lower and hence a higher ion signal is recorded. From this point, it is convenient to move on to the helium-solvated molecules. As in the gas-phase case, the signal drops to 20% of the peak value, but the dynamics following the initial decay are different. Instead of staying constant as in the gas-phase, the ion yield decreases until it reaches around 10% of the peak value at around 1.2 ns. Acting as a dissipative environment, the helium solvent offers a series of acceptor states to which excited iodobenzene molecules can transfer energy, and thus solvent-induced relaxation can account for the decrease in ion yield for helium-embedded molecules, as the transfer of energy from IPh to the solvent lowers the energy of the molecule and thus the ionization rate from the probe pulse.
Concerning the fragment signals, a first observation is that the decrease of the $Ph^+$ ion yield is likely to be linked to the relaxation of IPh, suggesting that dissociation of excited IPh molecules is a source of $Ph^+$ ions.

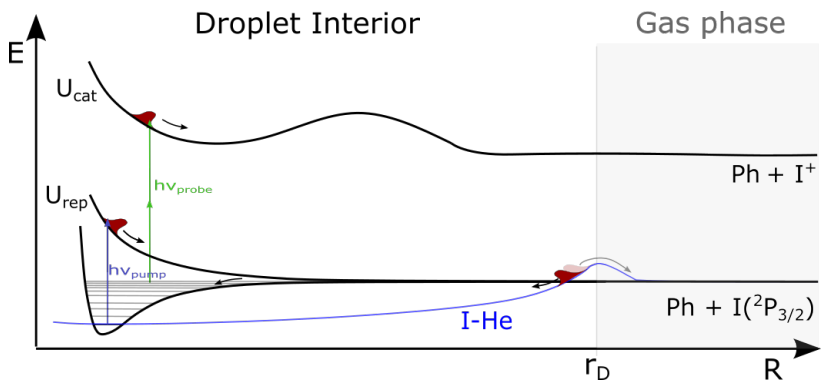


**Figure 4.15:** Schematic representation of the potential energy curves involved in the mechanistic explanation proposed for the dynamics observed for the photodissociation of iodobenzene (IPh) molecules embedded in helium nanodroplets of radius $r_D$. $U_{rep}$ refers to the repulsive state that leads to direct dissociation into a neutral iodine fragment and a neutral phenyl fragment, while $U_{cat}$ refers to the state that produces an iodine in a cationic state.

The experiment using a 400 nm probe complements the information just discussed, as it reveals that the parent ion yield peaks at ca. 80 ps, contrary to the signal recorded at 800 nm where no rise was observed. With these observations in hand, the mechanism schematized in fig 4.15 is proposed. Excitation at 266 nm photodissociates iodobenzene, producing phenyl and iodine fragments that travel towards the outside of the droplet. The translationally excited fragments dissipate energy by interacting with the solvent, until eventually some fragments are slowed down enough to be dragged towards the bound state at the center of the droplet. Due to their motion towards the center, the two fragments meet and recombine, forming a vibrationally hot molecule. Once the recombination takes place, a claim that can be further supported by the experiments by Drabbels and Braun, it must be argued how the interaction of the vibrationally hot molecule and the probe pulse yields phenyl and iodine ions. It seems plausible that the simultaneous dissociation-ionization of the excited parent molecule requires the involvement of dissociative ionic states, given that only the probe pulse is left to interact with the molecule. To support this, it is pointed out that the decay of the phenyl and iodine signal follows different time constants, which indicates that they are produced through different potential energy surfaces. As shown in fig.4.4, the ca. 2 eV (16000 $cm^{-1}$) of vibrational energy initially deposited in the molecule after recombination enables the probe photons to access states that were previously too high in energy. The nature of this states is speculative, but excitation to a Rydberg states that couples to ion pair states, or direct excitation to ion pair states are reasonable possibilities [92, 93]. As a final remark, it must be underlined that the mechanistic interpretation of the result is speculative, and that more experiments should be carried out in the future to identify the electronic states that participate in the production of the fragments.

*"Most human beings have an almost infinite capacity for taking things for granted."*

— Aldous Huxley, *Brave New World*

# 5 The Primary Steps of Solvation

The experiments concerning the solvation dynamics of sodium cations were performed together with Constant Schouder and Simon H. Albrechtsen. The experiments on lithium and potassium were performed together with Simon H. Albrechtsen. The time-dependent density functional (TDDFT) simulations were done entirely by our collaborators at the physics department of Universitat de Barcelona, prof. Manuel Barranco and prof. Martí Pi.

## 5.1 Motivation

When learning chemical reactions in undergraduate chemistry courses, it is introduced that the conditions at which a reaction is carried out (temperature, pressure, catalyst) are indicated on top of the reaction arrow that starts from the main reactant and points towards the main product. The solvent is sometimes also included among this information, especially if it exchanges atoms with the reactants during the reaction; for instance, when the solvent acts as a base. However, the solvent is often omitted and in the best of cases, the choice of solvent is based on its polarity - polar solvents are best suited for reactions involving an increase in polarity (reaction to products) and apolar solvents in the opposite case. In practice, most organic chemists choose their solvent based on an intuition developed by obtaining more experience working in the laboratory.
An "educated choice" of solvent that does not involve experiments is generally not an option. The action of the solvent during the reaction is hard to measure or simulate because even simple reactions involve a large number of surrounding solvent molecules, often in frantic motion, each having many degrees of freedom; such conditions make simulations impossible in practice. Experiments are not free of difficulties themselves.

Following structural and energetic changes in the solvent is possible but challenging. The observables stem from an average of an ensemble of solute and solvent molecules, complicating a detailed study of specific solvent interactions.
Having said this, solvent interactions may seem an obscure art into which chemists venture with more faith than science on their bags. Nonetheless, physical chemistry does understand to a large degree solvent interactions, and an account of experiments and theoretical models that treat solvation will be provided later in this chapter.
The less dramatic message is rather that solvation dynamics remains an unexplored part of chemistry if compared to other areas, which is striking considering that it drives or is involved directly in virtually any process (excluding gas-phase chemistry) and hence a better understanding of it could improve our control over chemical and biological processes. This is especially relevant in the field of photochemistry, where light provides the chemist with a powerful tool to influence reactions as they occur. The main motivation of the experiments shown in this chapter is to develop a simplified solvent/solute system that can be measured at the single-particle level and which can be compared directly with simulations. The solvent of choice is liquid helium, and the solutes are alkali metal atoms. Results concerning the solvation of alkali metal cations in liquid helium will be shown and compared to TDDFT simulations.

## 5.2 Chemical Reactions in Solution

Gas-phase chemical reactions are interesting from a fundamental perspective: the reactive system is stripped of environmental perturbations, thus simplifying the interpretation of the experimental data. Gas-phase chemistry is also relevant in some fields, such as atmospheric chemistry. Nonetheless, most chemistry occurs in solution and therefore a large portion of research in physical chemistry is devoted to developing experimental methods to study chemical dynamics in the presence of a solvent. This is a challenging enterprise due to the large degree of complexity added by the solvent, as well as the challenges involved in decoupling excitation/detection of the solute and the solvent.
The solvent can be viewed as an energy reservoir in the context of a reaction. It can provide the energy necessary to surmount the energy barrier of a reaction through collisions, but it also provides a high density of acceptor states that can remove excess energy from the solute. Examples of the former are found among electron transfer (ET) reactions (fig.5.1a). Solvent fluctuations facilitate to a large extent the transition from reagents to products and in the case of ET reactions, a given solvent geometry ($q_{bl}$ in fig.5.1a) influences the reaction. The big effect of the solvent geometry on ET reactions is due to the nature of the process, where charge is being transferred. The transfer of charge generally means that the solvent molecules have very different equilibrium configurations for the reagents and products.

Other than ET reactions, reactions can often be depicted using potential energy curves rather than potential energy surfaces. This is the case in reactions involving only one

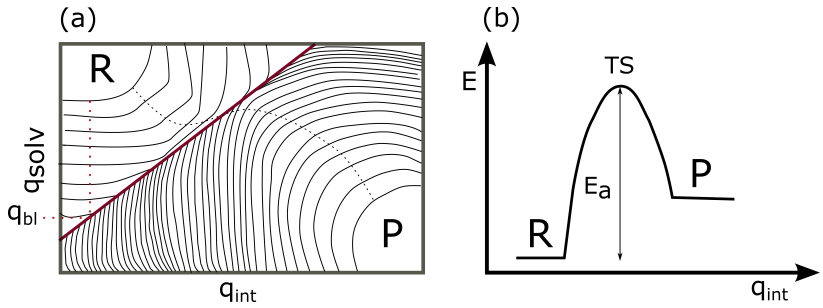


**Figure 5.1:** Contour map of a hypothetical electron transfer reaction. The reaction coordinate in the y-axis is the solvent coordinate, and the x-axis corresponds to an internal mode of the molecule. $q_{bl}$ marks the solvent geometry at which the reaction becomes barrierless.

internal coordinate, but also for processes involving multiple coordinates, which can often by represented by combining the different modes into a reaction coordinate. For reactions that fall in this category, the solvent is not considered explicitly in the reaction coordinate, but still plays an important role. The energy necessary to reach the transition state (depicted as TS in fig.5.1b) is provided by collisions with the solvent. Additionally, in bimolecular reactions the reactants need to meet in order for the reaction to proceed, and as such the nature of the interaction of the solvent with the solute has an effect over the reaction rate [94] - a solvent that binds too strongly with the solute can hinder the exchange necessary to form a prereactive complex.

### 5.2.1 Intermolecular Interactions

In simple terms, what characterises reactions in solution is the constant presence of solvent molecules around the solute. The solvent-solute interactions are binding but there are some nuances as compared to the binding interactions found in chemical bonds, such as covalent bonding. Covalent bonding is characterized by being short-range interactions and also directional, due to the involvement of electronic orbitals. As learnt from the "ball-and-stick" models described in chemistry books, it is tempting to interpret bonds as rigid objects connecting the atoms, like a stick or a metal bar that holds the atoms together. Despite being an oversimplification, this picture captures well the highly directional nature of covalent bonding.

Solvent interactions are more complex; they are less directional (thermal energy is often much larger than the energy difference between different solvent configurations) and especially, solvation is a collective process. The energy gained by a single solute-solvent interaction is generally low and does not account for the fact that substances dissolve. In order to explain solvation, the collective interactions must be taken into consideration, as well as the entropic contribution in going from a highly ordered system to a more disordered one.

Understanding solvation requires to understand how molecules with bound states in which no electrons are shared interact i.e., interactions in which the molecules remain defined as separate entities but exert an attraction or repulsion over each other.
Intermolecular interactions are generally considered "long-range": they span ranges larger than the typical distances in between atoms in a molecule. The dependence of a particular interaction with the distance between the particles depends on whether the particles are polar, apolar or have a charge, as well as their size and total charge.

#### 5.2.1.1 Point charge-Point charge interaction

The simplest case can be considered that in which the two particles can be approximated as point charges. The interaction potential between two point charges is described by the Coulomb potential, which depends inversely on the distance between the two particles:

$$\omega(r) = \frac{q_1 q_2}{4\pi\epsilon\epsilon_0 r} \tag{5.1}$$

where $q_1$ and $q_2$ are the charges of the particles, $r$ the distance between them and $\epsilon_0$ is the vacuum permitivity and $\epsilon$ the permittivity of the medium. The simplicity of the Coulomb potential is one of the reasons why the Coulomb Explosion Imaging (CEI) technique has been widely used as an imaging technique and will be introduced later as it is the main method in this chapter.

#### 5.2.1.2 Point charge-Point dipole interaction

If one of the particles possesses a dipole, the distance-dependence changes as the square of the distance, as well as including a cosine term that describes the orientation of the dipole:

$$\omega(r) = -\frac{q\mu\cos\theta}{4\pi\epsilon\epsilon_0 r^2} \tag{5.2}$$

where $\mu$ is the magnitude of the dipole, $q$ the charge of the particle and $\theta$ is the angle between the dipole moment and the distance, $r$:

$$\cos\theta = \frac{\vec{\mu}\cdot\vec{r}}{|\mu||r|} \tag{5.3}$$

The maximum interaction occurs when $\theta = 0^o$. Equation 5.2 applies when the dipole is fixed, if the dipole can rotate freely the interaction is averaged over all possible orientations and yields:

$$\omega(r) = -\frac{q^2\mu^2}{6(4\pi\epsilon_0\epsilon)^2 kTr^4} \tag{5.4}$$

which corresponds to the high-temperature approximation, that is appropriate provided that:

$$kT > \frac{Qu}{4\pi\epsilon_0\epsilon r^2} \tag{5.5}$$

Eq.5.4 features an inverse dependence on temperature, which can be understood as a lowered potential at higher temperatures, caused by the excitation of the rotational modes as the temperature increases. At low temperatures the expression is reduced to eq.5.2 [95], which physically is equivalent to the point charge fixing the dipole position in space (that is to say, it induces alignment of the dipole).

#### 5.2.1.3 Interactions involving uncharged particles

Particles with a charge generally present stronger interactions than uncharged particles, but interactions between uncharged particles are a widespread phenomenon and occur both across the condensed and the gas phase. When it comes to uncharged particles, a quantity of central importance is the polarizability, $\alpha$. The polarizability relates to how easy it is for an external electric field to induce a dipole in a particle. The dipole induced by an external electric field, $E$, follows:

$$u_{ind} = \alpha E \tag{5.6}$$

where $u_{ind}$ is the magnitude of the induced dipole and $\alpha$ the aforementioned polarizability. The general expression for the interaction between a point charge and an induced dipole can be described by:

$$\omega(r) = -\frac{q^2\alpha}{2(4\pi\epsilon\epsilon_0)^2 r^4} \tag{5.7}$$

Finally, if both particles lack a charge, the interaction is driven by their respective polarizabilities, which assuming two identical particles follows:

$$\omega(r) = -\frac{3}{4}\frac{I\alpha^2}{(4\pi\epsilon\epsilon_0)^2 r^6} \tag{5.8}$$

where $I$ corresponds to the ionization potential. This equation is often referred to as London's equation[96], and interactions within this category are referred to as dispersion interactions or Van der Waals interactions.

### 5.2.2 Coulomb Explosion Imaging

Coulomb explosion imaging (CEI) has been used as the principal method in experiments involving structural characterisation in this thesis. Contrary to traditional spectroscopic methods like IR spectroscopy, where the determination of structure requires comparison of the experimental data to quantum models, CEI accesses the molecular structure in a more direct manner by applying Coulomb's law to the kinetic energy of ionic fragments. The first step in CEI is to multiply ionize a molecule i.e., stripping off multiple electrons. This often leads to break-up of the molecular cation into recoiling ionic fragments due to their internal electrostatic repulsion [97, 98]. Assuming that the ionization process takes place infinitely fast, the recoil directions of the cationic fragments should provide

information about the structure of the neutral molecule. This assumption forms the basis of why CEI can be used as a tool in molecular structure determination and will be addressed later in this section.
Following the prompt multiple ionization of the molecule, the close proximity of positively charged fragments originates a repulsive potential between the fragments. As time propagates, the potential energy is decreased as the distance between the fragments increases. The potential energy lost by the fragments as they travel apart translates into kinetic energy. Given enough time, all the potential energy will be converted into kinetic energy i.e., the fragments reach their maximum and final velocity. Measuring the final velocity of the charged fragments can thus be related to the initial potential energy and by extension to the distance between the fragments in the neutral molecule, as shown in eq.5.1

One of the requisites for the Coulomb approximation to be valid is that the fragments are far enough from each other. If two particles are too close, intermolecular forces can play a significant role and lead to a modification of the Coulombic curve. The approximation can further break down if the two particles are found at distances where orbital overlap occurs [99].

### 5.2.3 Solvent Dynamics

Long-range interactions differentiate liquids from gases. Stronger long-range interactions allow a liquid to remain more ordered due to a higher degree of interaction, on average, among its constituents. This makes liquids dynamical systems, with a fast change in the state of individual molecules that still keep a degree of cohesion on average. Once a solute is introduced in the liquid, structural changes arise. As an example, if the solute is an ion and the solvent is made up of polar molecules, the solvent-solute interaction will be stronger than the solvent-solvent interaction, and thus solvent molecules will arrange preferentially around the ion. In the limit where the solute interacts much more strongly with the solvent than the solvent interacts with itself, a number of solvent molecules are found to "crystallize" around the ion i.e., their positions become fixed around the ion forming a quasi-molecule (fig.5.2). How many molecules bind depends on the size of the ion and the strength of the interaction. This number is the solvation number (hydration number if the solvent is water) and it is of interest in many fields of chemistry and biology, mostly those where diffusion of molecules is involved (e.g. the diffusion of $Na^+/K^+$ across membranes, electrode reactions).

As an example it is illustrative to look at how alkali metal ions interact with water, given that this is a case of interest in biological systems. Sodium and lithium have a hydration number of 4-5 [95], while cesium of only 1 [95]; the larger ions have a lower charge density, and this leads to a lower hydration number. Small and multivalent ions have generally higher hydration numbers, such as $Cr^{3+}$ or $Mg^{2+}$, for which 6 molecules are found to solvate the ion [95].
The number of water molecules attached to, e.g. sodium, is a subject of debate in the

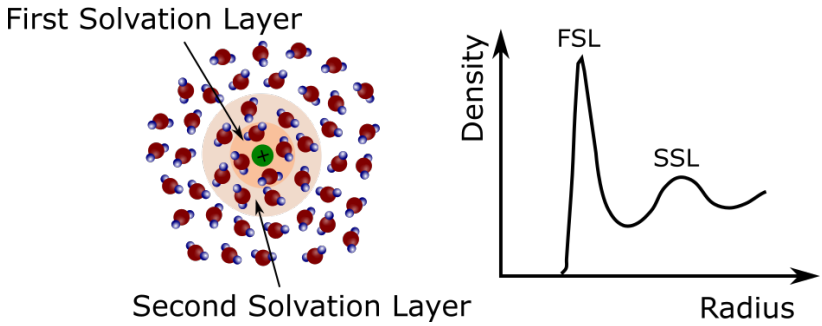


**Figure 5.2:** Illustration of the first (FSL) and second (SSL) solvation layers around a cation. The radial density and degree of order of the molecules is higher closer to the ion, and decays to nearly the bulk value after the second layer.

literature, as reality shows that the picture is more complex than simply a bunch of molecules fast bound to the ion. The reason for this is that in most cases a static picture fails to describe what happens around the molecule. In the case of sodium, non-integer number are found in the literature, such as 5.2 [95]. Non-integer number strike as nonphysical, given that we are counting water molecules, but this is due to time-averaging. Solvent molecules are in constant motion and molecules constituting the, e.g. first solvation layer, undergo a frantic exchange with surrounding molecules that is dependent on the strength of the bond. For the smallest alkali metal ions ($Li^+$, $Na^+$, $K^+$) the exchange rate of a water molecule is found to be in the order of nanoseconds, but for a larger ion such as $Cs^+$ it goes down to hundreds of picoseconds. For more strongly binding ions, such as $Cr^{3+}$, the lifetime of the species can be as long as hours, and thus opens the discussion of whether the solvent "reacts" with the ion, rather than solvate it. Solvation numbers and binding energies are important static properties, but it is the dynamical response of the solvent that is of most importance in chemical dynamics. Gas-phase reactions are known to be particularly fast, on the order of femtoseconds. This is because once the transition state geometry is formed, the complex can easily evolve into products. However, the presence of a solvent changes this. This difference is not only due to the different potential energy surface found in the gas phase as compared to solution, but also by the coupling between the reactant and the solvent dynamics. A good understanding of the real-time solvent dynamics is necessary to describe with detail chemical reactions in solution.

### 5.2.4 Femtosecond Solvation Dynamics

For a system in equilibrium, the arrangement of solvent molecules around a solute is determined by the charge distribution in the solute molecule. Hence that if a chemical reaction, such as electron transfer, or excitation to a different electronic state takes place the equilibrium shifts towards a different solvent configuration; in other words, exciting the solute by accepting/donating an electron or absorbing/emitting a photon triggers

a dynamical response of the system. Solvent relaxation takes place on the picosecond timescale, as it involves nuclear motion. However, experiments on solvation dynamics reveal that the solvent response is actually bimodal, with a fast component on the femtosecond regime and a slow(er) component on the order of picoseconds [94].

The sudden change in the solvent-solute pair potential has a strong effect on the system due to the close proximity of the two elements and the large magnitude of the interaction potential. This produces a fast reaction of the system, dominated by the solute-solvent interaction (inertial motion), followed by a slower dynamical response driven by the solvent-solvent pair interactions [100].

Studying fast processes as these requires the use of time-resolved spectroscopy techniques, with resolution well beyond that of the response time of electronic components. This is overcome by inducing a chemical reaction or molecular excitation with a short pulse of light, and using a second pulse to interrogate the previously excited molecules, in what is called a "pump-probe experiment". This experimental scheme, already introduced in chapter 4, is key in studying molecular dynamics, as it allows experimental scientists to access processes beyond the capabilities of conventional spectroscopy. Most pump-probe techniques are differentiated by the nature of the probe pulse and the signal that is detected. A popular technique to measure solvent dynamics is femtosecond fluorescence up-conversion [101]: molecules are initially excited by a pump pulse, which populates an excited electronic state. The dynamics of the excited state are followed by measuring the fluorescence emission by mixing the fluorescence with a probe pulse in a non-linear crystal, which yields a sum-frequency signal that is used as an observable.
Up-conversion techniques rely on following the energy evolution of the excited state through its emission spectrum: the energy of the excited state lowers as a consequence of solvent relaxation, which is observed as a red-shift in the fluorescence emission. Following this, the rate at which the fluorescence emission decays can be related to the solvation dynamics, provided that this can be considered the main mechanism lowering the energy of the excited state. A limitation of this technique is that the measured signal is an average of a large number of molecules, and additionally, that it lacks selectivity towards the immediate solvation environment of the molecule.
Experimental measurement of the dynamical response of the solvent at the atomic level is challenging, and our knowledge is still mainly based on theoretical simulations. In a recent paper by Biasin et al. [102], the solvent dynamics accompanying photoinduced intramolecular electron transfer in an iron-ruthenium bimetallic complex solvated in water were studied at the natural timescale. The authors reported a method based on pumping the molecules in solution with a femtosecond laser pulse and probing with a femtosecond X-ray pulse made available by a free electron laser. These results succeeded at measuring dynamics of electron transfer coupled with solvent motion, but they relied on a structural model developed by performing molecular dynamics simulations.

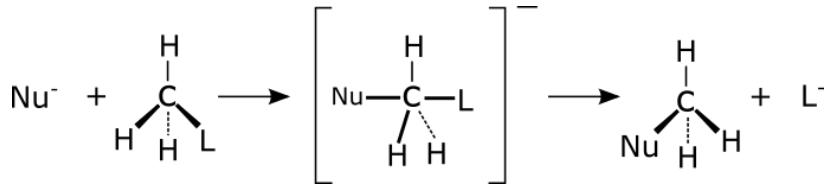


**Figure 5.3:** Exemplification of an $S_N2$ reaction.

### 5.2.5 The Role of Solvation in Chemical Reactions

One of the favourite reactions of many organic chemists and especially physical organic chemists is the $S_N2$ reaction, or "nucleophilic substitution". In this reaction, an electron-rich reactant (such as a halide anion) approaches an electron-poor region of a molecule (such as the carbon in a haloalkane) and progressively binds to it, while at the same time stretching the bond between the electron-deficient atom and another substituent (see fig.5.3). The reaction results in the substitution of one of its atoms/fragments for the incoming electron-rich fragment/atom. The dynamics of the reaction can in some cases be followed by considering just one of the normal modes of the molecule, for instance, by following evolution of the potential energy along the C-X bond distance. This yields a potential energy curve analogous to that shown in fig.5.1b. In the particular case of a pure $S_N2$ reaction, the transition state corresponds to a molecule including both fragments and having bipyramidal geometry.
Due to the fact that charge distribution is at the core of $S_N2$ reactions, the difference in charge of the reactants, products, and transition state, are generally highly important to develop an understanding of the reaction. A general rule when choosing what solvent suits the reaction best is, that its polarity should be chosen according to which of the species wants to be stabilised. As charge is more delocalized in the transition state as compared to either reagents or products, $S_N2$ reactions show higher yields in apolar solvents than in polar solvents. A large effect on the outcome of the reaction is thence caused by the charge distribution, which can be considered a static property, but the solvent dynamics around the transition state also have a far from negligible effect on the reaction [103]. In the gas phase the potential energy surface drives the reaction as it is the only source of forces applied on the molecule, but in solution the collision of solvent molecules can provide the reactants with a push in the direction opposite to product formation, which can lead to a decrease in the number of molecules that cross the potential energy barrier [104].

A different case, already introduced earlier in this chapter, is electron transfer reactions. It stems from the nature of the reaction itself, that there will be a change in the charge distribution in the products as compared to the reactants. A consequence of this is that the transfer of the electron, which can be considered to be nearly instantaneous on the timescales considered here, needs to be followed by a stabilization of the product by solvent rearrangement. If the solvent relaxation is too slow, the electron can "jump" back

into its original location and reform the reactants. The frequency of the solvent modes is determining the electron transfer rate, and the frequency of the solvent fluctuations can be considered the most important parameter in most ET reactions.
A last example in which the solvent plays an important role, is in photodissociation reactions. When light induces the breaking of a bond in the gas phase the fragments are ejected and experience no force beyond that exerted by the geminate fragment itself. In solution this is different, because the fragment collides with the solvent as it travels far from its origin. If the solvent "traps" the outgoing fragments for long enough, the binding potential between the two leads to a recombination which restores the reactant in a vibrationally excited state. This is known as the cage-effect, and is analogous to what has been reported in chapter 4. This phenomenon is well-known within photochemistry, and it is the reason why photodissociation reactions have lower quantum yields in solution than in the gas phase [74, 75].

## 5.3 Solvation Dynamics of Alkali Metals in HeNDs

The main result in this chapter is the observation of the solvation dynamics of alkali metal cations with femtosecond time resolution at the single-particle level. To our understanding, there is a lack of experiments that probe directly the time evolution of the solvation of an ion with single-particle resolution. Additionally, our method does not rely on the use of complex modelling to interpret the data.
Besides the measurement of the solvation dynamics of alkali metal cations, the method developed here can be applied as a measurement of the distance between the surface and the bulk dopants by means of Coulomb-explosion imaging. This method can be used to measure the size of the droplet, if certain assumptions are made, and it serves as an indication of the position of the neutral dopants inside of the droplet.

### 5.3.1 Experimental Premise

The underlying concept in the experiment presented here is to induce a sudden change in the interaction potential between an alkali metal atom adsorbed to the surface of a helium nanodroplet, which drives a dynamical response of the system. The fact that the atom is found on the surface brings the system as close to a gas-phase atom as we deem possible. The change in potential is achieved by ionizing the alkali metal, which produces a change in interaction potential from the initial $Na@He_N$ to $Na^+@He_N$. The neutral atom binds very weakly to the helium due to its loose valence electron, which lowers the binding energy due to Pauli repulsion. Removing the valence electron to form the alkali metal cation changes the interaction potential from heliophobic to heliophilic (fig.5.4).
More specifically, ionization at $t_{pump}$ changes the potential depth from a weak interaction of 1.76 K (1.22 $cm^{-1}$) for the neutral atom (Na) to a potential depth of 400 K (278 $cm^{-1}$) for the ion [26]. The energetic cost that liquid helium pays to solvate the newly formed cation is much lower than the He-He interaction (5 $cm^{-1}$), making the solvation process energetically favourable.

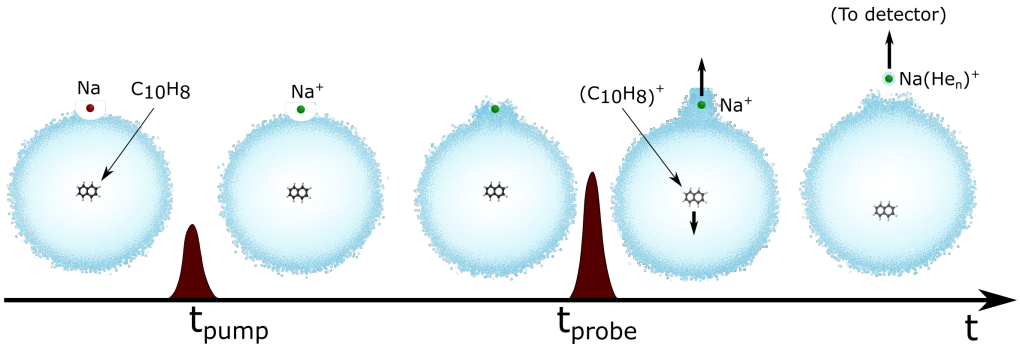


**Figure 5.4:** Schematic representation of the time evolution of the system. After the ionization of the alkali atom on the surface by the pump pulse, the helium droplet is brought out of equilibrium and surrounds the alkali cation in order to minimize its energy. Ionizing the molecule inside the droplet (e.g. naphthalene, $C_10H_10$) with the probe pulse produces a Coulomb repulsion between the alkali cation and the molecular cation, which ejects the metal cation from the droplet. The solvation state of the metal cation can be followed through mass spectrometric analysis.

### 5.3.2 Experimental Setup

The main results presented here were taken by initiating solvation of the alkali ion with an 800 nm pump pulse ($\omega_o = 40$ $\mu$m, $\tau_{pulse} = 40$ fs, $I_{pump} = 0.2$ TW/cm$^2$) and a 400 nm probe pulse ($\omega_o = 25$ $\mu$m, $\tau_{pulse} = 130$ fs, $I_{probe} \approx 0.09$-$0.35$ TW/cm$^2$). In the experiments with lithium, the probe pulse was an 800 nm pulse with similar characteristics to the pump pulse, except for its intensity. The intensity of the pump was adjusted so that the ionization of the bulk-dopant was negligible. As for the probe pulse, the intensity is chosen sufficiently high so that the bulk molecule is ionized, but not too high in order to minimize fragmentation.

The experiment lies on the premise that the pump power ionizes surface-bound sodium atoms and not the bulk dopant. Given that the pump pulse is nonresonant for the species doped in the droplet, the parameter that dominates the ionization probability is the ionization potential. Hence, a "clean" ionization of sodium (or lithium) in hetero-doped droplets relies on the lower ionization potential of the alkali metals, of 5.14 eV and 5.39 eV for sodium and lithium respectively, versus 8.14 of naphthalene. The ionization potentials for the species used in our experiments are shown in table 5.1. A last aspect of the experiment to be considered is the effect of the probe pulse on the $Na^+$ ion. Following the same argumentation just presented for the interaction with the pump pulse; a comparison of the ionization potential of naphthalene (8.14 eV) with the second ionization energy of sodium (47.29 eV) indicates that removing a second electron from sodium is very unlikely, and that ionizing exclusively naphthalene is the most likely outcome of the interaction of the probe pulse with the hetero-doped droplets.

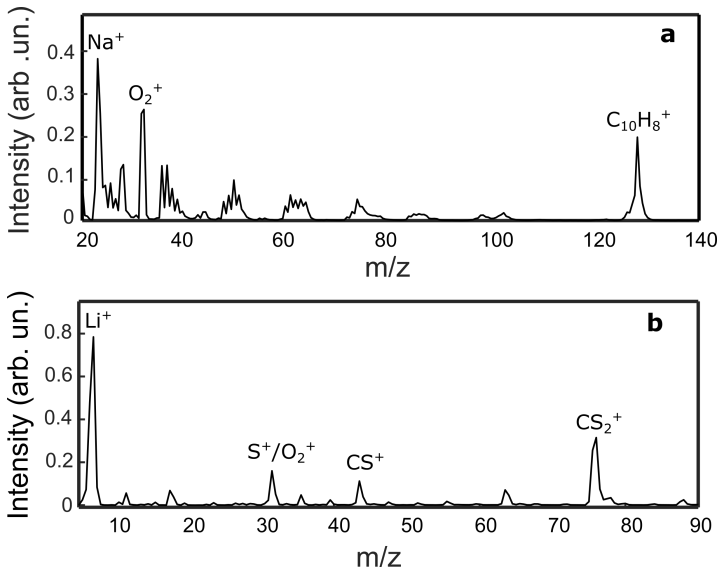


**Figure 5.5:** Mass spectrum of helium nanodroplets co-doped with (a) sodium/naphthalene and (b) lithium/$CS_2$.

**Table 5.1:** Ionization Energies (source: NIST)

| Species | IP1 [eV] | IP2 [eV] |
|---|---|---|
| Sodium | 5.14 | 47.29 |
| Lithium | 5.39 | 75.64 |
| Naphthalene | 8.14 | - |
| Benzonitrile | 9.71 | - |
| $CS_2$ | 10.08 | - |

### 5.3.3 Doping Considerations

A first step in this experiment is to confirm that the desired complex is formed. The system of interest is made up of an alkali atom (Ak) on the surface of the helium nanodroplet and an organic molecule (M) located in the center, as shown in fig.5.4. This can be done by means of mass spectrometric (MS) analysis. The mass spectrum of sodium/naphthalene doped droplets is shown in fig.5.5a, where the sodium (m/z = 23) and naphthalene (m/z = 128) peaks are seen to be the most prominent. Naphthalene fragments can also be observed, together with a prominent oxygen peak at m/z = 32, which stems from ionizing $O_2$ molecules present in the target chamber. It would be desirable to keep the parent ion intact by lowering the probe intensity, but this results in a lowering of the signal; a compromise between signal and fragmentation was sought.
The mass spectrum for lithium/$CS_2$ co-doped droplets is shown in fig.5.5b. In this case the peaks of lithium (m/z = 7) and $CS_2$ (m/z = 76) are dominant, with minor contributions from $S^+$ and $CS^+$ produced through dissociative ionization of the parent molecule.

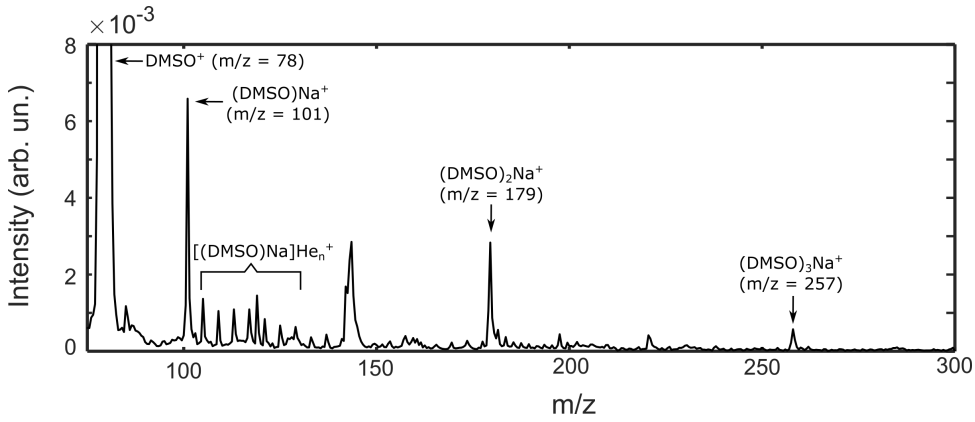


**Figure 5.6:** Mass spectrum of helium nanodroplets codoped with Na/DMSO. The probe used here was defocused in order to minimize the number of complexes that are destroyed in the probing process. See text for details.

Given that the ionization of sodium/lithium triggers an evolution of the system where the alkali ion evolves towards the interior of the droplet (or at least gets surrounded by helium atoms), it could be expected that the interaction between the bulk dopant and the alkali ion would lead to the formation of $(Ak\text{-}M)^+$ complexes. Taking the naphthalene-sodium complex as an example $(Np\text{-}Na)^+$, a binding energy of 1.24 eV has been reported[105] for the gas-phase complex. Despite the large binding energy, detection of these complexes requires the use of low laser intensities that ensure the complex remains intact after interaction with the laser pulse. The mass spectrum shown in fig.5.6 corresponds to molecules co-doped with dimethyl sulfoxide and sodium but it will be used as reference, since for the purpose of the experiment discussed here the behaviour of this atom/molecule pair is representative of all the systems studied.
The mass spectrum reveals four main peaks, corresponding to complexes $DMSO_n\text{-}Na^+$ with n= 1-3. The peak at m/z = 142 has not been labelled in the figure because it was assigned to an impurity ($CH_3I$), which remained in the target chamber after the last experiment run.

At this point it must be mentioned that the $(Ak\text{-}M)^+$ complexes were observed for all of the pairs of dopants measured except those where naphthalene was used as a co-dopant. Even though this will not be covered in detail, initially it was hypothesized that the observation of the complex could be due to the electrostatic properties of the bulk dopant. In particular, it was hypothesized that the dipole moment of the molecule could be what determined the formation of the complex due to the longer range of charge-dipole interactions. After running experiments with a series of molecules of increasing dipole moment this was discarded. It was possible to observe the formation of $(Ak\text{-}M)^+$ complexes with M being benzene and cyclohexane, ruling out the dipole contribution as the main factor determining whether the complex is formed or not. At this point, what drives the complex formation is still not understood and it is a subject

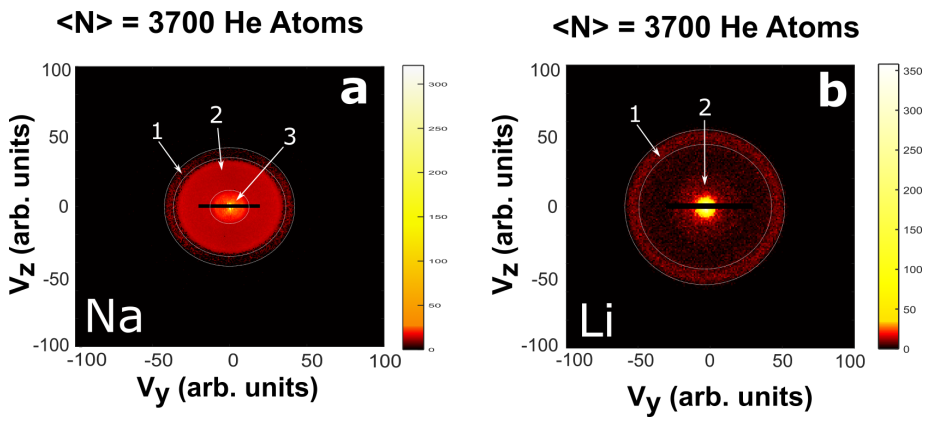


**Figure 5.7:** Helium-embedded (a) Sodium and (b) lithium ion images. Droplets formed at a stagnation pressure of 50 bar and nozzle temperature of 20K.

of study in the group.

### 5.3.4 Ion Images

The TimePix3 camera provides ion images of each fragment recorded in the mass spectrum. The ion images contain information about the kinetic energy of the ion, which makes it possible to differentiate ions according to the pathway through which they are formed.

Alkali ion images are of special interest, as the Coulomb explosion of the surface and bulk dopant ($Ak^+$-$M^+$) should yield a distinct ring that can be unequivocally assigned to hetero-doped droplets.

As a start, ion images of droplets (exclusively) doped with sodium or lithium are shown in fig.5.7a and fig.5.7b, respectively. The ion channels observed stem from helium nanodroplets doped with one or two alkali metal atoms. The alkali cations produced in singly-doped droplets have zero kinetic energy, as they do not experience repulsion from any other fragments. Thus, all the ions that hit the detector with some kinetic energy must be assigned to dimers or higher order oligomers. The black horizontal line seen in the center of the image is a filter applied to remove the contribution from gas-phase atoms that effuse into the target chamber; this signal does not contain information about the experiment, given that it originates from sodium atoms that are not doped into droplets. Fortunately, the effusive signal is easily assigned due to its characteristics - the effusive signal does not show a radial symmetry and instead is constituted by a narrow line that features only positive velocities. This can be understood by considering that the only kinetic energy available to effusive atoms originates from the thermal energy obtained in the sublimation process.

The three ionic channels observed in the sodium ion image (fig.5.7a) can be assigned to:

$$(1)\,Na_2\,(X^1\Sigma_g{}^+) \longrightarrow Na^+ + Na^+ \;;\; \text{TKER} = 4.28 \text{ eV}$$
$$(2)\,Na_2\,(a^3\Sigma_u{}^+) \longrightarrow Na^+ + Na^+ \;;\; \text{TKER} = 2.79 \text{ eV}$$
$$(3)\,Na_2 \longrightarrow Na + Na^+$$

where channel (1) and (2) correspond to Coulomb explosion of sodium dimers in the singlet and triplet state, respectively. Channel (3) is assigned to single ionization of the sodium dimer, which leads to dissociation into a sodium cation and a neutral sodium atom.
The same rationale can be applied to lithium. In this case, the energy channels observed for lithium are:

$$(1)\,Li_2\,(a^3\Sigma_u{}^+) \longrightarrow Li^+ + Li^+ \;;\; \text{TKER} = 3.38 \text{ eV}$$
$$(2)\,Li_2 \longrightarrow Li + Li^+$$

where channel (1) corresponds to Coulomb explosion of the lithium dimer in its triplet state, and channel (2) can be assigned to a dissociative ionization channel.

The situation is drastically different when the droplets are now doped both with an alkali atom plus an organic molecule. Fig.5.8 shows the Na+ ion image recorded for 5 different droplet size distributions. An extra ring has now appeared and its radius seems to increase as the helium droplet gets smaller.

Abel inversion of the ion images, shown in fig.5.9, provides a clearer view of the different channels from which the ions are formed. Using fig.5.9a as a starting point, the different ion channels are labelled from 1-4. The four channels can be divided in two groups, those arising from hetero-doped droplets and those stemming from homo-doped droplets (sodium dimers, assigned in fig.5.7a). Channels 1 and 2 are assigned to dissociative evens stemming from sodium dimers, as they can be also observed in absence of co-dopant. Covariance analysis of the two channels reveals an angular correlation of $180^o$ between ion hits in that energy range, which confirms that ions within those energy ranges arise from sodium dimers. The two rings can be assigned to the dimer in its triplet state (2) and in its singlet state (1). Previous experimental data on this two channels and their independence from droplet size or laser frequency make them suitable to calibrate the images, as the energies of these channels have been assigned in a previous experiment within our groun [21]. The inner-most feature (4) is likely to be a dissociative channel stemming from ionizing one sodium atom in the dimer, leading to subsequent break up into a sodium ion and a neutral sodium atom for which, given that only one sodium ion is produced in this channel, no covariance is observed.

A key observation in these images is that channel (3) only appears once a co-dopant is introduced in the droplet. This strongly indicates that these channels stems from hetero-doped droplets. The ions are formed in the process:

$$Na{-}DMSO(He_N) \longrightarrow Na^+ + DMSO^+(He_N)$$

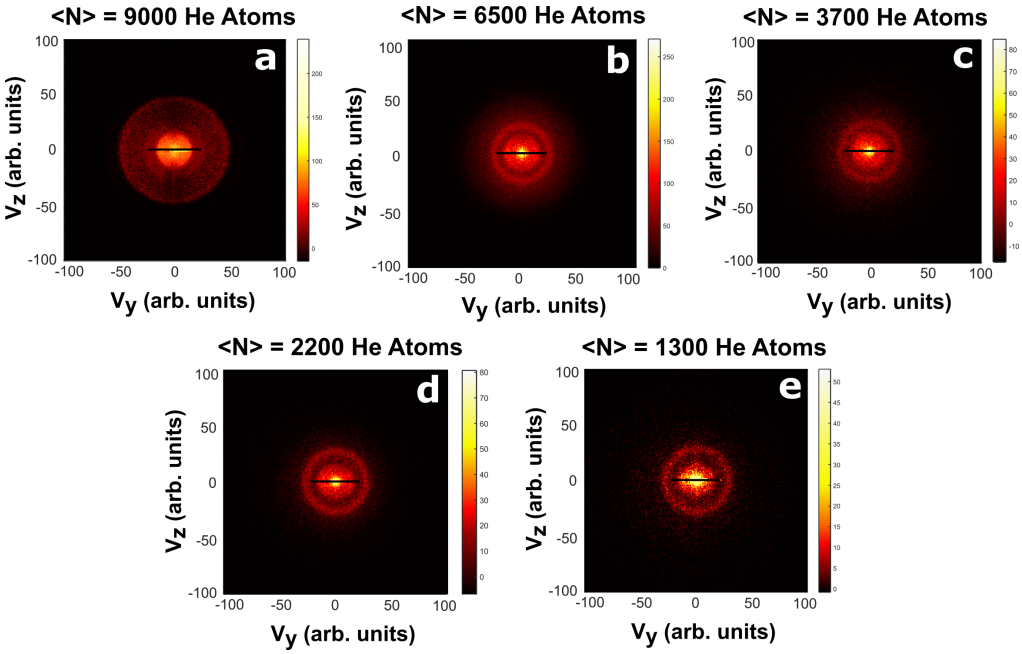


**Figure 5.8:** $Na^+$ ion images for five different droplet size distributions of mean size <N>. The codopant used to obtain the ion images was DMSO in all cases. For an assignment of the $Na^+$ channels the reader is referred to fig.5.9

.

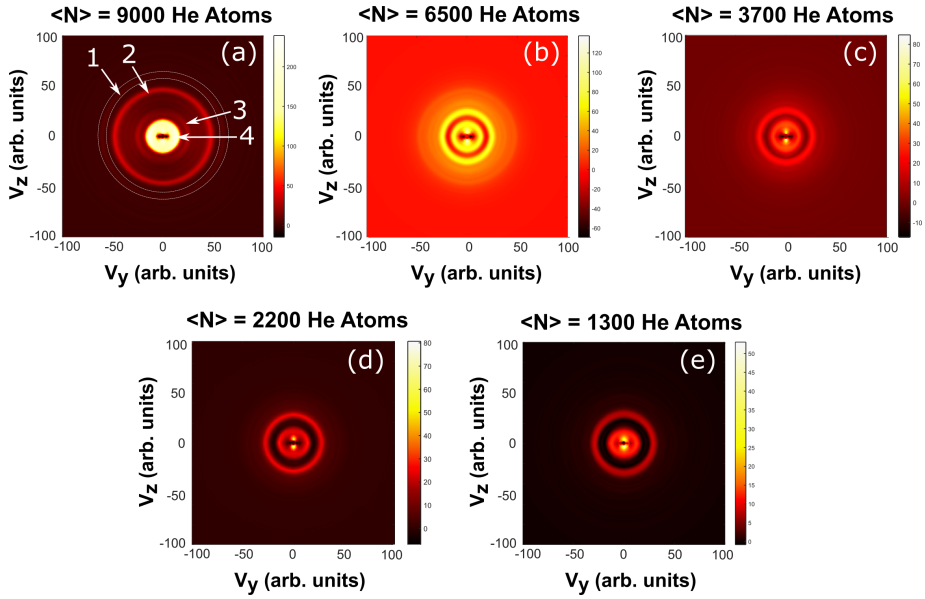


**Figure 5.9:** (a-e) Abel Inverted $Na^+$ Ion images of helium droplets doped with sodium and DMSO. Panel (a) is used to indicate the different channels through which $Na^+$ ions are produced. See text for details.

in which the sodium atom acquires a significantly higher velocity, as it has a mass 3.4 times smaller than DMSO. Developing further on the velocity of the ions from the perspective of the DMSO fragment, its low velocity and a large binding potential towards the center of the droplet hinder the detection of the $DMSO^+$ fragments. This prevents us from measuring the $DMSO^+$ and $Na^+$ in coincidence.
Going back to the sodium ions, an assignment of channel (3) to the Coulomb explosion channel can be built around three main arguments. First, the dopants are not expected to be found in a bound state which can be excited to a dissociative state, as they are located at distances on the order of tens of Å. The dopants remain at a fixed distance due to their interaction with the droplet, which keeps the sodium (or lithium) atom on the surface and DMSO (or other organic molecule) bound to the center. This suggests that the most feasible mechanism by which the sodium atoms are ejected from (hetero-doped) droplets is the Coulomb repulsion experienced with the molecular cation.
A second argument can be made based on the energetics of the process. If the channels corresponds to Coulomb repulsion, its energy can be calculated based on the distance between the alkali cation and the molecular ion. A good estimation of this distance can be made based on the droplet radii, which is determined by the conditions of the helium expansion (nozzle temperature and stagnation pressure [6]. A more detailed account of this second argument is provided later, in section 5.3.5.
Thirdly, as the Coulomb explosion channel shows a dependence that is well-characterized by the Coulomb-potential, a change in this distance should lead to a change in the velocity of the ions. In this regard, the possibility to change the droplet radii by controlling the expansion conditions strongly supports the assignment of the channel to the Coulomb channel. The dependence of the ions' velocity on the droplet size can be seen in fig.5.8 and 5.10.
The dependence of the energy on the droplet size is covered in more detail in the next section, and the use of this effect with the goal of measuring the characteristics of the droplet will be presented.

### 5.3.5 Distance Determination by Coulomb Explosion Imaging

As introduced in 5.2.2, Coulomb explosion imaging has been widely used as a technique to determine bond distances within a molecule, for instance for Van der Waals dimers, where the bond distance is 3-4 Å[99]. Here, we extend this technique and propose it as a tool to measure the distance between a dopant located in the interior of the droplet (bulk dopant) and a dopant adsorbed on the surface. Considering that the position of the surface dopant is representative of the surface position and that the bulk dopant is located in the centre of the droplet, this technique can be used to measure the distribution of droplet sizes within a helium droplet beam. This technique is an interesting method to determine droplet sizes because the Coulomb explosion method is a very direct way to measure distances.

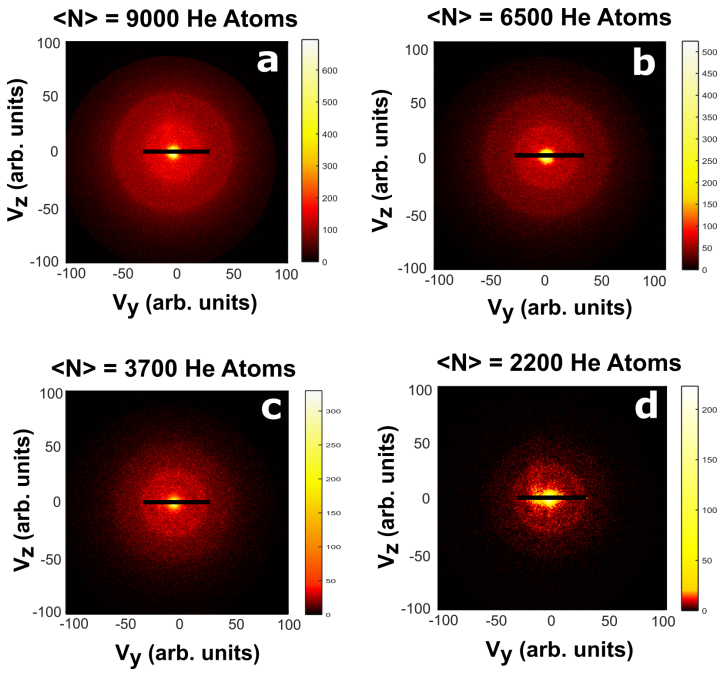


**Figure 5.10:** (a-d) $Li^+$ ion images for four different droplet sizes of mean size <N>. All the images were obtained for droplets codoped with DMSO.

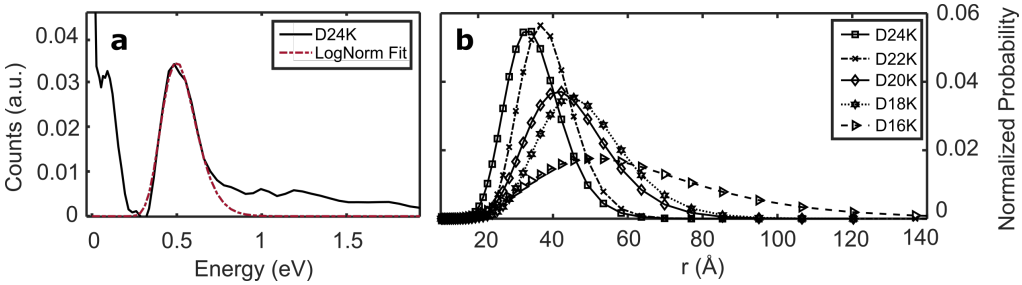


**Figure 5.11:** (a) In black, energy distribution of a $Na^+$ ion image obtained from droplets co-doped with DMSO. The expansion conditions for the droplet beam were of 24 K for the nozzle temperature and 50 bar for the stagnation pressure. In red, log-normal fit of the channel that corresponds to the $Na^+$-$DMSO^+$ channel (b) distribution of droplet radii, $r$, for a series of nozzle temperatures. The distributions are obtained from the fit as shown in panel (a).

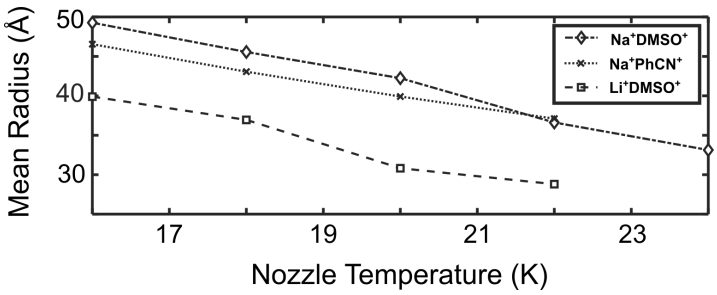


**Figure 5.12:** Mean droplet radii obtained as a function of the nozzle temperature for sodium/dimethyl sulfoxide (diamonds), sodium/benzonitrile (crosses) and lithium/dimethyl sulfoxide (squares). The stagnation pressure was 50 bar for all the measurements.

The droplet size distribution is obtained by fitting the Coulomb explosion channel to a log-normal function, as shown in fig.5.11a, the resulting energy distribution is converted into distance by applying equation 5.1. The distributions of radii extracted from this, normalized by area, are shown in fig.5.11b.
The mean radii calculated from three different alkali metal/molecule pairs are displayed in fig.5.12. Good agreement is found for the two dopant pairs where sodium is the surface dopant, and a discrepancy of around 5 Å is seen for the lithium/DMSO pair.

Some remarks can be made given that the droplet size distributions match fairly well values reported previously in the literature [26]. Firstly, that the CEI method can be successfully used to measure the distribution of droplet sizes. However, a more accurate fitting procedure (that accounts, for instance, for the baseline contribution) would be desirable to make the measurement more accurate. Secondly, the fact that the values measured with this technique correspond well with the values in the literature provides also information about the location of the dopants in the droplet. As stated above, two assumptions required for this method to be valid: that the position of the alkali metal is confined to the surface of the droplet (as stated in sec.2.4.1), and that the bulk dopant stays close to the center of the droplet. Thus, this data suggest that the bulk dopant is unlikely to free roam in the droplet and that it is likely to be localised relatively close to the center of the droplet. Recent experiments in the laboratory suggest that substituting the bulk dopant with a lighter dopant, such as argon, blurs the energy distribution of the metal ions. Even though these results are still preliminary, this could indicate that the localisation of the bulk dopant in the center can be assigned to its large mass and polarizability, while lighter dopants become more delocalized within the droplet.

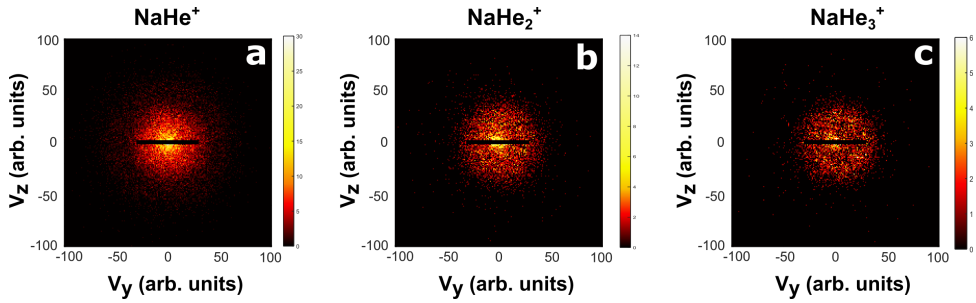


**Figure 5.13:** Ion images for (a) $NaHe^+$ (b) $Na(He_2)^+$ and (c) $Na(He_3)^+$. The images shown here were taken at the time delays for which the maximum ion yield for each of the complexes is observed, from a-c: 0.75, 1.5 and 2 ps, respectively. All the images shown here correspond to droplets codoped with DMSO.

### 5.3.6 Time Resolved Measurements

The experimental results shown in the last section strongly indicates that the Coulomb explosion of hetero-doped droplets yields a clearly distinct kinetic energy channel in the ion images (channel 3 in fig.5.9). Thus, the Coulomb channel offers an observable that enables following processes taking place in hetero-doped droplets and differentiate those from other ion channels.
However, following the solvation process in time requires defining an observable or a series of observables whose change in time can be related to solvation. In this regard, the Coulomb channel defined in the last section makes up a good starting point, but measuring the time evolution of the $Ak^+$ yield is not sufficient to follow the entire solvation process, as it does not provide information on the arrangement of the solvent around the ion or reflect the dynamics of the process.

As it will be shown in the simulation in section 5.3.7, the time evolution of the solvation process can be followed by looking at the increase in solvent density around the ion. The radial density profile peaks at distances where the solvent atoms gather more tightly around the atoms. These high-density areas can be related to the solvation layers introduced earlier in figure 5.2. Nonetheless, our experimental capabilities do not include measuring the radial density profile around the ion. Instead, the solvation process has been followed from a "molecular" perspective i.e., by the number of helium atoms that bind to the alkali ion as a function of time. Further considerations concerning what is considered "binding" will be given in the discussion section.
The observables of choice are therefore the time evolution of the ion yield of different $Ak(He_n)^+$ complexes. This can be done due to the capabilities offered by the TimePix3 (TPX3) camera, which records the ions' 2D momentum distribution and time-of-flight data simultaneously.
The TPX3 camera can record fast enough so that it records images with a time stamp, allowing to record images simultaneously for all the ions hitting the detector. This means

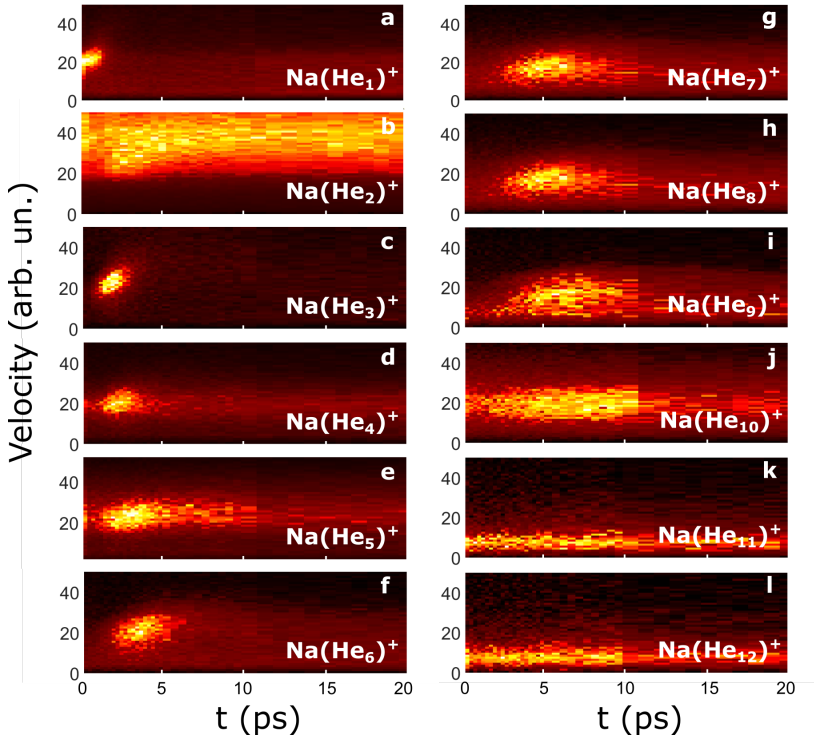


**Figure 5.14:** (a-l) radial contour plots for sodium ions and sodium-helium complexes after Coloumb explosion of $Na/CS_2$ hetero-doped droplets, formed at a nozzle temperature of 22K and a stagnation pressure of 50 bar.

that, as shown in fig.5.13, sodium (or any other alkali) and its corresponding series of helium complexes, $Na(He_n)^+$, can be recorded.

The ion images in fig.5.13 were then recorded at different time delays by introducing a probe pulse (800 nm), which results in the radial contour plots displayed in fig.5.14. Here, the time evolution of the velocity of the ions originated from the Coulomb channel can followed for a series of $Na(He_n)^+$ complexes (n= 1-12).

The radial contour plots in fig.5.14 show the time evolution of the ion yield for a series of $Na(He_n)^+$ complexes and the evolution of their velocity on the plane of the detector. The velocity of the ions is found to increase as a function of time, meaning that the ions produced at later time delay feature higher velocities than those produced earlier. The difference in velocity between the early fragments and those produced at longer time delays is seen to decrease as the number of helium attachments becomes larger. Given that the process under study is the solvation of the cation and its progressive approach to the center of the droplet, a first consideration should be whether the increase in the velocity of the ions arises from the closer proximity of the cations to the co-dopant (as derived from the inverse dependence on the distance, see eq.5.1). However, the timescale at which the increase in velocity takes place, and the sudden decay of the signal do not

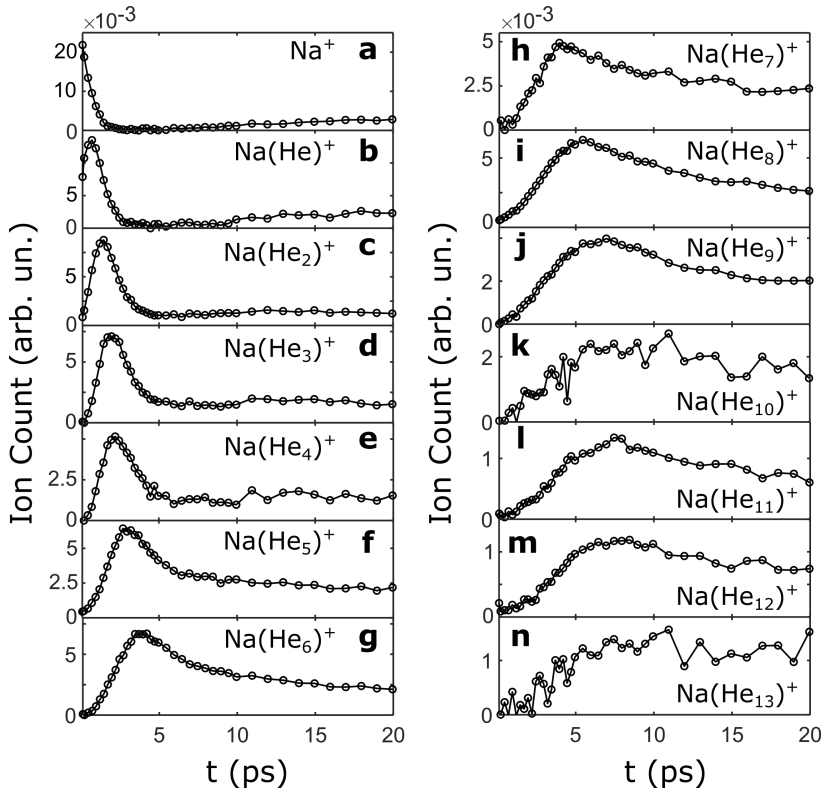


**Figure 5.15:** (a-n) time evolution of $Na^+$ and $Na(He_n)^+$ after Coloumb explosion of Na/Naphthalene hetero-doped droplets, formed at a nozzle temperature of 18K and a stagnation pressure of 50 bar.

support this explanation. Instead, we suggest that the increase in velocity observed for ions appearing later should be explained by considering the distribution in droplet sizes. It is proposed that the increase in velocity for later fragments stems from the probing process and not from the physics of the system under study itself.

Due to the distribution in droplet sizes, the Coulomb repulsion that ions experience will depend on the size of the droplet on which they are doped. Summoning again eq.5.1, the inverse dependence on the distance between the alkali cation and the molecular dopant determines the repulsive potential experienced by the ion and by extension its final velocity. A more extensive discussion of this will be done in section 5.4.1, where the effect of the probe on the state of the ion will be carried out.

Concerning the ion yield, these plots reveal that the maximum yield is achieved at later time delays as the number of helium atoms attached becomes larger. A more clear observation of the time evolution of the ion yield can be obtained by integrating the ion counts assigned to the Coulomb channel, which can be done by applying a radial constraint to the ions that are integrated. The time evolution of the ion yield resulting from this is shown in fig.5.15. Here, it can be more clearly seen that the time delay at

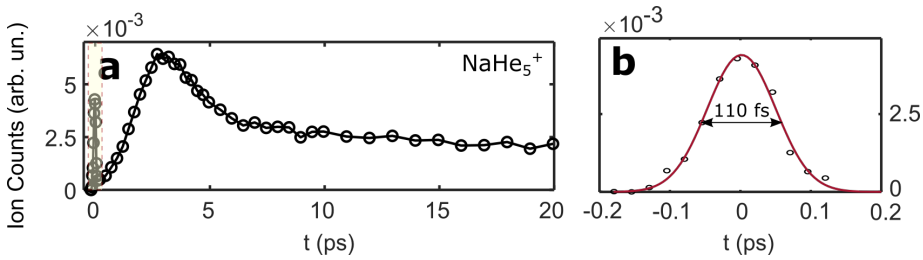


**Figure 5.16:** (a) Temporal evolution for the ion yield of $Na(He_5)$. (b) zoom-in of the area shaded in yellow, which corresponds to the cross-correlation of the pump (800 nm) and probe (400 nm) pulses. The cross-correlation is obtained through the increase in ion yield from fragmentation of the naphthalene molecule during the overlap of the pump and probe pulses. The fragment (m/z = 43) can be assigned to $(C_3H_3)He^+$.

which the maximum ion yield is observed increases with the number of helium atoms in the complex.
Due to the presence of contaminants in the chamber, the ion yields have been background subtracted in order to correct for the contributions from overlapping fragments; the background observed for $Na(He_7)^+$ corresponds to $C_4H_3^+$ fragments, while the background for $Na(He_{10})^+$ can be assigned to $C_8H_3^+$. The overall dynamics of the sodium ion or the sodium-helium complexes are not affected due to the much faster dynamics of these fragments.

The presence of overlapping fragments can be used in the advantage of the experiment. The increased ion yield observed for some fragments during the pump-probe overlap provides an *in situ* measurement of the pump-probe cross-correlation. As an example, the time evolution of the ion yield of $Na(He_5)^+$ is shown in fig.5.16a. Fig.5.16b is a zoom in of the time window where the pump and probe pulses overlap. The overlap leads to an increase in the ion counts, which can be used as an *in situ* cross-correlation. As shown in fig.5.16b, the full-width half-maximum (FWHM) of the cross-correlation is of 110 fs. In comparison, the FWHM of the cross-correlation of the pump and the probe pulses, obtained by recording their sum frequency signal (266 nm) generated in a BBO crystal is 130 fs.

In order to extend the method to other alkali metals and to test its robustness, we set ourselves to perform experiments on nanodroplets where lithium is found on the surface instead of sodium.
The time evolution of the ion yields for $Li^+$ and $Li(He_n)^+$ complexes is shown in fig.5.17. The ion yield time evolution of lithium and lithium complexes is qualitatively equivalent to that previously observed for sodium: the larger the complex, the later its ion yield reaches its maximum.

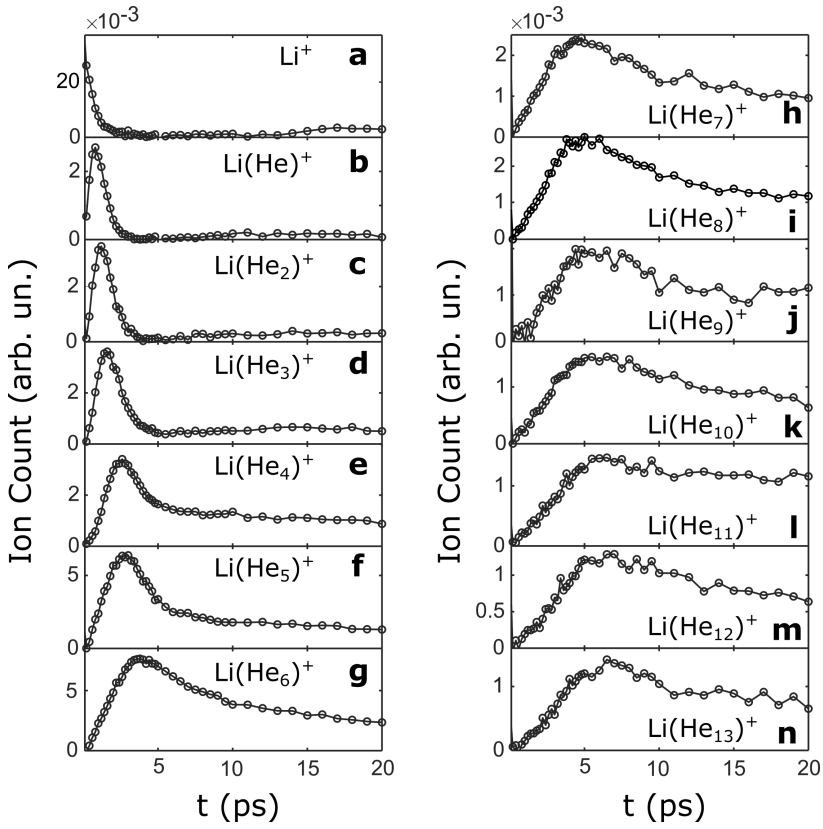


**Figure 5.17:** (a-n) time evolution of the ion yield for $Li^+$ and $Li(He_n)^+$ after Coloumb explosion of $Li/CS_2$ hetero-doped droplets, formed at a nozzle temperature of 18K and a stagnation pressure of 50 bar.

A comparison of the solvation dynamics of sodium and lithium is presented in fig.5.18. Here, the time delay at which the ion yield of a given alkali-helium complex reaches its maximum is plotted as a function of the number of helium atoms attached. The plot reveals that the rate at which helium atoms attach to the ion follows a linear trend up to ca. 8 helium attachments for lithium and ca. 12 helium attachments for sodium. From the fits (see fig.5.18) we interpret the linear behaviour as the $Li^+$ ($Na^+$) ion binding one He atom every 0.7 ps for the first 8 (12) atoms.

### 5.3.7 TDDFT Simulation

A simulation based on time-dependent density functional theory (TDDFT) is presented in order to get further insight into the experimental results. The simulations were performed by prof. Manuel Barranco and prof. Martí Pi, from Universitat de Barcelona. A detailed account of the simulation procedure is out of the scope of this text (and of

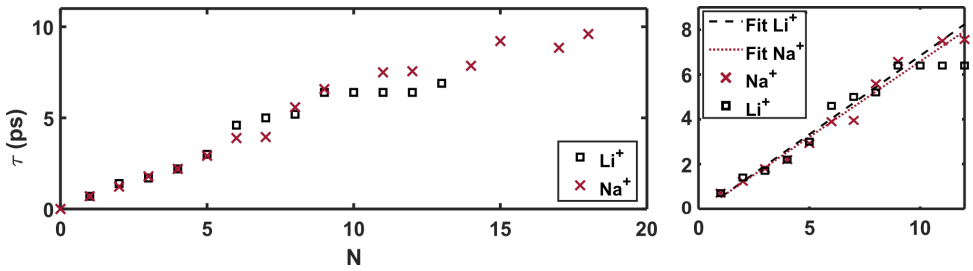


**Figure 5.18:** Time delay corresponding to the maximum ion yield ($\tau$) for $Ak(He_N)^+$.

my own understanding), but the reader is referred to a series of publications by prof. Pi and prof. Barranco [106, 107, 108]. The calculations are started from the equilibrium configuration of a droplet consisting of 2,000 helium atoms and a sodium atom. The equilibrium position is calculated from the ground-state Na-He potential in ref.[109]. The dynamics are triggered by changing the interaction potential between the atom and the droplet by switching the pair potential from that of Na-He to that of $Na^+$-He, leaving an out-of-equilibrium configuration for $Na^+$@He2000. This strategy was already applied to Cs, Rb [110] and Ba [111]. The pair-potential for the $Na^+$He interaction is taken from ref. [112]. The helium is represented by a complex effective wavefunction *ψ(r,t)*, so that the helium density can be found as $|\psi(r,t)|^2$. It is deemed valid to treat the motion of the $Na^+$ ion classically, due to its large mass compared to that of helium. Within the DFT method used, other applications used in the simulation are the Born-Oppenheimer approximation, the Franck-Condon approximation and the diatomics-in-molecules approximation. The time evolution of the wavefunction is given by:

$$i\hbar\frac{\partial}{\partial t}\psi = \big[-\frac{\hbar^2}{2m_{He}}\nabla^2 + \frac{\delta\epsilon_c}{\delta\rho(r)} + V_X^+(|r - r_{Na+}|)\big]\psi \tag{5.9}$$

where the functional term $\epsilon_c$ contains the He-He interaction, $\rho(r)$ is the helium density and $V_x^+$ is the He-$Na^+$ pair potential. The position of the sodium cation, $r_{Na^+}(t)$, is calculated by:

$$m_{Na} + \ddot{r}_{Na+} = -\int d\mathbf{r}\big[\nabla\rho(\mathbf{r})\big]V_X^+(|r - r_N a^+|)\big] \tag{5.10}$$

The equations have been solved with a time step of 0.5 fs and a space step of 0.4 Å. The equilibrium geometry for the Na atom attached to a helium droplet is shown in fig.5.19a1. Here, the atom is seen to reside on a dimple on the surface, with no helium density directly surrounding it (see panel fig.5.19b1). Ionizing the atom triggers a dynamic response of the system, as the depth of the pair potential of $Na^+$-He is significantly deeper than that of Na-He. This results in the helium atoms approaching the cation and in a build-up of helium density around $Na^+$. Fig.5.19a2 shows a snapshot of the system 10.0 ps after ionization. Here, the density of helium around the cation is found to be much larger, as seen in panel fig.5.19b2, where a peak of density is found at 2.5

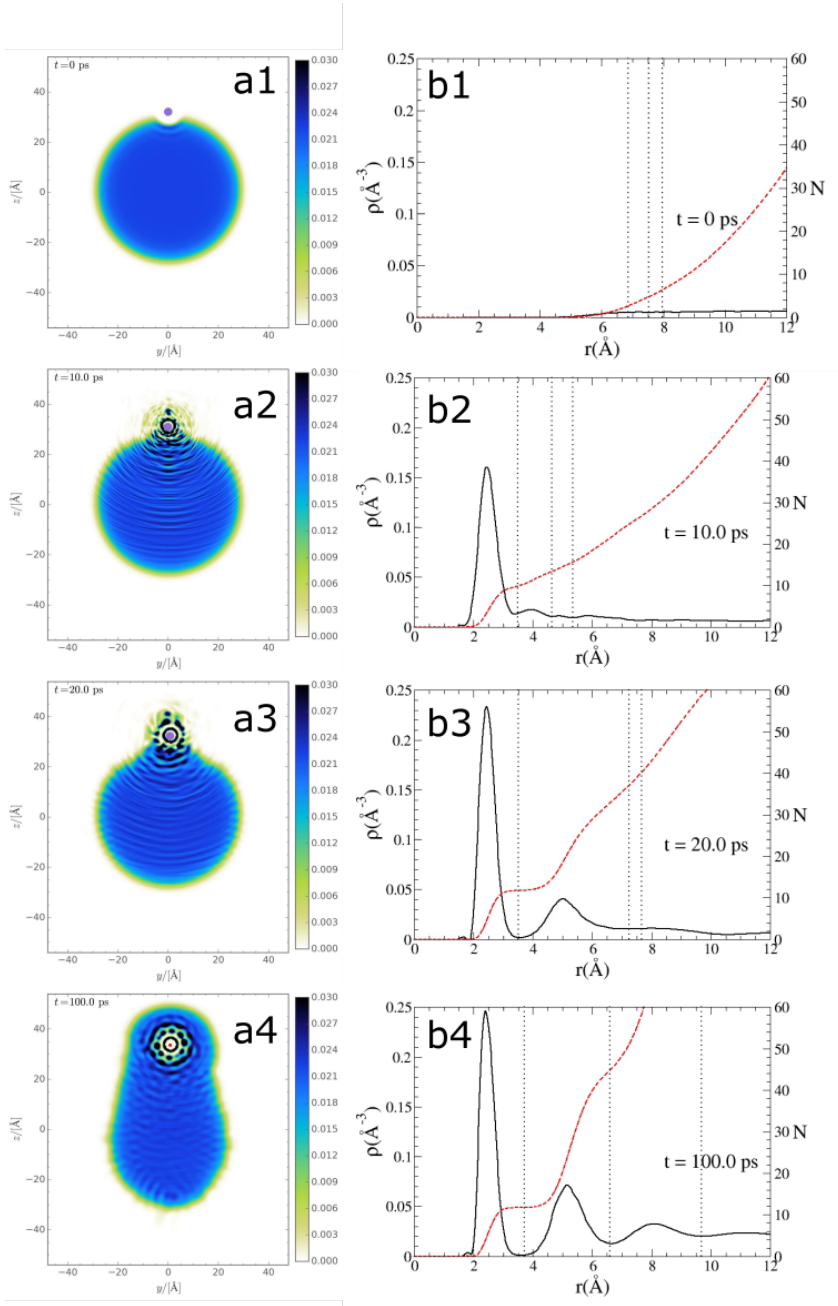


**Figure 5.19:** TDDFT Simulation of the solvation of a Na+ cation in liquid helium. Panels a1-a4 show the sodium cation (purple circle) and the helium density at time delays of 0, 10, 20 and 100 ps, respectively. The darker areas represent higher helium density. Panels b1-b4 show the radial density profile of the images. The simulations were performed by prof. Manuel Barranco and prof. Martí Pi (Universitat de Barcelona).

Å. At this point the formation of the first solvation layer is almost complete, although the density has not yet reached is maximum. Fig.5.19a3 and fig.5.19b3 show the helium density around the cation 20.0 ps after ionization. At this point an increase in the helium density in the first solvation layer (2.5 Å)is found and an increase in the density at 5 Å can also be seen, which corresponds to the formation of the second solvation layer.
Finally, the helium density distribution 100.0 ps after ionization is shown in fig.5.19a4, and the radial density profile in fig.5.19b4. It is possible to observe the formation of a third solvation layer, and an equilibration of the helium density around the cation. Despite this, the helium droplet remains out of equilibrium and shows an elongated shape, which pressumably does not correspond to its equilibrium geometry. However, the droplet dynamics are not seen in the time window of the simulation and are also out of the interest of this experiment, where the interest lies in the build-up of helium around the alkali cation i.e., its solvation dynamics.

## 5.4 Discussion

### 5.4.1 Effect of the Probe on the Solvation State of the Ion

One aspect of this experiment which should be discussed is the extent to which the dynamics observed are representative of the real solvation dynamics. In other words, it should be considered how does our probing process affect the dynamics of the system. As it was schematized in fig.5.4, the bulk dopant is ionized in the probing event, leading to a repulsive interaction with the alkali metal cation. The repulsion experienced by the metal cation ejects it away from the droplet, after which its velocity can be measured. Fig.5.8 and fig.5.10 result from the velocity distribution of alkali metal cations, and as it was shown in sec.5.3.5, this velocity is proportional to the distance between the surface dopant (Ak) and the bulk dopant (M). The droplet sizes extracted from the images have been deemed to be an accurate representation of the droplet size by comparison with other experimental work, mainly due to the small degree of scattering that the alkali atom experiences, as it is located in the surface of the droplet and hence does not undergo multiple collisions on its way out.
Nonetheless, studying the solvation dynamics of the ion requires an analysis of the solvation state of the ion i.e., the number of helium attachments as a function of time, and not only analysis of the velocity distribution of the ions. The key point is therefore, whether the number of helium atoms that accompany the ion to the detector are a snapshot of the amount of helium atoms that are bound to the ion at the time of ejection. Ideally, the experiments aims at ejecting the alkali metal complexes without altering the number of helium atoms that are bound to the ion.
In this regard, there are two possible ways in which the probing process can affect the solvation state of the ion - by picking up more helium atoms while it is ejected, or by losing them on its way out. The pick-up of additional helium atoms can occur through collisions with pairs of solvent atoms, which leads to attachment of the solvent atoms to

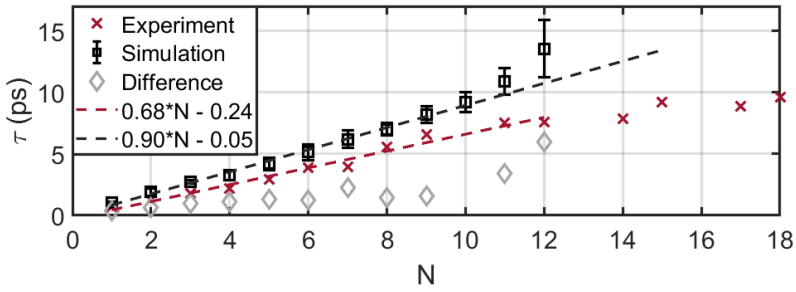


**Figure 5.20:** Experimentally determined values for the maximum ion yield of a given Na complex with N helium attachments (red crosses) and linear fit of the data points up to N =10 (red dotted line). Values obtained from the simulation (black squares) and linear fit of the first 10 data points (black dashed line). The discrepancy between the experimental data and the simulation is shown as grey diamonds.

the ion. This is a well-known phenomenon referred to as snow-ball formation, which has been extensively reported for helium-embedded species [113], but not observed with time resolution.
Pick-up of more helium atoms after the probe interaction can also take place due to the finite amount of time that it takes for the ion to leave the droplet. In other words, additional helium atom attachments can occur in the time that elapses in between the ionization of the bulk dopant and the ion leaving the droplet.
Lastly, the loss of helium attachments can be caused by providing enough energy in the probing process to break-up $Ak^+$-He bonds.

To start the discussion, the possibility of picking up additional helium atoms will be examined. The alkali metal atom is initially adsorbed on the surface, which implies that it encounters no helium atoms on its way out of the nanodroplet. This applies to the early time delays in the experiment but a different scenario arises as helium atoms creep around the ion. As a result, a change in the dynamics for helium attachments is to be expected as the ion is surrounded by solvent atoms. This change in dynamics manifests in fig.5.18, where a change in slope is observed for a given N value (8 for $Li^+$, 12 for $Na^+$). The initial slope of ca. 700 fs, which reasonably fits the timescale for bond formation, decreases to sub-100 fs after the aforementioned N values.

More insight into the dynamics can be obtained by comparison with the TDDFT simulation. Fig.5.20 shows the time delay at which a sodium ion containing N helium attachments reaches its maximum yield as extracted from the experimental data (red crosses) and from the TDDFT simulation (black squares). The simulation and the experimental data agree to within a picosecond up to N = 10, but at larger N values the discrepancy becomes larger. It is likely that increasing difference in $\tau$ values as N becomes larger is caused by the appearance of a new source of helium attachments as the solvation process progresses. As the sodium ion becomes surrounded by an increasingly large

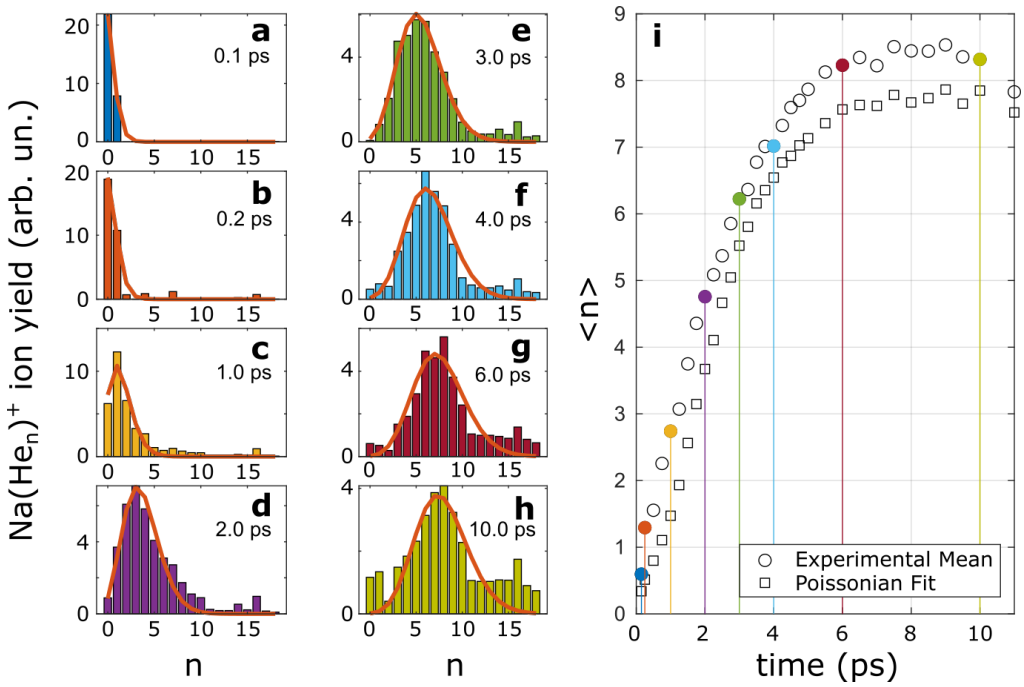


**Figure 5.21:** (a-h) Experimental distribution of Na(He$_n$)$^+$ complexes as a function of the number of helium attachments (n) corresponding to time delays of 0.1, 0.2, 1.0, 2.0, 3.0, 4.0, 6.0 and 10.0 ps. The solid orange line corresponds to a Poissonian fit of the experimental data (shown as bars) (i) time evolution of the mean number of helium atoms attached to the cation as extracted from the experimental data (circles) and from the Poissonian fit of the experimental data (squares). The distributions shown in panels (a-h) are highlighted in panel (i) by using the same colour-coding.

layer of helium, so does the probability of capturing $N$ helium atoms through two-body collisions as the ion is ejected from the droplet. While the simulation predicts slower dynamics after the first solvation layer has been fully formed (N=12), the experimental data shows the contrary behaviour. Based on this, it is suggested that the increased time constant for helium attachments above N = 12 is a result of the probing process and not a direct consequence of the solvation process itself. Due to the sudden "kick" that the ion gets towards the outside of the droplet, it collides with a relatively high energy with solvent atoms on its way out, with a finite probability of forming additional Na-He bonds.

The number of helium atoms bound to the sodium cation as a function of time is represented in fig.5.21. Here, the ion yield for each Na(He$_n$)$^+$ species at a given pump-probe time delay is shown as a bar graph (panels a-e). The distribution of complexes at a given time delay can be fitted to a Poisson distribution, as shown by a red dashed line. Panel f shows the average number of helium atoms attached to sodium as a function of time. From this plot, it can be seen that the increase in the (average) number of

helium atoms stops at around 10 ps (8 He atoms), later to be followed by a decrease. A comparison of the average number of atoms obtained by the Poissonian fit (squares) and the experimental data (circles) shows that the the distribution of complexes at a given time delay is represented well by a Poissonian distribution of helium attachments.
Although the physical meaning of the Poissionian distribution is still being discussed, it can be interpreted as suggesting that the probability for a helium attachment taking place is independent of the number of helium atoms that have been already attached to the cation.

## 5.5 Conclusion

The study of the solvation dynamics of two alkali metal cations (sodium, lithium) with femtosecond time resolution and at the single-particle level has been achieved by means of ion imaging in conjunction with the extended capabilities provided by the TimePix3 camera.
Our results show that a helium atom binds to $Na^+$ (or $Li^+$) every 700 fs, and that each subsequent helium attachment is independent of the number of helium atoms already bound to the cation up to ca. 12 He atoms for sodium and 8 He atoms for lithium.
In addition to measuring the solvation dynamics of two alkali cations, Coulomb explosion imaging is proposed as an effective, more direct than previously reported techniques, way of measuring the distribution of droplet sizes in a helium droplet beam. Besides accessing the size distribution of helium droplets, this technique can also be exploited as a method to image the localisation of dopants within the helium droplet helium.

*"I find the great thing in this world is not so much where we stand, as in what direction we are moving: To reach the port of heaven, we must sail sometimes with the wind and sometimes against it,—but we must sail, and not drift, nor lie at anchor."*

— Oliver Wendell Holmes

# 6 Conclusion and Outlook

This last chapter is devoted to briefly present future experiments that follow naturally to the observations and conclusions presented throughout this thesis. The chapter is structured around the main three chapters that constitute the thesis itself: rotational dynamics in helium nanodroplets, photodissociation dynamics in helium nanodroplets and solvation dynamics of alkali metals in liquid helium. Finally, some remarks concerning the use of helium nanodroplets as matrices for chemical reactions at low temperature will be made.

## 6.1 Rotational Dynamics in HeNDs

The study of rotational dynamics in helium carried out during this thesis includes two differentiated parts: the application of rotational coherent spectroscopy (RCS) as a tool in the investigation of the interaction between liquid helium and a rotationally excited molecular dopant and the use of laser-induced alignment as a tool to control molecular orientation in helium-embedded dopants.

### 6.1.1 Exploring Rotational Coherence in the Superfluid Regime

One aspect of liquid helium that draws considerable attention within the physics community is its superfluidity. Nonetheless, it was covered in chapter 3 that superfluidity is limited to excitation energy below the roton excitation of the droplet.
An interesting direction to pursue is whether molecules preserve rotational coherence for long time delays in helium nanodroplets. To follow this direction, the rotational excitation put into the molecule must be well below the roton gap, in the superfluid

regime.
Rotational coherence can be kept up to very long time delays in the gas phase due to the low centrifugal distortion constant, which is the main parameter in determining the dephasing of the wavepacket. In helium nanodroplets, much larger centrifugal distortion constants are observed and therefore the rotational wavepacket would be expected to dephase faster. This is why boron subphthalocyanine is a good candidate for these experiments - the centrifugal distortion term is lower in molecules with low rotational constants, as it is the case for boron subphthalocynanine. The experiment proposed here, as a continuation of the results presented in chapter 3, is to perform RCS of boron subphthalocyanine in helium nanodroplets. The low rotational constant (and centrifugal distortion) bestow SubPc with a long revival time and a gas-phase like behaviour consequence of its low centrifugal distortion constant, increasing the likelihood of the rotational coherence to be preserved at long time delays.
In addition to this, it is also of interest to perform Fourier analysis of the alignment dynamics in order to gather more evidence for how does the $B/B^*$ ratio evolve as a function of mass.

## 6.2 Photodissociation dynamics in HeNDs

The photodissociation dynamics of iodobenzene and iodine have been presented in chapter 4. The initial intention of the experiment was to measure the time that it takes for a photofragment to escape from the helium nanodroplet, by tuning a spectrally narrow laser pulse to selectively (2+1)-photon ionize iodine atoms in the gas-phase. It was observed that the signal from the photofragments kept rising up to time delays that are much longer than what would be expected considering the initial velocity of the fragments and the size of the droplets. Following this observations, it was hypothesized that the slow dynamics stem from recombination of the photofragments through an effect analogous to the "cage-effect".
The conclusions reached from the experiments are based on the dynamics of (2+1)-photon ionized iodine and the nonresonant (strong-field) ionization at both 800 nm and 400 nm. The conclusions reached concerning the mechanism proposed for the dynamics observed are tentative, due to the difficulty of recognizing the electronic states involved in the ionization process. Due to the complexity of this process, additional experiments should be carried out in order to confirm or rule out the recombination hypothesis.

### 6.2.1 Recombination Dynamics

As summarized in fig.4.15, the slow dynamics observed were attributed to a resonance of a vibrationally excited iodobenzene molecule. The vibrational state in conjunction with the wavelength of the probe are thought to determine the probing efficiency, as shown by the different dynamics observed by probing with three different colours (298 nm, 800 nm and 400 nm).

Following this, it is suggested to carry out this experiment with a range of spectrally narrow probes of different wavelengths. If the hypothesis here exposed is correct, probing with different colours should yield slower dynamics for lower wavelengths. The argumentation for this follows that given that ionization occurs through resonance with a cationic dissociative state, higher energies probe lower vibrational levels and therefore more time is needed for the solvent to induce vibrational relaxation to a state that can be excited to a high-lying electronic state, where iodine in its cationic state is formed.

### 6.2.2 Further Photodissociation Experiments

In the experiments performed during these thesis, the fragments studied have been mainly iodine atoms. In order to clarify the recombination mechanism, it is suggested that photodissociation experiments that produce other photofragments should be performed. The recombination efficiency can be studied by measuring a series of molecules with different photofragment-helium pair potentials.

## 6.3 Solvation Dynamics of Alkali Metals in Liquid Helium

The solvation dynamics of sodium and lithium in liquid helium have been the most recent results obtained in the group and possibly those that lay the ground for the most likely follow-up experiments. The results shown in chapter 5 are, to our knowledge, the first experimental results concerning solvation dynamics on its natural timescale with single-particle resolution.

### 6.3.1 Alkali Metals

A natural step in these experiments is to extend the measurement of solvation dynamics to the entire series of alkali metals. Especially, performing measurements on larger alkali metals could yield significantly different dynamics to those recorded for sodium and lithium. Observing different solvation dynamics would be highly interesting from the perspective of theoretical modelling of helium nanodroplets. In order to add interest to these experiments, it is suggested that continuing the collaboration with theoreticians could yield an interesting perspective that could potentially be employed as a method to benchmark the TDDFT calculations.

### 6.3.2 Alkaline Earth Metals

Alkaline earth metals have been found to be located near the surface but sunk deeper into the "dimple" than alkali metals [114]. This provides an interesting system to further study solvation dynamics in helium. Furthermore, alkaline earth meatals can be doubly ionized, which can be used to investigate the solvation dynamics for the doubly-charged ion as compared to the singly-charged ion.

### 6.3.3 Complex Formation

Even though this has not been included in the thesis, we carried out a series of experiments that aimed at understanding the physics dominating the formation of complexes between alkali metals and organic molecules residing in the center of the droplet. The $(Ak\text{-}M)^+$ complexes could be detected when using low-enough laser intensities. This was achieved in one-pulse experiments with defocused 800 nm light that ensured the selective ionization of the alkali metal without ionizing the molecule in the center of the droplet.
Our understanding of these series of experiments was that as the alkali metal is ionized, it will travel towards the center of the droplet and eventually meet with the molecule residing inside of the droplet, forming a complex. Indeed, $(Ak\text{-}M)^+$ complexes were detected, along with their corresponding helium attachments, but detection of the complexes proved to be dependent on the nature of M i.e., the bulk dopant.
Our experiments posed a number of questions that suggest a series of experiments on this line.

#### 6.3.3.1 Molecular Properties and Complex Formation

The set of experiments carried out within this subsection concern the study of the dependence of the complex formation on dielectric properties such as the molecular polarizability or dipole moment. Given that this is an interesting questions and that the experiments performed so far have not been enough to identify a clear relation, more thorough experiments are suggested as a next step.

#### 6.3.3.2 Detection of Ak-M covariance

The TPX3 camera enables the detection of simultaneous ionic species and as such provides the opportunity to measure correlations between ions with a different m/z ratio. So far it was not possible to detect angular (or radial) covariance between any alkali metal (sodium, lithium) or molecular dopant (DMSO, $CS_2$, benzonitrile, naphthalene).
The lack of covariance is not fully understood but we suggest that it is due to the fact that the molecular species does not escape the droplet as its velocity is too low due to the share of momentum with the alkali ion.
However, it is suggested that performing experiments at long pump-probe time delays (e.g. 4-10 ns) could allow the detection of angular covariance between the two species. It was argued that M is not detected because it is too slow to escape the droplet, but the reason by which the complexes are detected in the first place has not been yet discussed. Given that $(Ak\text{-}M)^+$ complexes are detected in one-pulse experiments, the system can be considered to have fully equilibrated by the time the fragments reach the detector. The complexes are thus thought to "escape" the droplet by getting rid of the helium solvent due to dissipation of the excess vibrational energy found in the complex once it is formed.

This argumentation is the reason for suggesting a long pump-probe time delay; this would enable the full relaxation of the complex and its corresponding de-solvation, which would afford a significant population of complexes in the gas-phase from which angular covariance can be measured.

#### 6.3.3.3 Vibrational Relaxation in the Droplet

Building up on the experiment suggested in last section, finding the timescale for the rise of the $(Ak\text{-}M)^+$ covariance signal would open up for the possibility of measuring the dynamics of vibrational relaxation in liquid helium. Once the timescale for the complex formation is identified by performing the experiments suggested in the last section, a time-resolved measurement could be carried out as a way of studying the dynamics of vibrational relaxation in helium nanodroplets.

### 6.3.4 Measurement of Nanometric Distances by Coulomb Explosion Imaging

In addition to the time-resolved experiments, there are a number of one-pulse experiments to be carried out. As it was shown in chapter 5, Coulomb exploding hetero-doped droplets yields structural information about the droplet. On this regard, future experiments should be carried out in order to optimize the accuracy of the technique and ideally, benchmarking it by comparison to experimental results obtained with other techniques. With the aim of improving its accuracy, it is suggested that the first parameter to investigate is the nature of the bulk dopant. The spread in kinetic energy measured after Coulomb explosion is the main source of uncertainty in the experiment and one origin for this spread is likely to be excessive fragmentation of the organic molecule used as bulk dopant. Thus, the choice of a dopant that undergoes less fragmentation could be beneficial.

### 6.3.5 Measuring the Localization of Dopants in the Droplet

The localization of neutral impurities in the helium nanodroplet has been a topic of debate within the helium nanodroplet community [28]. It is suggested that the Coulomb explosion imaging technique introduced here can be used to add new experimental evidence to this debate by performing a more direct measurement of the dopants wavefunction within the droplet.
Preliminary measurements in our group reveal that a broader distribution of distances is measured by introducing smaller bulk dopants. In addition to the results shown in chapter 5, measurements employing neon as a bulk dopant indicate that neon atoms are more delocalized within the droplet.

## 6.4 Chemical Reactions in Helium Nanodroplets

The long-term goal of the experiments presented here is the realization of chemical reactions in helium nanodroplets. The interest for this lies in exploring chemical reactivity at low temperature, and expanding gas-phase experiments by introducing a dissipative medium that interferes minimally with the chemical reaction. Some advantages the helium nanodroplet technique include, as mentioned earlier, the ease of forming complexes between large molecules and its very broad spectral window.
Due to the findings within the solvation dynamics of alkali metals, the direction of future experiments in the near future is likely to be expanding this results into a myriad of systems, as exposed above.

# Bibliography


[1] S. R. Logan. The origin and status of the arrhenius equation. *J. Chem. Ed.*, 59(4):279, April 1982.

[2] M. E. El-Khouly, E. El-Mohsnawy, and S. Fukuzumi. Solar energy conversion: From natural to artificial photosynthesis. *J. Photochem. Photobio. C: Photochem. Rev.*, 31:36–83, 2017.

[3] T.E. Gough, M. Mengel, P.A. Rowntree, and G. Scoles. Infrared spectroscopy at the surface of clusters: SF6 on ar. *J. Chem. Phys.*, 83(10):4958–4961, November 1985.

[4] A. Scheidemann, J.P. Toennies, and J.A. Northby. Capture of neon atoms by $^4$he clusters. *Phys. Rev. Lett.*, 64(16):1899–1902, April 1990.

[5] M. Hartmann, R.E. Miller, J.P. Toennies, and A. Vilesov. Rotationally resolved spectroscopy of SF6in liquid helium clusters: A molecular probe of cluster temperature. *Phys. Rev. Lett.*, 75(8):1566–1569, August 1995.

[6] D.M. Brink and S. Stringari. Density of states and evaporation rate of helium clusters. *Z. Phys. D Atom Mol. Cl.*, 15(3):257–263, September 1990.

[7] S. Grebenev, M. Hartmann, A. Lindinger, N. Pörtner, B. Sartakov, J.P. Toennies, and A.F. Vilesov. Spectroscopy of molecules in helium droplets. *Phys. B: Cond. Matt.*, 280(1-4):65–72, May 2000.

[8] M. Hartmann, F. Mielke, J.P. Toennies, A.F. Vilesov, and G. Benedek. Direct spectroscopic observation of elementary excitations in superfluid he droplets. *Phys. Rev. Lett.*, 76(24):4560–4563, June 1996.

[9] J. Friedrich and D. Haarer. Photochemical hole burning: A spectroscopic study of relaxation processes in polymers and glasses. *Ang. Chem. Int. Ed.*, 23(2):113–140, February 1984.

[10] S. Grebenev, J.P. Toennies, and A.F. Vilesov. Superfluidity within a small helium-4 cluster: The microscopic andronikashvili experiment. *Science*, 279(5359):2083–2086, March 1998.

[11] M.V. Rama Krishna and K.B. Whaley. Microscopic studies of collective spectra of quantum liquid clusters. *J. Chem. Phys.*, 93(1):746–759, July 1990.

[12] P. Sindzingre, M.L. Klein, and D.M. Ceperley. Path-integral monte carlo study of low-temperature $^4$he clusters. *Phys. Rev. Lett.*, 63(15):1601–1604, October 1989.

[13] L.F. Gomez, K.R. Ferguson, J.P. Cryan, C. Bacellar, R.M.P. Tanyag, C. Jones, S. Schorb, D. Anielski, A. Belkacem, C. Bernando, R. Boll, J. Bozek, S. Carron, G. Chen, T. Delmas, L. Englert, S.W. Epp, B. Erk, L. Foucar, R. Hartmann, A. Hexemer, M. Huth, J. Kwok, S.R. Leone, J.H.S. Ma, F.R.N.C. Maia, E. Malmerberg, S. Marchesini, D.M. Neumark, B. Poon, J. Prell, D. Rolles, B. Rudek, A. Rudenko, M. Seifrid, K.R. Siefermann, F.P. Sturm, M. Swiggers, J. Ullrich, F. Weise, P. Zwart, C. Bostedt, O. Gessner, and A.F. Vilesov. Shapes and vorticities of superfluid helium nanodroplets. *Science*, 345(6199):906–909, August 2014.

[14] E. Lugovoj, J.P. Toennies, and A.Vilesov. Manipulating and enhancing chemical reactions in helium droplets. *J. Chem. Phys.*, 112(19):8217–8220, May 2000.

[15] C.D. Jonah, R.N. Zare, and Ch. Ottinger. Crossed-beam chemiluminescence studies of some group IIa metal oxides. *J. Chem. Phys.*, 56(1):263–274, January 1972.

[16] M.P. de Lara-Castells, A.W. Hauser, and A.O. Mitrushchenkov. Ab initio confirmation of a harpoon-type electron transfer in a helium droplet. *J. Phys. Chem. Lett.*, 8(17):4284–4288, August 2017.

[17] M. Renzler, M. Daxner, L. Kranabetter, A. Kaiser, A. W. Hauser, W.E. Ernst, A. Lindinger, R. Zillich, P. Scheier, and A.M. Ellis. Communication: Dopant-induced solvation of alkalis in liquid helium nanodroplets. *J. Chem. Phys.*, 145(18):181101, November 2016.

[18] K. Nauta and R.E. Miller. Nonequilibrium self-assembly of long chains of polar molecules in superfluid helium. *Science*, 283(5409):1895–1897, March 1999.

[19] G.E. Douberly, R.E. Miller, and S.S. Xantheas. Formation of exotic networks of water clusters in helium droplets facilitated by the presence of neon atoms. *J. Am. Chem. Soc.*, 139(11):4152–4156, March 2017.

[20] K. Nauta and R.E. Miller. Formation of cyclic water hexamer in liquid helium: The smallest piece of ice. *Science*, 287(5451):293–295, January 2000.

[21] H.H. Kristensen, L. Kranabetter, C.A. Schouder, C. Stapper, J. Arlt, M. Mudrich, and H. Stapelfeldt. Quantum-state-sensitive detection of alkali dimers on helium nanodroplets by laser-induced coulomb explosion. *Phys. Rev. Lett.*, 128(9), March 2022.

[22] M. Schlesinger, M. Mudrich, F. Stienkemeier, and W. T. Strunz. Dissipative vibrational wave packet dynamics of alkali dimers attached to helium nanodroplets. *Chem. Phys. Lett.*, 490(4-6):245–248, April 2010.

[23] B. Grüner, M. Schlesinger, Ph. Heister, W. T. Strunz, F. Stienkemeier, and M. Mudrich. Vibrational relaxation and dephasing of rb2 attached to helium nanodroplets. *Phy. Chem. Chem. Phys.*, 13(15):6816, 2011.

[24] J. Higgins, C. Callegari, J. Reho, F. Stienkemeier, W.E. Ernst, K.K. Lehmann, M. Gutowski, and G. Scoles. Photoinduced chemical dynamics of high-spin alkali trimers. *Science*, 273(5275):629–631, August 1996.

[25] B. Shepperson, A.S. Chatterley, A.A. Søndergaard, L. Christiansen, M. Lemeshko, and H. Stapelfeldt. Strongly aligned molecules inside helium droplets in the near-adiabatic regime. *J. Chem. Phys.*, 147(1):013946, July 2017.

[26] J.P. Toennies and A.F. Vilesov. Superfluid helium droplets: A uniquely cold nanomatrix for molecules and molecular complexes. *Ang. Chem. Int. Ed.*, 43(20):2622–2648, May 2004.

[27] L. Tiefenthaler, J. Ameixa, P. Martini, S. Albertini, L. Ballauf, M. Zankl, M. Goulart, F. Laimer, K. von Haeften, F. Zappa, and P. Scheier. An intense source for cold cluster ions of a specific composition. *Rev. Sci. Inst.*, 91(3):033315, March 2020.

[28] F. Ancilotto, P.B. Lerner, and M.W. Cole. Physics of solvation. *J. Low Temp. Phy.*, 101(5-6):1123–1146, December 1995.

[29] J. Reho, U. Merker, M.R. Radcliff, K.K. Lehmann, and G. Scoles. Spectroscopy of mg atoms solvated in helium nanodroplets. *J. Chem. Phys.*, 112(19):8409–8416, May 2000.

[30] A. Hernando, M. Barranco, R. Mayol, M. Pi, and F. Ancilotto. Density functional theory of the structure of magnesium-doped helium nanodroplets. *Phys. Rev. B*, 78(18), November 2008.

[31] S. Göde, R. Irsig, J. Tiggesbäumker, and K-H. Meiwes-Broer. Time-resolved studies on the collapse of magnesium atom foam in helium nanodroplets. *New J Phys*, 15(1):015026, January 2013.

[32] P.L. Houston D.W. Chandler. Two-dimensional imaging of state-selected photodissociation products detected by multiphoton ionization. *J. Chem. Phys.*, 87(2):1445–1447, 1987.

[33] D.H. Parker T.J.B.A. Eppink. Velocity map imaging of ions and electrons using electrostatic lenses: Application in photoelectron and photofragment ion imaging of molecular oxygen. *Rev. Sci. Inst.*, 68(9):3477–3484, 1997.

[34] B. Whitaker. *Imaging in Molecular Dynamics: Technology and Applications*. Cambridge University Press, 2003.

[35] T. Poikela, J. Plosila, T. Westerlund, M. Campbell, M. De Gaspari, X. Llopart, V. Gromov, R. Kluit, M. van Beuzekom, F. Zappon, V. Zivkovic, C. Brezina, K. Desch, Y.F., and A. Kruth. Timepix3: a 65k channel hybrid pixel readout chip with simultaneous ToA/ToT and sparse readout. *J. Inst.*, 9(05):C05013–C05013, May 2014.

[36] R.J. LeRoy. Spectroscopic reassignment and ground-state dissociation energy of molecular iodine. *J. Chem. Phys.*, 52(5):2678–2682, March 1970.

[37] M.J.J. Vrakking. An iterative procedure for the inversion of two-dimensional ion/photoelectron imaging experiments. *Rev. Sci. Inst.*, 72(11):4084–4089, November 2001.

[38] B. Dick. Inverting ion images without abel inversion: maximum entropy reconstruction of velocity maps. *Phys. Chem. Chem. Phys.*, 16(2):570–580, 2014.

[39] V. Zhaunerchyk, L. J. Frasinski, J. H. D. Eland, and R. Feifel. Theory and simulations of covariance mapping in multiple dimensions for data analysis in high-event-rate experiments. *Phys. Rev. A*, 89(5), May 2014.

[40] P. Atkins, R.S. Friedman, and P.W. Atkins. *Molecular Quantum Mechanics*. Oxford University Press, 2010.

[41] E.T. Karamatskos, S. Raabe, T. Mullins, A. Trabattoni, P. Stammer, G. Goldsztejn, R.R. Johansen, K. Długołecki, H. Stapelfeldt, M.J.J. Vrakking, S. Trippel, A. Rouzée, and J. Küpper. Molecular movie of ultrafast coherent rotational dynamics of OCS. *Nat. Comm.*, 10(1), July 2019.

[42] J. Jang and R.M. Stratt. Rotational energy relaxation of individual rotational states in liquids. *J. Chem. Phys.*, 113(14):5901–5916, October 2000.

[43] Dominik Z. Kandula, Christoph Gohle, Tjeerd J. Pinkert, Wim Ubachs, and Kjeld S. E. Eikema. Extreme ultraviolet frequency comb metrology. *Phys. Rev. Lett.*, 105(6), August 2010.

[44] Deepak Verma, Rico Mayro P. Tanyag, Sean M. O. O'Connell, and Andrey F. Vilesov. Infrared spectroscopy in superfluid helium droplets. *Adv. Phys.*, 4(1):1553569, December 2018.

[45] M. Y. Choi, G. E. Douberly, T. M. Falconer, W. K. Lewis, C. M. Lindsay, J. M. Merritt, P. L. Stiles, and R. E. Miller. Infrared spectroscopy of helium nanodroplets: novel methods for physics and chemistry. *Int. Rev. Phys. Chem.*, 25(1-2):15–75, January 2006.

[46] U. Even, J. Jortner, D. Noy, N. Lavie, and C. Cossart-Magos. Cooling of large molecules below 1 k and he clusters formation. *J. Chem. Phys.*, 112(18):8068–8071, May 2000.

[47] H. Stapelfeldt and T. Seideman. Colloquium: Aligning molecules with strong laser pulses. *Rev. Mod. Phys.*, 75(2):543–557, April 2003.

[48] A.A. Søndergaard, B. Shepperson, and H. Stapelfeldt. Nonadiabatic laser-induced alignment of molecules: Reconstructing $<\cos^2\theta>$ directly from $<\cos^2\theta_{2D}>$ by fourier analysis. *J. Chem. Phys.*, 147(1):013905, July 2017.

[49] G.Wlodarczak, D. Boucher, R. Bocquet, and J. Demaison. The rotational cosntants of methyl iodide. *J. Mol. Spec.*, 124:53–65, 1987.

[50] S. Grebenev, M. Hartmann, M. Havenith, B. Sartakov, J.P. Toennies, and A.F. Vilesov. The rotational spectrum of single ocs molecules in liquid 4he droplets. *J. Chem. Phys.*, 112(10):4485–4495, March 2000.

[51] K. Nauta and R.E. Miller. Rotational and vibrational dynamics of CO[sub 2] and n[sub 2]o in helium nanodroplets. *J. Chem. Phys.*, 115(22):10254, 2001.

[52] A.S. Chatterley, L. Christiansen, C.A. Schouder, A.V. Jørgensen, B. Shepperson, I.N. Cherepanov, G. Bighin, R.E. Zillich, M. Lemeshko, and H. Stapelfeldt. Rotational coherence spectroscopy of molecules in helium nanodroplets: Reconciling the time and the frequency domains. *Phys. Rev. Lett.*, 125(1), July 2020.

[53] B. Shepperson, A.A. Søndergaard, L. Christiansen, J. Kaczmarczyk, R.E. Zillich, M. Lemeshko, and H. Stapelfeldt. Laser-induced rotation of iodine molecules in helium nanodroplets: Revivals and breaking free. *Phys. Rev. Lett.*, 118(20), May 2017.

[54] R. Lehnig, P.L. Raston, and W. Jäger. Rotational spectroscopy of single carbonyl sulfide molecules embedded in superfluid helium nanodroplets. *Faraday Discuss.*, 142:297, 2009.

[55] I.N. Cherepanov, G. Bighin, C.A. Schouder, A.S. Chatterley, S.H. Albrechtsen, A. Viñas Muñoz, L. Christiansen, H. Stapelfeldt, and M. Lemeshko. Excited rotational states of molecules in a superfluid. *Phys. Rev. A*, 104(6), December 2021.

[56] R.J. Beuhler, R.B. Bernstein, and K.H. Kramer. Observation of the reactive asymmetry of methyl iodide. crossed beam study of the reaction of rubidium with oriented methyl iodide molecules. *J. Am. Chem. Soc.*, 88(22):5331–5332, November 1966.

[57] H. Matsuzaki, T.N. Murakami, N. Masaki, A. Furube, M. Kimura, and S. Mori. Dye aggregation effect on interfacial electron-transfer dynamics in zinc phthalocyanine-sensitized solar cells. *J. Phys. Chem. C*, 118(31):17205–17212, July 2014.

[58] C.G. Claessens, D. González-Rodríguez, M.S. Rodríguez-Morgade, A. Medina, and T. Torres. Subphthalocyanines, subporphyrazines, and subporphyrins: Singular nonplanar aromatic systems. *Chem. Rev.*, 114(4):2192–2277, December 2013.

[59] H. Gotfredsen, T. Neumann, F.E. Storm, A.V. Muñoz, M. Jevric, O. Hammerich, K.V. Mikkelsen, M. Freitag, G. Boschloo, and M.B. Nielsen. Donor-acceptor-functionalized subphthalocyanines for dye-sensitized solar cells. *ChemPhotoChem*, 2(11):976–985, August 2018.

[60] M. Ince, A. Medina, J-H. Yum, A. Yella, C.G. Claessens, M.V. Martínez-Díaz, M. Grätzel, M.K. Nazeeruddin, and T. Torres. Peripherally and axially carboxylic acid substituted subphthalocyanines for dye-sensitized solar cells. *Chem. Eur. J.*, 20(7):2016–2021, January 2014.

[61] G.E. Morse and T.P. Bender. Boron subphthalocyanines as organic electronic materials. *ACS App. Mat. & Int.*, 4(10):5055–5068, September 2012.

[62] A. Slenczka. Electronic spectroscopy of phthalocyanine and porphyrin derivatives in superfluid helium nanodroplets. *Molecules*, 22(8):1244, July 2017.

[63] S. Fuchs, J. Fischer, A. Slenczka, M. Karra, and B. Friedrich. Microsolvation of phthalocyanine molecules in superfluid helium nanodroplets as revealed by the optical line shape at electronic origin. *J. Chem. Phys.*, 148(14):144301, April 2018.

[64] J. Fischer, F. Schlaghaufer, E.-M. Lottner, A. Slenczka, L. Christiansen, H. Stapelfeldt, M. Karra, B. Friedrich, Th. Mullan, M. Schütz, and D. Usvyat. Heterogeneous clusters of phthalocyanine and water prepared and probed in superfluid helium nanodroplets. *Journal Phys. Chem. A*, 123(46):10057–10064, October 2019.

[65] A.S. Chatterley, E.T. Karamatskos, C. Schouder, L. Christiansen, A.V. Jørgensen, T. Mullins, J. Küpper, and H. Stapelfeldt. Communication: Switched wave packets with spectrally truncated chirped pulses. *J. Chem. Phys.*, 148(22):221105, June 2018.

[66] A.S. Chatterley, C. Schouder, L. Christiansen, B. Shepperson, M. Heidemann Rasmussen, and H. Stapelfeldt. Long-lasting field-free alignment of large molecules inside helium nanodroplets. *Nat. Comm.*, 10(1), January 2019.

[67] J.D. Pickering, B. Shepperson, L. Christiansen, and H. Stapelfeldt. Alignment of the CS2 dimer embedded in helium droplets induced by a circularly polarized laser pulse. *Phys. Rev. A*, 99(4), April 2019.

[68] L. Christensen, L. Christiansen, B. Shepperson, and H. Stapelfeldt. Deconvoluting nonaxial recoil in coulomb explosion measurements of molecular axis alignment. *Phys. Rev. A*, 94(2), August 2016.

[69] Joel Tellinghuisen. Resolution of the visible-infrared absorption spectrum of i2 into three contributing transitions. *J. Chem. Phys.*, 58(7):2821, 1973.

[70] D.W. Chandler and P.L. Houston. Two-dimensional imaging of state-selected photodissociation products detected by multiphoton ionization. *J. Chem. Phys.*, 87(2):1445–1447, July 1987.

[71] A. G. Sage, T.A.A. Oliver, D. Murdock, M.B. Crow, G.A.D. Ritchie, J.N. Harvey, and M.N.R. Ashfold. n$\sigma^*$ and $\pi\sigma^*$ excited states in aryl halide photochemistry: a comprehensive study of the UV photodissociation dynamics of iodobenzene. *Phys. Chem. Chem. Phys.*, 13(18):8075, 2011.

[72] K. Kavita and P.K. Das. Photodissociation of c6h5i, c6f5i, and related iodides in the ultraviolet. *J. Chem. Phys.*, 117(5):2038–2044, August 2002.

[73] A.L. Harris, J.K. Brown, and C.B. Harris. The nature of simple photodissociation reactions in liquids on ultrafast time scales. *Annu. Rev. Phys. Chem.*, 39(1):341–366, October 1988.

[74] P.K. Walhout, C. Silva, and P.F. Barbara. Ultrafast study of the photodissociation and recombination of aqueous o3-. *J. Phys. Chem.*, 100(13):5188–5199, January 1996.

[75] Michael N.R. Ashfold, Daniel Murdock, and Thomas A.A. Oliver. Molecular photofragmentation dynamics in the gas and condensed phases. *Annu. Rev. Phys. Chem.*, 68(1):63–82, May 2017.

[76] David Booth and Richard M. Noyes. The effect of viscosity on the quantum yield for iodine dissociation. *J. Am. Chem. Soc.*, 82(8):1868–1872, April 1960.

[77] A. Braun and M. Drabbels. Photodissociation of alkyl iodides in helium nanodroplets. i. kinetic energy transfer. *J. Chem. Phys.*, 127(11):114303, September 2007.

[78] A. Braun and M. Drabbels. Photodissociation of alkyl iodides in helium nanodroplets. II. solvation dynamics. *J. Chem. Phys.*, 127(11):114304, September 2007.

[79] A. Braun and M. Drabbels. Photodissociation of alkyl iodides in helium nanodroplets. III. recombination. *J. Chem. Phys.*, 127(11):114305, September 2007.

[80] R.A. Crowell, R. Lian, M.C. Sauer, D. A. Oulianov, and I.A. Shkrob. Geminate recombination of hydroxyl radicals generated in 200 nm photodissociation of aqueous hydrogen peroxide. *Chem. Phys. Lett.*, 383(5-6):481–485, January 2004.

[81] J.M. Papanikolas, J.R. Gord, N.E. Levinger, D. Ray, V. Vorsa, and W.C. Lineberger. Photodissociation and geminate recombination dynamics of i2- in mass-selected i2-(CO2)n cluster ions. *J. Phys. Chem.*, 95(21):8028–8040, October 1991.

[82] T. Kühne and P. Vöhringer. Vibrational relaxation and geminate recombination in the femtosecond-photodissociation of triiodide in solution. *J. Chem. Phys.*, 105(24):10788–10802, December 1996.

[83] S.H. Gardiner, M.L. Lipciuc, T.N.V. Karsili, M.N.R. Ashfold, and C. Vallance. Dynamics of the a-band ultraviolet photodissociation of methyl iodide and ethyl iodide via velocity-map imaging with 'universal' detection. *Phys. Chem. Chem. Phys.*, 17(6):4096–4106, 2015.

[84] S.M. Poullain, M.G. González, P.C. Samartzis, T.N. Kitsopoulos, L. Rubio-Lago, and L. Bañares. New insights into the photodissociation of methyl iodide at 193 nm: stereodynamics and product branching ratios. *Phys. Chem. Chem. Phys.*, 17(44):29958–29968, 2015.

[85] Y-J. Jung, Y.S. Kim, W.K. Kang, and K-H. Jung. Photoelectron imaging spectroscopy for (2+1) resonance-enhanced multiphoton ionization of atomic iodine produced from a-band photolysis of CH3i. *J. Chem. Phys.*, 107(18):7187–7193, November 1997.

[86] A.T.J.B. Eppink and D.H. Parker. Methyl iodide a-band decomposition study by photofragment velocity imaging. *J. Chem. Phys.*, 109(12):4758–4767, September 1998.

[87] E. Luc-Koenig, C. Morillon, and J. Vergès. Etude expérimentale et théorique de l'iode atomique.observation du spectre d'arc infrarouge, classification et structure hyperfine. *Phys. Scripta*, 12(4):199–219, October 1975.

[88] L. Drescher, M.C.E. Galbraith, G. Reitsma, J. Dura, N. Zhavoronkov, S. Patchkovskii, M.J.J. Vrakking, and J. Mikosch. Communication: XUV transient absorption spectroscopy of iodomethane and iodobenzene photodissociation. *J. Chem. Phys.*, 145(1):011101, July 2016.

[89] F. Coppens, J. von Vangerow, M. Barranco, N. Halberstadt, F. Stienkemeier, M. Pi, and M. Mudrich. Desorption dynamics of RbHe exciplexes off he nanodroplets induced by spin-relaxation. *Phys. Chem. Chem. Phys.*, 20(14):9309–9320, 2018.

[90] M. Kadi, J. Davidsson, A.N. Tarnovsky, M. Rasmusson, and E. Åkesson. Photodissociation of aryl halides in the gas phase studied with femtosecond pump-probe spectroscopy. *Chem. Phys. Lett.*, 350(1-2):93–98, December 2001.

[91] R. Montero, A.P. Conde, A. Longarte, F. Castaño, M.E. Corrales, R. de Nalda, and L. Bañares. Femtosecond time-resolved photophysics and photodissociation dynamics of 1-iodonaphthalene. *Phys. Chem. Chem. Phys.*, 12(28):7988, 2010.

[92] J. von Vangerow, A.S. Bogomolov, N.V. Dozmorov, D. Schomas, F. Stienkemeier, A.V. Baklanov, and M. Mudrich. Role of ion-pair states in the predissociation dynamics of rydberg states of molecular iodine. *Phys.Chem. Chem. Phys.*, 18(28):18896–18904, 2016.

[93] M.H. Palmer, T. Ridley, S. Vrønning Hoffmann, N.C. Jones, M. Coreno, M. de Simone, C. Grazioli, M. Biczysko, and A. Baiardi. The ionic states of iodobenzene studied by photoionization andab initioconfiguration interaction and DFT computations. *J. Chem. Phys.*, 142(13):134301, April 2015.

[94] T. Kumpulainen, B. Lang, A. Rosspeintner, and E. Vauthey. Ultrafast elementary photochemical processes of organic molecules in liquid solution. *Chem. Rev.*, 117(16):10826–10939, December 2016.

[95] J. Israelachvili. Intermolecular and surface forces. *Academic Press*, 2011.

[96] F. London. The general theory of molecular forces. *T. Faraday Soc.*, 33:8b, 1937.

[97] Z. Vager, R. Naaman, and E.P. Kanter. Coulomb explosion imaging of small molecules. *Science*, 244(4903):426–431, April 1989.

[98] T. Yatsuhashi and N. Nakashima. Multiple ionization and coulomb explosion of molecules, molecular complexes, clusters and solid surfaces. *J. Photoch. Photobio. C Photoch. Rev.*, 34:52–84, March 2018.

[99] C.A. Schouder, A.S. Chatterley, L.B. Madsen, F. Jensen, and H. Stapelfeldt. Laser-induced coulomb-explosion imaging of the $cs_2$ dimer: The effect of non-coulombic interactions. *Phys. Rev. A*, 102(6), December 2020.

[100] R. Jimenez, Graham R. Fleming, P. V. Kumar, and M. Maroncelli. Femtosecond solvation dynamics of water. *Nature*, 369(6480):471–473, June 1994.

[101] S. Cao, H. Li, Z. Zhao, S. Zhang, J. Chen, J. Xu, J.R. Knutson, and L. Brand. Ultrafast fluorescence spectroscopy via upconversion and its applications in biophysics. *Molecules*, 26(1):211, January 2021.

[102] E. Biasin, Z.W. Fox, A. Andersen, K. Ledbetter, K. S. Kjær, R. Alonso-Mori, J.M. Carlstad, M. Chollet, J.D. Gaynor, J.M. Glownia, K. Hong, T. Kroll, J.H. Lee, C. Liekhus-Schmaltz, M. Reinhard, D. Sokaras, Y. Zhang, G. Doumy, A.M. March, S.H. Southworth, S. Mukamel, K.J. Gaffney, R.W. Schoenlein, N. Govind, A.A. Cordones, and M. Khalil. Direct observation of coherent femtosecond solvent reorganization coupled to intramolecular electron transfer. *Nat. Chem.*, 13(4):343–349, February 2021.

[103] P. Rossky and J.Simon. Dynamics of chemical processes in polar solvents. *Nature*, 370:263–269, 1994.

[104] J.T. Hynes. Chemical reaction dynamics in solution. *Annu. Rev. Phys. Chem.*, 36(1):573–597, 1985.

[105] S. Mecozzi, A.P. West, and D.A. Dougherty. Cation-pi interactions in simple aromatics: Electrostatics provide a predictive tool. *J. Am. Chem. Soc.*, 118(9):2307–2308, 1996.

[106] F. Ancilotto, M. Barranco, F. Coppens, J. Eloranta, N. Halberstadt, A. Hernando, D. Mateo, and M. Pi. Density functional theory of doped superfluid liquid helium and nanodroplets. *Int. Rev. Phys. Chem.*, 36(4):621–707, August 2017.

[107] F. Coppens, F. Ancilotto, M. Barranco, N. Halberstadt, and M. Pi. Dynamics of impurity clustering in superfluid 4he nanodroplets. *Phys. Chem. Chem. Phys.*, 21(31):17423–17432, 2019.

[108] A. Hernando, M. Barranco, M. Pi, E. Loginov, M. Langlet, and M. Drabbels. Desorption of alkali atoms from 4he nanodroplets. *Phys. Chem. Chem. Phys.*, 14(11):3996, 2012.

[109] S.H. Patil. Adiabatic potentials for alkali–inert gas systems in the ground state. *J. Chem. Phys.*, 94(12):8089–8095, June 1991.

[110] A. Leal, D. Mateo, A. Hernando, M. Pi, M. Barranco, A. Ponti, F. Cargnoni, and M. Drabbels. Picosecond solvation dynamics of alkali cations in superfluid 4he nanodroplets. *Phys. Rev. B*, 90(22), December 2014.

[111] A. Leal, X. Zhang, M. Barranco, F. Cargnoni, A. Hernando, D. Mateo, M. Mella, M. Drabbels, and M. Pi. Dynamics of photoexcited $ba^+$ cations in 4he nanodroplets. *J. Chem. Phys.*, 144(9):094302, March 2016.

[112] A.D. Koutselos, E.A. Mason, and L.A. Viehland. Interaction universality and scaling laws for interaction potentials between closed-shell atoms and ions. *J. Chem. Phys.*, 93(10):7125–7136, November 1990.

[113] T. González-Lezana, O. Echt, M. Gatchell, M. Bartolomei, J. Campos-Martínez, and P. Scheier. Solvation of ions in helium. *Int. Rev. Phys. Chem.*, 39(4):465–516, August 2020.

[114] Y. Ren and V.V. Kresin. Surface location of alkaline-earth-metal-atom impurities on helium nanodroplets. *Phys. Rev. A*, 76(4), October 2007.